LA--10941-T

DE87 006168

LA-10941-T
Thesis

UC-34D
Issued: March 1987

Inelastic Pion Scattering by ^{13}C at Low Energies

Joseph Hamilton Mitchell*

---

*Guest Scientist at Los Alamos. Deparment of Physics, University of Colorado, Boulder, CO 80309.

Los Alamos
Los Alamos National Laboratory
Los Alamos, New Mexico 87545

CONTENTS

CHAPTER

I. INTRODUCTION 1

General properties of the πN and πA Systems 1

Why Low Energy Pions? 5

Why ^{13}C? 8

II. THE EXPERIMENT 11

LAMPF and LEP 11

The Clamshell Spectrometer 16

The Detectors 21

The Electronics 26

Data Acquisition and Replay 28

Peak Fitting 33

Resolution 37

Differential Cross Sections 39

Normalization Procedure and Systematic Uncertainties 45

III. THEORY 48

The Optical Analogy 48

The Scattering Amplitude 50

Scattering Theory 53

The Born Series and DWBA 55

Multiple Scattering and the Impulse Approximation.... 57
The Computer Codes.................................. 60
The Specific Optical Potential......................... 61
Medium Modifications.................................. 63
Matter Densities and Form Factors..................... 66
IV. COMPARISON OF THEORY TO DATA................. 68
Elastic Scattering.. 68
The Collective Model.................................. 75
The States at 3.68 MeV and 7.55 MeV in Excitation.... 77
The State at 11.82 MeV................................ 83
The Monopole Transition at 8.86 MeV in Excitation.... 83
Summary of the Results for the Collective Excitations.. 86
The Spin-Flip Transition at 9.5 MeV.................. 101
Data for the State at 9.9 MeV.......................... 109
V. EXCITATION FUNCTIONS............................. 112
Why Fixed $|\vec{q}|$ Excitation Functions?.................. 113
The Data... 115
Excitation Functions for $q \approx 0.96\ \mathrm{fm}^{-1}$................ 116
Excitation Functions for $q \approx 1.1\ \mathrm{fm}^{-1}$.................. 117
VI. CONCLUSIONS....................................... 126
Experimental Remarks.................................. 126
Final Summary of Results.............................. 128
REFERENCES... 130

APPENDIX

A. CHANNEL LOG 134
B. POLYNOMIAL FILE 135
C. REPRESENTATIVE Q FILES 138
D. PION DECAY 150

TABLES

Table

4.1 Deformation Lengths.. 102

FIGURES

Figure

1.1 Total cross sections for $\pi^{\pm}p$ 3
1.2 Zero degree SCX excitation funtion 6
1.3 Pion meanfree path vs pion kinetic energy 7
2.1 Time structure of the LAMPF proton beam 13
2.2 The experimental areas at LAMPF 14
2.3 The LEP channel 15
2.4 The Clamshell Spectrometer and its detectors 17
2.5 Schematic view of a drift chamber 24
2.6 Drift chamber histograms 27
2.7 Q system architecture 31
2.8 Uncorrected PID 34
2.9 Corrected PID 35
2.10 Sample missing mass spectra 38
2.11 Focal plane efficiency 44
4.1 Ground state matter densities 72
4.2 π^+ elastic scattering at 65 MeV 73
4.3 π^- elastic scattering at 65 MeV 74
4.4 π^+ scattering to the state at 3.68 MeV in excitation 79
4.5 π^- scattering to the state at 3.68 MeV in excitation 80

4.6 π^+ scattering to the state at 7.55 MeV in excitation.. 81

4.7 π^- scattering to the state at 7.55 MeV in excitation........... 82

4.8 π^+ scattering to the state at 11.82 MeV in excitation.......... 84

4.9 π^+ scattering to the state at 11.82 MeV in excitation.......... 85

4.10 Transition densities for the collective transitions............... 87

4.11 π^+ scattering to the state at 8.86 MeV in excitation........... 88

4.12 π^- scattering to the state at 8.86 MeV in excitation........... 89

4.13 π^+ and π^- elastic scattering at 100 MeV....................... 92

4.14 π^+ and π^- scattering to the state at 3.68 MeV in excitation, T_π =100 MeV.. 93

4.15 π^+ and π^- scattering to the states at 7.55 MeV and 11.82 MeV in excitation, T_π =100 MeV.............................. 94

4.16 π^+ and π^- elastic scattering at 162 MeV...................... 95

4.17 π^+ and π^- scattering to the two $L = 2$ transitions, T_π =162 MeV.. 96

4.18 π^+ and π^- scattering to the monopole transition at 8.86 MeV, T_π =162 MeV.. 97

4.19 π^+ and π^- scattering to the state at 11.82 MeV in excitation, T_π =162 MeV... 98

4.20 The particle-hole structure of the $\frac{9}{2}^+$ state..................... 103

4.21 π^+ and π^- scattering to the state at 9.5 MeV in excitation, T_π =162 MeV... 106

4.22 π^+ and π^- scattering to the state at 9.5 MeV in excitation, T_π =100 MeV... 107

4.23 π^+ and π^- scattering to the state at 9.5 MeV in excitation, T_π =65 MeV.. 108

4.24 Data for π^+ and π^- scattering to the state at 9.9 MeV, T_π =65 MeV.. 111

5.1 Fixed $q \approx 0.96$ fm^{-1} π^- excitation function for the state at 3.68 MeV 118

5.2 Fixed $q \approx 0.96$ fm^{-1} π^- excitation function for the state at 7.55 MeV 119

5.3 Fixed $q \approx 0.96$ fm^{-1} π^- excitation function for the state at 11.82 MeV 120

5.4 Fixed $q \approx 0.96$ fm^{-1} π^- excitation function for the state at 9.5 MeV 121

5.5 Fixed $q \approx 1.1$ fm^{-1} π^+ excitation function for the state at 3.68 MeV 123

5.6 Fixed $q \approx 1.1$ fm^{-1} π^+ excitation function for the state at 7.55 MeV 124

5.7 Fixed $q \approx 1.1$ fm^{-1} π^+ excitation function for the state at 8.86 MeV 125

Inelastic Pion Scattering by ^{13}C at Low Energies

by

Joseph Hamilton Mitchell

ABSTRACT

Angular distributions for inelastically scattered pions were obtained for several states in ^{13}C at an incident energy of 65 MeV. The data include results from both π^+ and π^- measurements. In addition, π^- measurements were made at $T_\pi = 50$ MeV at one angle to give a two point fixed-q excitation function. The data are compared to theory and the data of others. As might be expected, medium corrections are shown to be considerably more important at low energies than at resonance. This is true for inelastic transitions of multipolarity 0,2 and 3. Parameters derived from an analysis of elastic pion scattering and SCX data also provide an adequate description of the inelastic transitions. The charge asymmetry in the cross sections for the $9/2^+$ state that was seen at resonance persists at these energies. This result is consistent with an impulse approximation treatment of the spin-flip amplitude. This is true even though the incoming energy of the pions is far below the range where the validity of an impulse treatment is expected.

CHAPTER I

INTRODUCTION

This thesis contains the results of a measurement of cross sections for inelastic pion scattering to several states in ^{13}C. The purpose of this chapter is to explain the motivation for performing the experiment and also to present some relevant background information.

General Properties of the Pion-Nucleon and Pion-Nucleus Systems

The pion is a spin zero boson with negative intrinsic parity, $J^\pi = 0^-$. It can be found in three charge states, π^+,π^- and π^0,corresponding to the three projections of its isospin, $m_\tau = 0, \pm 1$, for the T=1 particle. The fact that it is a boson allows it to be emitted or absorbed singly in interactions with nucleons and/or nuclei. It is this fact which leads to a picture in which the exchange of pions intermediates the long-range part of the nucleon-nucleon interaction. It was from considerations of the range of nuclear forces that Yukawa first predicted the existence and mass of the pion in 1935 [Yuk 35]. In terms of the more modern quark picture of hadrons the pion, being a meson, is composed of a quark and an antiquark in a color singlet. Since the pion is the lightest strongly interacting meson it is constructed of only the two lightest quarks, the up and down, and their corresponding antiquarks. A knowledge of the quark charges ($u = +2/3e$, $d = -1/3e$) allows one to write down the quark substructure of any particular pion charge state.

When the scattering of pions with kinetic energy less than 300 MeV from nucleons is examined (Fig 1.1) the dominant feature of the data is seen to be a large resonance at an incident pion energy of approximately 180 MeV with a width of about 100 MeV. This corresponds to the production and subsequent decay of virtual $\Delta(1232)$ particles in the process

$$\pi + N \rightarrow \Delta \rightarrow \pi + N.$$

This resonance is often referred to as the $(3,3)$ resonance, a nomenclature which comes from (2J,2T) where J and T are the spin and isospin of the Δ. J can be decomposed as

$$J = s_\pi + s_N + l_{rel}.$$

Since the pion has spin zero, $s_\pi = 0$, the resonance must take place in either a relative p or d-wave state of the pion nucleon system. Phase shift analyses (see for instance [Bar 68]) of a great volume of experimental data points to the fact that it is the relative p-wave state of the πN system that undergoes this resonance and hence it is the $p_{3,3}$ phase shift that dominates the πN interaction at resonance energies.

The assumption of Δ dominance and the use of some simple isospin relationships imply the following ratios of cross sections

$$\sigma(\pi^+ p \rightarrow \pi^+ p) : \sigma(\pi^+ n \rightarrow \pi^+ n) : \sigma(\pi^+ n \rightarrow \pi^0 p) = 9 : 1 : 2$$

$$\sigma(\pi^- n \rightarrow \pi^- n) : \sigma(\pi^- p \rightarrow \pi^- p) : \sigma(\pi^- p \rightarrow \pi^0 n) = 9 : 1 : 2.$$

If this behavior were to continue in the case of π-nucleus interactions, ratios of π^+ to π^- cross sections would be an excellent way of distinguishing the

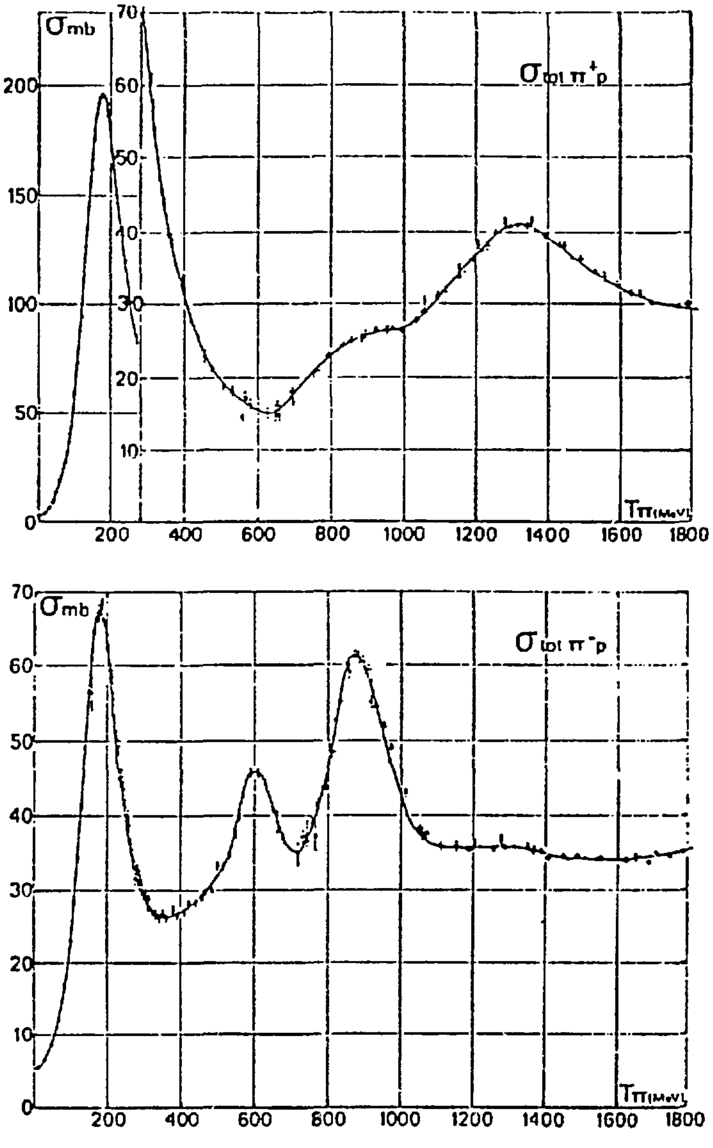

Figure 1.1 The total cross sections for π^+p and π^-p as a function of incident pion energy [Bar 68].

neutron and proton pieces of nuclear ground state and transition densities. This was in fact one of the primary goals of experimental pion physics when the meson factories, LAMPF, TRIUMF and SIN, were built in the 1970s. Although this technique has not been as useful as had been hoped, there have been some successes [Boy 81][Ull 86a] along these lines. In fact the measurement at resonance [See 81] of the 9/2+ state at 9.5 MeV in ^{13}C is one of the more dramatic examples of an experimental sensitivity to the neutron-like structure of a state.

The fact that pions have an isospin of one means that in addition to elastic and inelastic scattering they can also undergo single charge exchange (for example $\pi^+, Z \rightarrow \pi^0, Z+1$) and double charge exchange ($\pi^+, Z \rightarrow \pi^-, Z+2$) reactions with nuclei. The double charge exchange reaction is perhaps the only way to look experimentally at double isobaric analog states. As alluded to earlier, since pions are bosons they can be absorbed in the nucleus, giving up their rest mass, in a process called true absorption. The name true absorption is used to signify processes in which the pion does not appear in the exit channels. This is not the same as optical absorption which refers to the absorption inherent in a multiple scattering picture (see Chapter 3). Both double charge exchange and pion true absorption must involve at least two nucleons. Double charge exchange must involve two nucleons for isospin reasons, whereas kinematics require at least two nucleons for true absorption. (Actually this is not strictly true, pion absorption cannot take place on a single free nucleon for kinematic reasons. However the argument does not hold rigorously for absorption on a nucleon in a bound system.)

Therefore these reactions provide a tool for probing two or more nucleon correlations.

Why Low-Energy Pions ?

Pion experiments with incident energies below the (3,3) resonance are interesting for a number of reasons. First, the scattering process is no longer totally dominated by one partial wave ($p_{3,3}$). In fact, interference between the repulsive s-wave and the attractive p-wave becomes appreciable as their magnitudes become nearly equal. This interference is clearly seen in zero-degree single charge exchange data (Fig 1.2) [Ull 86b] where the deep minimum in the excitation function at $T_\pi \approx 50$ MeV is due to the almost perfect cancellation of these two amplitudes.

Secondly, although there is a great deal of data for inelastic scattering at resonance energies there are currently few data at incident energies below 100 MeV. This paucity of data is due largely to the lack of a good low energy spectrometer facility. Another reason that data at these energies are scarce is that many aspects of the problem conspire to make low-energy measurements experimentally more difficult. The principal problem is that the pion decay losses become larger and larger as the energy of the incident pions is decreased. Therefore the pion flux on target drops as well. In addition to this diminished beam flux, the fundamental cross sections (the total cross sections for πN scattering) decrease with decreasing energy. These two facts mean that it requires longer running times to accumulate low-energy pion data than to aquire equivalent data at resonance energies.

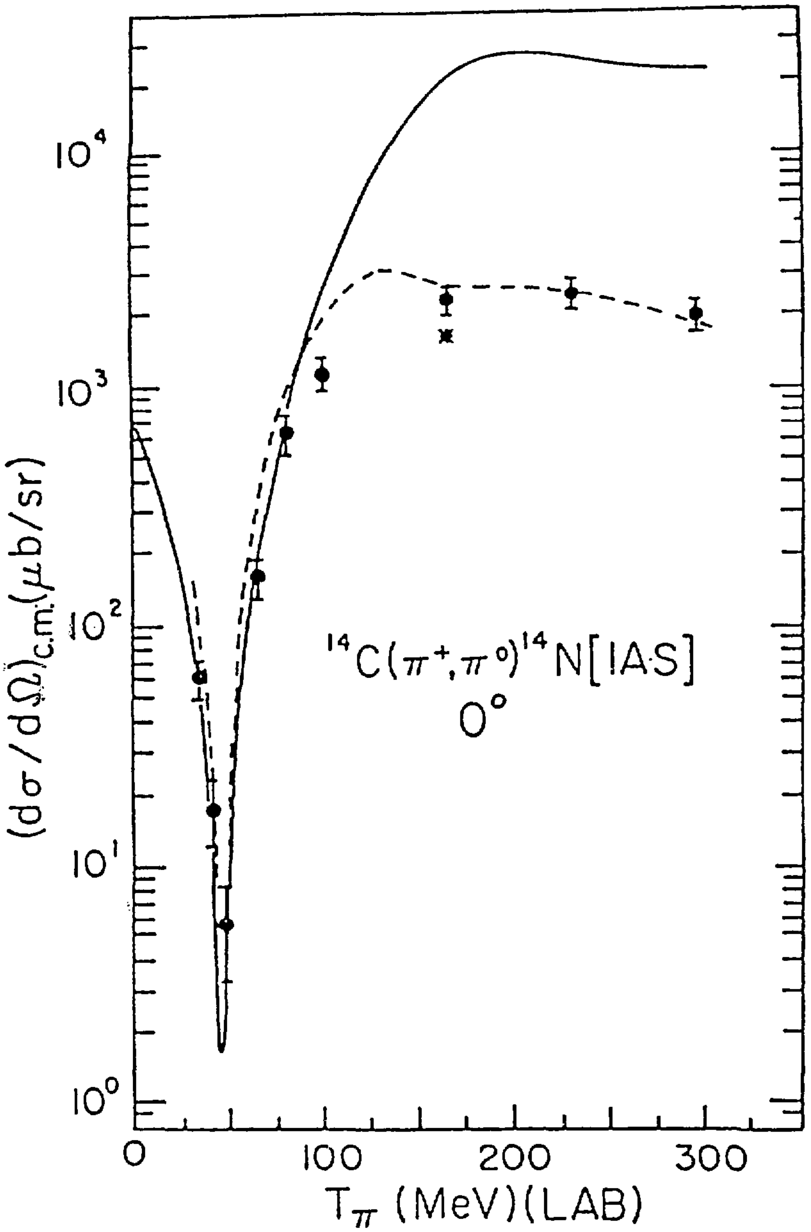

Figure 1.2 Zero degree excitation function for single charge exchange on ^{14}C. The minimum is due to the destructive interference of the s-wave and p-wave pieces of the interaction [Ull 86b].

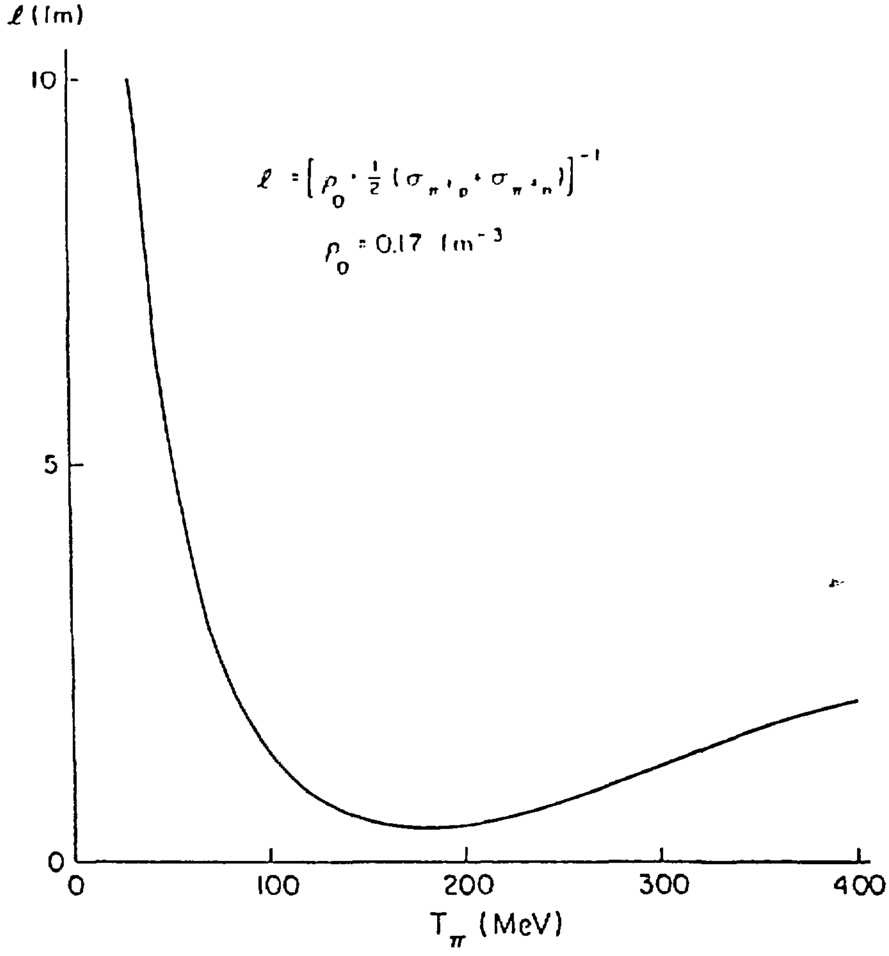

Figure 1.3 The meanfree path of pions in nuclear matter as a function of energy [Kol 80].

As shown in Figure 1.1 the total cross section for pion interactions is smaller at these energies. Therefore the mean free path of the pions is correspondingly longer, as shown in Figure 1.3 and hence it is expected that low energy experiments may probe the interior of the nuclear ground state and transition densities. This is important as resonance experiments only sample the tails of the matter distributions.

Finally medium (absorption and nuclear correlations) effects are expected to be relatively more important at low energies than at energies near the (3,3) resonance. This is calculationally a disadvantage as no detailed models of these processes exist. However, measured inelastic cross sections should provide some quantitative measure of these effects.

Why ^{13}C ?

Carbon 13 was chosen as the target for this investigation because its spectroscopy is well known. By this it is meant that the energies of its excited states are well known and hence the experiment is largely self energy calibrating (this is certainly true for excitation energies up to about 10 MeV since there are several well separated states with which to calibrate). Also the spins and parities of these excitations are well documented, as are their single particle or collective nature.

Another advantage of this nucleus is that there exists some theoretical guidance in the form of shell model calculations of particle-hole strengths [Lee 80a][Lee 80b] which have been demonstrated to provide adequate descriptions of pion scattering to many of the states of interest at resonance

[See 81]. This well understood nuclear structure is important so that comparisons of data to theory will alllow some inferences about the π-nucleus reaction models.

Among the most interesting states in ^{13}C is the 9/2+ state at 9.5 MeV. Transitions to the ground state from this state are almost purely M4 in nature. Virtually no E5, the other transition mode that is consistent with selection rules, is seen [Hic 86]. This result is verified from pion scattering excitation functions [See 81] and is understood in terms of the nuclear structure [Lee 80b]. On the basis of π^-/π^+ ratios taken at resonance [See 81] this state appears to be a very pure neutron spin-flip state $(\Delta J = 4, \Delta L = 3, \Delta S = 1)$ with a neutron particle-hole configuration of $d_{5/2}p_{3/2}^{-1}$ coupled to the extra $p_{1/2}$ neutron that is present in the ^{13}C ground state. This very pure spin-flip state is an ideal place to examine the strength of the spin-flip piece of the π-nucleus interaction at low energies.

The other low lying excitations are also of interest. These are mostly collective states and they have been studied by numerous reactions [Pet 81] [Bla 78]. A comparison of low energy pion scattering results with the information obtained by other reactions could be beneficial due to the highly penetrating nature of the probe. The nuclear structure of these states is well described by the simple collective model [See 81]. This being the case, a comparison of the measured cross sections for scattering to these states and distorted wave calculations should allow the extraction of reaction mechanism information. Certainly these data will provide a test of the extent to which medium effects must be included in order to successfully describe low energy pion scattering.

In the next chapter the details of the experiment are discussed. This is followed by a brief overview of the theory of pion scattering. At that point the results of the experiment are compared with theory as well as with other data.

CHAPTER II

THE EXPERIMENT

LAMPF and LEP

The experiment was performed at the Clinton P. Anderson Meson Physics Facility (LAMPF) on the Low Energy Pion Channel (LEP). The positive and negative pions at LEP are produced as secondary beams by using the primary proton beam from the LAMPF linear accelerator (linac). The linac at Los Alamos is approximately one half mile in length and has three principal sections. The first section consists of the ion sources and the Cockcroft-Walton generators. The ion sources are pulsed and are the reason for the macro-time stucture in the primary proton beam. The Cockcroft - Waltons are D.C. devices that provide the initial acceleration of the particles to an energy of 750 keV. The second section is an Alvarez-type drift tube linear accelerator which has an operating frequency of 201.25 MHz and it is this section that gives the beam its 5 ns micro-time structure as shown in Figure 2.1. When the particles exit the second section they have obtained a kinetic energy of about 200 Mev and are ready to enter the final section which is a resonantly-side-coupled standing wave linear accelerator with an operating frequency of 805 MHz. The machine is operated at a duty factor of approximately 10% with an average beam current as high as 1 mA. Pions for the Energetic Pion Channel and Spectrometer, EPICS, and LEP are produced by impinging the line A proton beam on a graphite target designated A-1. Because of the tremendous power dissipated in the production target by the beam, the target is both water cooled and rotated to prevent it from burning. Figure 2.2 shows the LAMPF experimental areas and the A-1 production target.

LEP is discussed in detail elsewhere [Bur 75] so only a brief description is given here. The beamline optics are shown in Figure 2.3. The channel contains two quadrupole doublets, the first of which is two magnets designated QM01 and QM02, and the second QM03 and QM04. The channel bends the incoming pions in a vertical plane by using the four dipoles designated BM01-BM04. Three four-jaw collimators allow adjustment of the channel's solid angle and hence the pion flux on target. In addition there is a momentum slit that allows the momentum spread of the beam to be tailored to the needs of the individual experiment. This feature is very important as the LEP beamspot is achromatic and hence the spread in beam momentum makes a direct contribution to the resolution of measurements made using the channel as a pion source. It should be noted that the setting of this slit also effects the beam rate. There are two additional items worth mentioning, the proton absorbers for separating contaminant protons from pions using differential energy loss and the gas barrier which is a 3 mil kapton window used to prevent radioactive ^6He gas from seeping down the channel from the production target and into the area. This barrier was leaking at the time of this experiment so an additional 3 mil window was installed at the juncture of the channel snout with the scattering chamber.

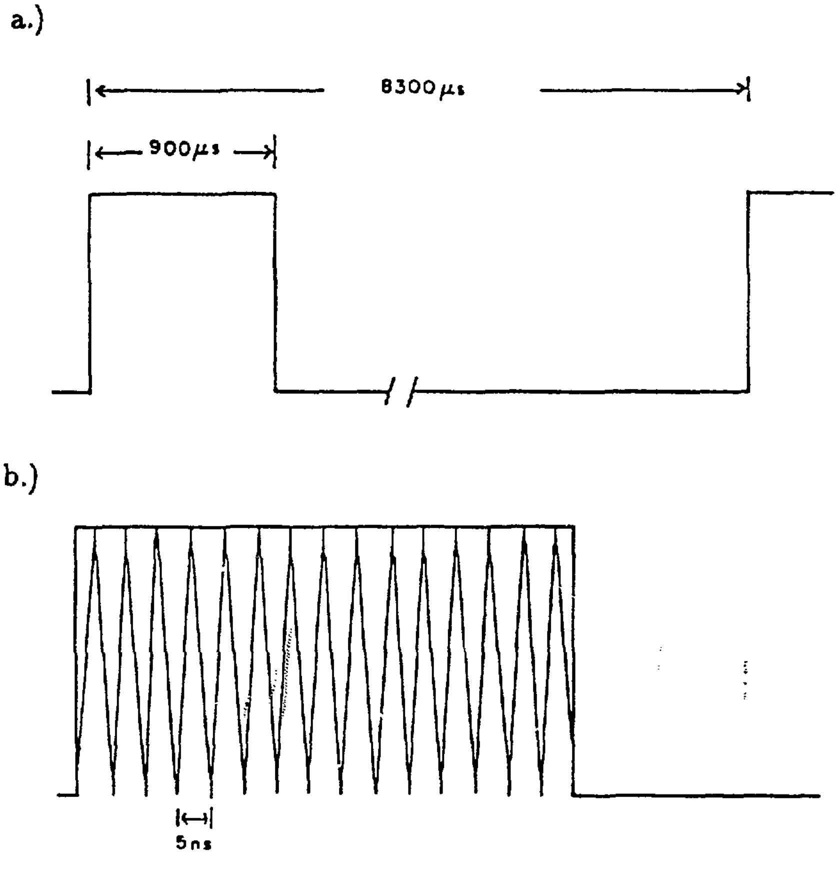

Figure 2.1 a.) The macro-time structure of the primary proton beam. The duty factor is approximately 11%. (The duty factor is $\approx \frac{900\ \mu s}{8300\ \mu s} \times 100$) b.) The micro-time structure of the LAMPF proton beam.

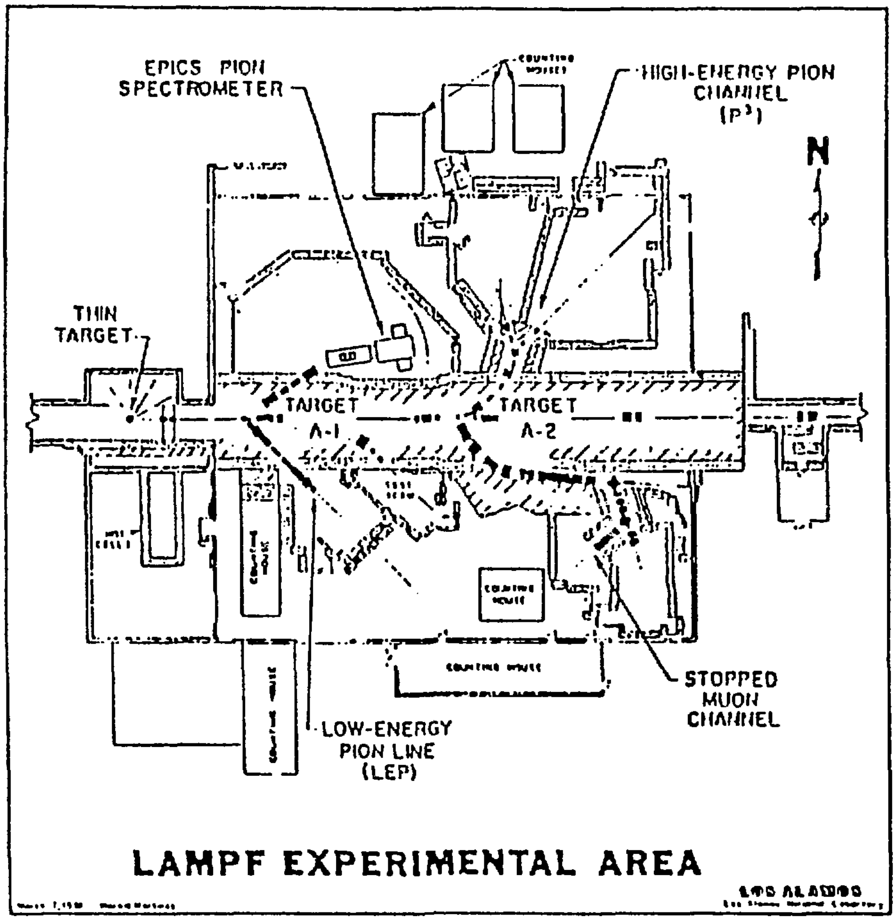

Figure 2.2 The experimental areas at LAMPF. The Low Energy Pion Channel (LEP) is shown [LUH 80].

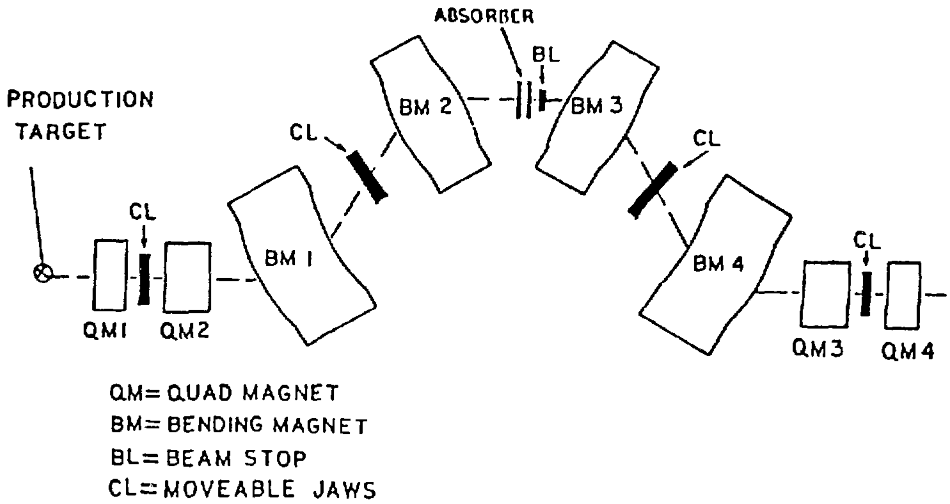

Figure 2.3 The magnetic elements that comprise the LEP channel [Fic 85].

Channel logs were kept during the experiment; a sample log entry is in Appendix A. Since the channel was intended for transport of low energy pions, minimizing its length was a prime concern to minimize decay losses. Its final length, including a 1.9 m final drift to target, was 15.2 m.

The Clamshell Spectrometer

The scattered pions were momentum analysed using the Clamshell Spectrometer. Since this was one of the first experiments to use this device, it is not surprising that some difficulties were encountered. In particular, the design resolution of 250 keV at 50 MeV had not yet been achieved. The Clamshell is basically a dipole with non-parallel pole faces which provide some focusing in the non-dispersive direction. It is pictured in Figure 2.4 both from the side and in a cutaway that shows the non-uniform gap between the pole faces. The magnetic field along the mid-plane of the spectrometer varies roughly as the reciprocal of the gap distance. Since charged pions have a mean lifetime of only 2.6×10^{-8} sec (in their rest frame), the Clamshell has a central path length of only 1.8 m. This short path length coupled with its large solid angle, $d\Omega \approx 40$ msr, make it well suited for work with pions whose kinetic energies are less than 100 MeV.

In all discussions of the spectrometer the following coordinate system will be used unless otherwise stated: z is in the direction of the beam, x is in the dispersion direction (positive down at the target), and y is in the non-dispersive direction such that (x,y,z) forms a right-handed triad. The passage of particles through the spectrometer can be treated in analogy with the passage of light through an optical system. Given a set of coordinates

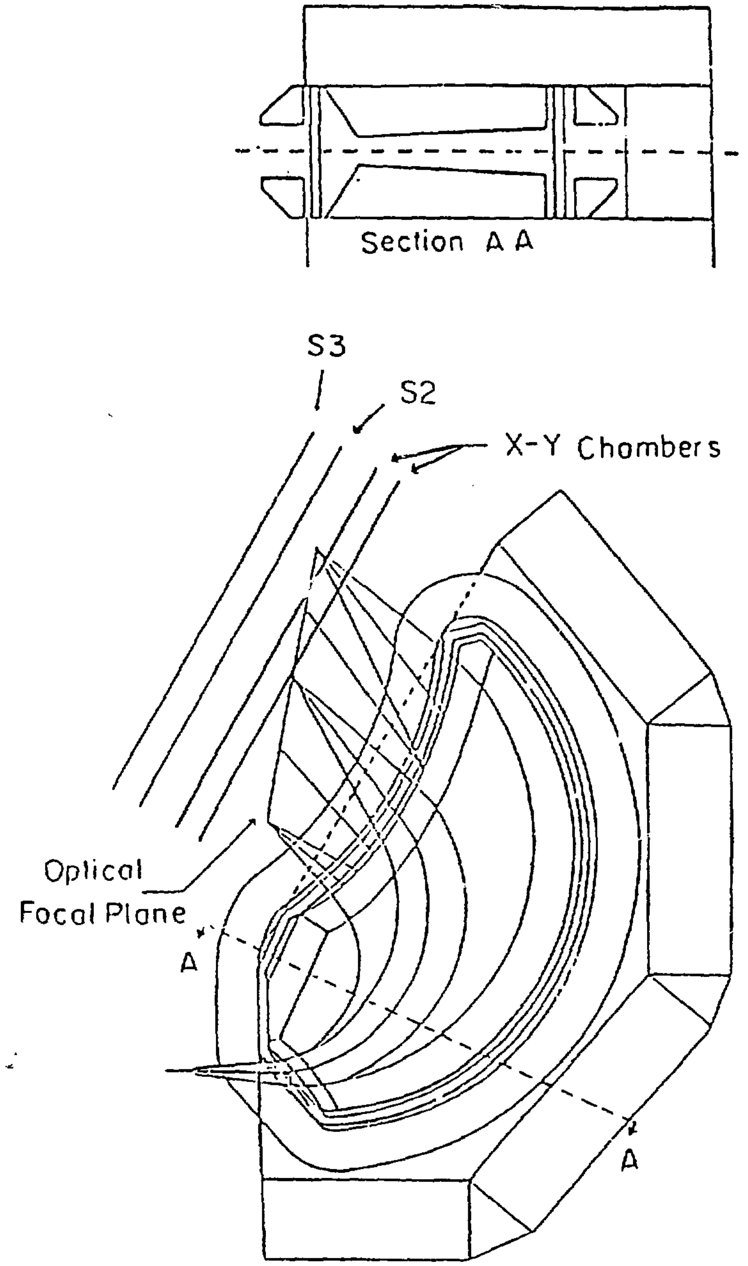

Figure 2.4 The Clamshell spectrometer and its detector array. The cutaway view shows the nonuniform gap between the magnet's pole faces.

characterizing the trajectory of a particle at the target, the problem of interest is: what does one expect the particle's coordinates to be after traversing the magnetic system? A convenient set of variables is the set $x, \theta, y, \phi, l, \delta$ where θ is dx/dz, ϕ is dy/dz, δ is the momentum difference from the central ray, $\frac{p-p_{cp}}{p_{cp}}$, and l is the path length difference from the central ray. If we picture this set of quantities as a 6-dimensional vector describing the entrance phase space of a particle, then the passage of particles through the system can be represented in a first order treatment by a 6×6 transport matrix acting on the entrance vector to produce the exit vector,

$$X_{out} = \begin{pmatrix} x \\ \theta \\ y \\ \phi \\ l \\ \delta \end{pmatrix}_{out} = \begin{pmatrix} R_{11} & R_{12} & \dots & R_{16} \\ R_{21} & R_{22} & \dots & R_{26} \\ \vdots & \vdots & \ddots & \vdots \\ R_{61} & R_{62} & \dots & R_{66} \end{pmatrix} \begin{pmatrix} x \\ \theta \\ y \\ \phi \\ l \\ \delta \end{pmatrix}_{in}$$

where, for instance, R_{11} is the magnification of the system and R_{16} is the dispersion of the system. Another notation that is commonly used to specify terms in the transport matrix is $R_{11} = \langle x_{out} | x_{in} \rangle$ which is read x_{out} given x_{in}. For a system like the Clamshell which has midplane symmetry, utilizes only static fields, and for which the five exit quantities x, θ, y, ϕ, and δ are independent of l the transport matrix takes on the following much simplified form.

$$\begin{pmatrix} R_{11} & R_{12} & 0 & 0 & 0 & R_{16} \\ R_{21} & R_{22} & 0 & 0 & 0 & R_{26} \\ 0 & 0 & R_{33} & R_{34} & 0 & 0 \\ 0 & 0 & R_{43} & R_{44} & 0 & 0 \\ R_{51} & R_{52} & 0 & 0 & 1 & R_{56} \\ 0 & 0 & 0 & 0 & 0 & 1 \end{pmatrix}$$

The design optics of the Clamshell are point-to-point in the x or dispersion direction and parallel-to-point in the y direction. The implications of these conditions in terms of Transport language [Bro 80] are as follows. Point-to-point in x means that x is only a strong funtion of δ and that $R_{12} = 0$. Practically these conditions assure that if a monoenergetic, divergent beam emerges from a point on the target, these particles will be focused to a point in $x_{focalplane}$. Parallel-to-point in the y direction means that particles which emerge from the target on parallel trajectories are focused to a point in $y_{focalplane}$. In Transport language this means that the term y given ϕ or R_{34} is the dominant term for obtaining $y_{focalplane}$, or equivalently that $R_{33} = 0$. Since, in practice, measurements of positions and angles are made at the focal plane and the quantities of interest are the corresponding quantities at the target, it is often interesting to run time backward through the above discussion and generate target quantities given the focal plane quantities, i.e. it would be nice to invert the transport matrix. It should be recalled that the treatment here is only to first order and that higher order terms do appear in practice. Also some of the first order terms which one would like to be zero may not be exactly zero due to misalignments; hence the above is only a guide to the actual optics of this device. Reference should be made to the magnet entrance and exit boundaries which were machined in the shape of high order polynomials (as opposed to being straight edges) so as to reduce certain aberrations of the system.

The inversion mentioned above is in fact done and is the basis for the polynomial traceback routines that are employed at LAMPF. After a particle has traversed the spectrometer, its position and exit angles are recorded by an array of detectors in the focal plane. These quantities are then used to calculate the target quantities of interest. During the development periods a great deal of time was spent trying to optimize the coefficients used by these routines and a basic understanding of this procedure is essential to an understanding of the device. Assume that the focal plane quantities X_{out} are known and that it is desired to calculate the target quantities from them. It is supposed that the relationships between the two sets of variables take the form of a polynomial. For instance

$$y_{tgt} = a_0 + a_1 y_{fp} + a_2 \phi_{fp} + \cdots + a_n y_{fp}^2 + \cdots + a_m y_{fp}^q \phi_{fp}^r + \cdots$$

where the a_m are fixed coefficients which are to be found. The method for doing this is amazingly straightforward. Using the example of y_{tgt}, one takes data with a set of targets that are well localized in the y direction, in our case a set of vertical carbon rods. Then for each particle one writes a 'ray' (the set of quantities X_{out}) and by using the known value of y_{tgt} one can solve a system of equations using standard linear techniques for the unknown coefficients. The system is typically over-determined with perhaps 1000 equations (one for each 'ray') and only 10 or 20 unknowns (the polynomial coefficients). Similar tricks are employed to determine other target quantities. For example, ϕ_{tgt} is found by using vertical rod targets and vertical slits to mask the spectrometer entrance so that all the events are well localized in ϕ, and the procedure for θ_{tgt} is the same except horizontal rods and slits are employed. These polynomials are then used in the reconstruction of standard data. The polynomials used by the computer are stored in a file named `POL.DAT`. A sample `POL.DAT` file and instructions for reading it are in Appendix B.

The Detectors

At the exit of the spectrometer the particles encounter an array of detectors which includes two plastic scintillator counters designated S2 and S3 (S1 is a counter which will become available for use at the entrance to the spectrometer, but was not used during these measurements) and two sets of x-y drift chambers. After this experiment was performed another counter S4 was installed to aid in background rejection. It is from these counters that the pertinent information about the particle's trajectory is obtained. The planes in which the detectors lie are not parallel to the optical focal plane. Instead the detector planes are rotated 19 degrees with respect to the optical focal plane. This is done so that the detected particles are closer to normal incidence and so that the lower end of the first wire chamber is isolated from the exit fringe field of the spectrometer.

The scintillators S2 and S3 are 15 cm by 80 and 90 cm, respectively. They are aligned in the dispersion direction and have phototubes at both ends. They are both $\frac{1}{4}$ in. thick, so a pion whose kinetic energy is 65 MeV will on average deposit $\approx$ 2.7 MeV in the counter while creating $\approx$ 30 photoelectrons (this number neglects the quantum efficiency of the tube) in the process. The two ends are designated S2(S3)N or S2(S3)P for negative or positive delta (low or high momentum side of the Clamshell). The use of two photo tubes allows one to do mean timing and to calculate mean pulse heights. This is important in counters of this length in order to get output signals that are reasonably independent of the position of impact. The anode signals were fed from the experimental area directly to the counting house on coaxial cables. Once inside, the signals were fed to time to digital converters (TDCs), amplitude to digital converters (ADCs) and scalers.

The wire chambers [Mor 78][Mor 82] are exactly like the chambers employed at the Energetic Pion Channel and Spectrometer, EPICS. They measure 90 cm by 30 cm and are mounted along the dispersion direction of the spectrometer exit. The chambers are of the alternating gradient type and utilize a delay line instead of individual wire readout. The anode wires are all bussed to a delay line which has a characteristic time of 2.5 ns/cm. Signals from both ends of the line are examined to obtain position information. The cathode wires are bussed together in two groups designated even and odd, i.e. every other wire is bussed together. The position of a charged particle passing through the chamber is determined by collecting the avalanche on an anode wire and passing this signal to the delay line. Suppose that there are N wires in the chamber and that the detected particle produced a signal on the m^{th} wire as counted from the left of the chamber. If the characteristic time per wire spacing on the delay line is t_c and the amount of time for the avalanche to drift from the point of impact to the anode wire is τ_{dr}, then the time measured at the left end of the delay line is

$$T_L = mt_c + \tau_{dr}$$

and the corresponding time on the right end of the line is

$$T_R = (N - m)t_c + \tau_{dr}.$$

The two quantities that are of interest are the sum and difference of these times.

$$T_L - T_R = 2mt_c - Nt_c \text{ and } T_L + T_R = 2\tau_{dr} + Nt_c$$

Examination of the above reveals that the difference identifies the wire that was struck and the sum is proportional to (with an offset) the drift time. It is clear that the position resolution is the wire spacing (8 mm in these chambers) as it cannot be specified on which side of the anode wire the particle passed. This is the so called left-right ambiguity and it is resolved by examining the induced cathode pulses. If a particle passes on the right side of an anode wire then (see Figure 2.5) the nearest cathode wire (an odd wire in the figure) will get a larger induced pulse than the cathode wire on the opposite side of that anode (an even wire in the figure). Thus if one looks at the cathode pulses and forms the quantity odd−even (the difference of the induced pulse heights) the left right ambiguity is removed as this quantity is positive on one side of a given anode and negative on the other.

It should be pointed out that both T_L and T_R above are referenced to a time signal from the S2 scintillator. Therefore it is important that this scintillator be near the chamber so that fluctuations in the start time due to particles of different momenta are minimal.

The cathode is at ground and the anode is held at positive high voltage relative to it. The raw anode signals are reasonably small, only 1-3 mV in amplitude. This should be compared to the raw scintillator pulse heights of approximately 100-500 mV. For this reason the anode signals are fed into a pair of bridged ×10 amplifiers, which give a net ×100 gain, and are then sent to constant fraction discriminators to provide good timing

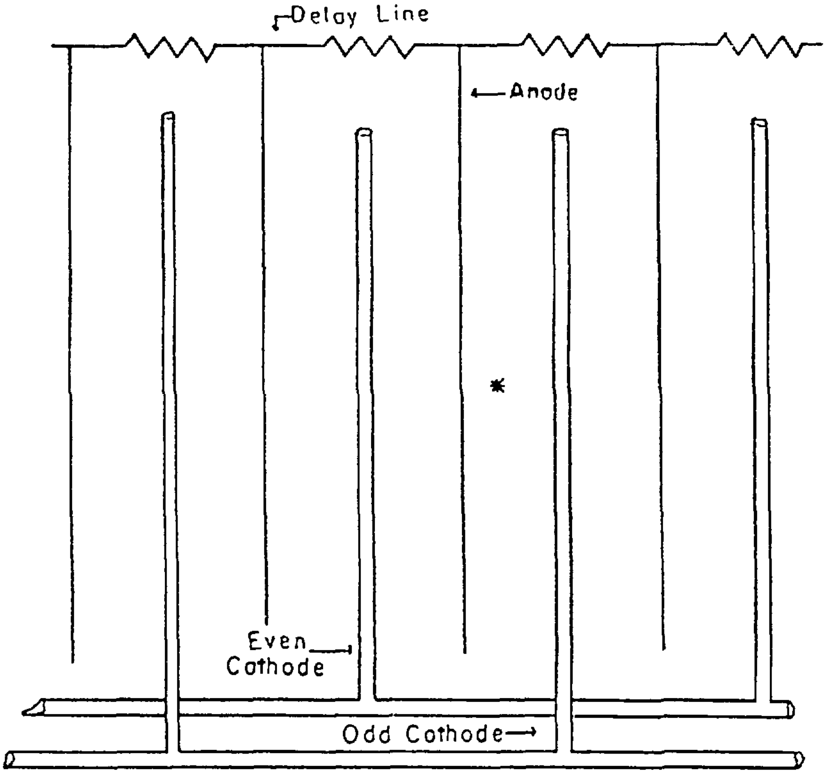

Figure 2.5. A schematic view of one of the drift chambers in the detector array. The * denotes passage of a particle.

signals. Finally these discriminated signals are sent to the counting house and fed into TDCs. The cathode signals are sent to amplifiers and then to the difference circuits which produce the odd—even output. This output, with a D.C. offset, is then fed into an ADC.

The chambers are filled with gas at atmospheric pressure. This gas is a mixture of argon, because it is inert, isobutane, because it is electronegative thus helping to quench the avalanches, and alcohol which prevents the isobutane from polymerizing on the wires. During this experiment the gas came from the EPICS gas handling system and was monitored at bubblers located at the exit side of the chamber gas flow.

The wire chambers require calibration and for completness a brief description of this procedure will be presented. First and foremost it is crucial that all the hardware be working properly. There are several online checks that can be made. These are made by utilizing a special set of histograms which are designed to give chamber information. These include histograms of the truncated x and y positions and the crude x and y positions in the focal plane. These truncated and crude positions have no drift time information so individual wires should be visible in these histograms. The calibration of the chambers involves a least squares fitting procedure to determine the coefficients needed to convert measured times to distances. For instance the crude x position in the focal plane is given by an expression [Ate 81]

$$x_{crude} = a_0 + a_1(T_L - T_R) + a_2(T_L - T_R)^2.$$

The coefficients, a_n, describe signal propagation along the delay line and are determined by fitting to the wire positions. The truncated positions are defined from the crude positions by

$$x_{trunc} = Int(\frac{x_{crude}}{w}) \times w,$$

where w is the wire spacing and $Int(x)$ is a function that forms a integer by truncating its argument [Mor 82]. The actual determination of the coefficients used in the calculation of x_{crude} is accomplished by minimizing the quantity

$$\chi^2 = \sum_{i=1}^{n} (x^i_{crude} - x^i_{trunc})^2,$$

where the sum is over a large number of events, n. The drift time to drift distance conversion is found by integrating the drift time histogram as described in Atencio et al [Ate 81]. The function that converts from drift times to drift distances is then stored in lookup table. After the delay line has been calibrated and the drift distance lookup table is in place it is necessary to decide whether to add or subtract the drift distance to the truncated position. This is determined by trial and error. A properly calibrated chamber has a position resolution of about 250 μm.

The Electronics

The electronics directly associated with the chambers and the scintillators were discussed previously. It is appropriate now to make a few general comments on the fast electronics that were used. The raw signals from both scintillators and chambers are first processed (amplified, fanned out for distribution, discriminated, pulse shaped) in the NIM bins. These NIM standard pulses are then fed to CAMAC modules (TDCs, ADCs, scalers) for digitizing. Unlike the NIM bins, which are just power supplies for the individual pieces of electronics in them, CAMAC crates are set up so that the

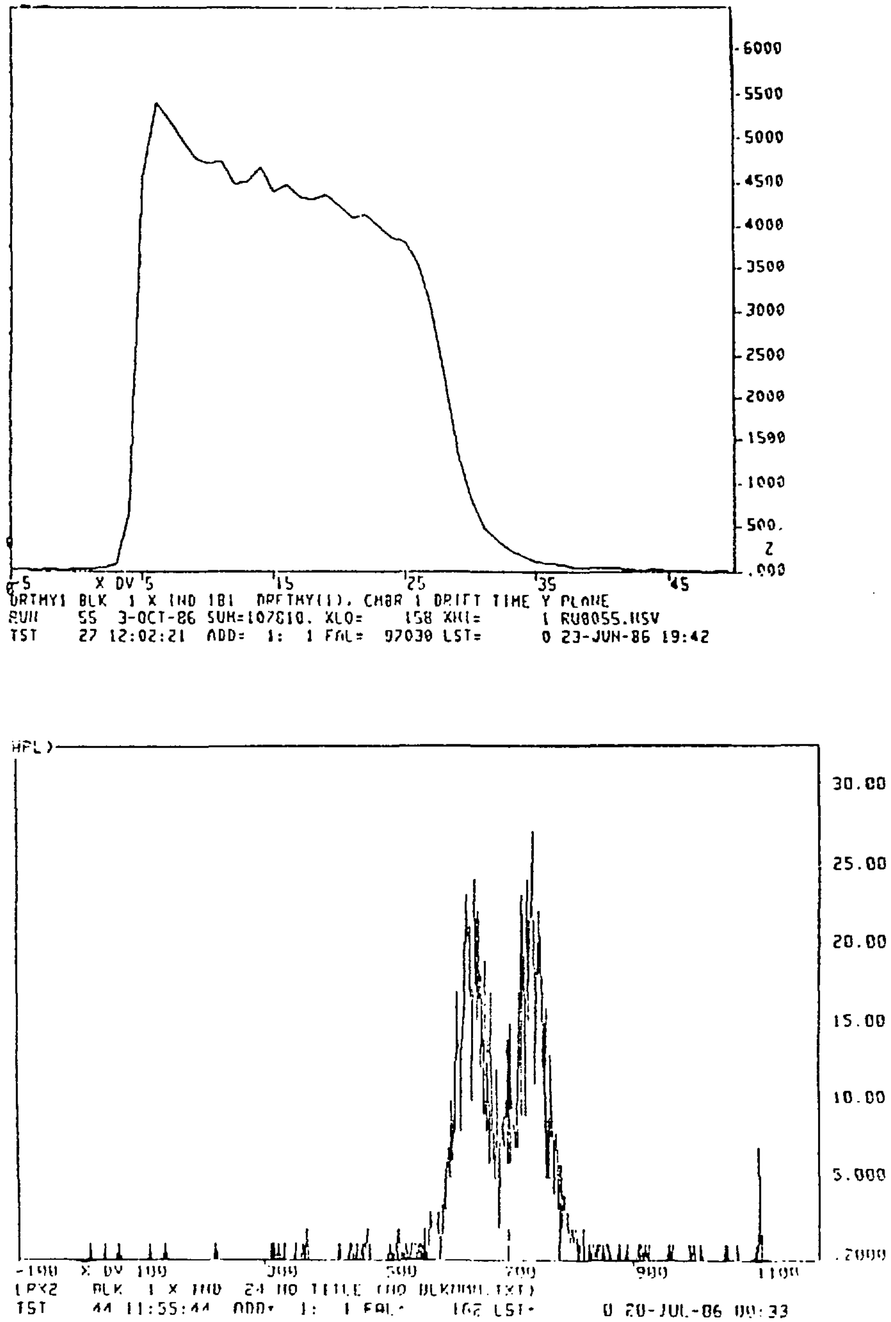

Figure 2.6 Two histograms that display chamber information. a.) The characteristic drift time distribution. The width of the bump corresponds to $\frac{1}{2}$ the wire spacing. b.) The output of the odd–even ADC from a LAMPF drift chamber.

individual units can all talk to the crate controller over the crate's data-way and different crates can communicate over the branch highway. The information in the CAMAC crates must be read out. This is accomplished by using the LAMPF trigger module which polls the crates and checks priorities so as to simplify the job of the Micro-programable Branch Driver (MBD) which is the real interface between the CAMAC and the Micro-VAX that was used for data acquisition. The hardware trigger, the set of conditions that must be met before an event is recorded, required that both scintillators S2 and S3 fire in coincidence and that this coincidence be accompanied by a signal on any two of the four delay lines. In addition to the above condition, it was demanded that a beam gate, a run gate and a computer not busy signal be present. The beam gate indicates the presence of a macro pulse on line A. The run gate insures that a run is in progress. The computer not busy signal is generated by the LAMPF trigger module to indicate that it is ready to accept signals. These conditions can be written

$$\text{Event} = S2 \cdot \text{S3} \cdot \text{any two delay lines}$$

$$\overline{\text{veto}} = \overline{\text{computer busy}} \cdot \overline{\text{not beam gate}} \cdot \overline{\text{not run gate}},$$

where the dots denote that a coincidence of the signals is required and the overbars indicate negation. Using the above notation, the trigger can then be written Trigger = Event $\cdot\,\overline{\text{veto}}$. One purpose of this hardware trigger is to try to minimize the number of bad events written to tape.

Data Acquisition and Replay

The data acquisition and replay were implemented using a specialized version of the EPICS Q system. The Q system is a complex software package (with some specific hardware, MBD and trigger module, required for data acquistion) designed at LAMPF with maximum flexibility in mind. As a complete description of Q (see for instance, The Q-Users Information Manual) would require several hundred pages, only an overview will be given here. Figure 2.7 shows the basic architecture of the Q system. The analyzer is the heart of the Q system and contains all the software that actually assimilates data on an event-by-event basis and contains the routines that calculate all quantities such as missing mass. Perhaps the most important of these routines is `PROC 5` which processes the 'real events' (the EPICS equivalent is `PROC 6`). The general purpose management region is a large common block through which all the Q subsystems access information. For the typical user the systems that are most often dealt with are the histogram plotting package (HPL) and the data testing package. HPL enables one to make either one parameter or two parameter histograms of any defined data word, a name given to the quantities dealt with in the software. The histogram package is intimately conected with the test package which allows one to select and histogram subsets of the raw data which pass certain user defined criteria. In addition one can use HPL to specify boxes and gates to be used as tests. To demonstrate the system, Appendix C contains copies of several files of interest. These include `BLK001.TXT`, which is a list of all the data words appropriate to the experiment, a schematic version of `EXP813.TST` which is the data test file that was used in analysis, and excerpts from a typical histogram setup file, `EXP813.HST`, as well as instructions for interpreting these files where they might be useful. Another important feature of Q is the dynamic parameter array which provides dynamically adjustable variables (both I*2 and R*4). It is here that things like calibration offsets, kinematic parameters and processing flags are stored.

The final peak areas were extracted from the missing mass histogram labelled MMASSC. Missing mass is basically an excitation energy spectrum. It is calculated by the subroutine `CALKIN`. The explicit expression for missing mass (denoted Q) is

$$(Q + m_d)^2 + p_d^2 = (E_{miss} + m_d)^2.$$

The quantity E_{miss} is given by

$$E_{miss} = (T_a + m_a) + m_b - \sqrt{p_c^2 + m_c^2} - m_d,$$

where the subcripts refer to the usual convention for reactions, $b(a,c)d$ (for this work $^{13}C(\pi,\pi)^{13}C$). T_a and all the masses are known (the masses are stored in a lookup table). The outgoing pion's momentum, actually its momentum difference, δ, is calculated as a polynomial in exit quantities (see Appendix B). The leading term in this polynomial is the term proportional to $x_{focalplane}$. The last uncalculated quantity in the above expressions is the momentum of the recoil particle, p_d. In order to calculate this one needs to know the scattering angle, θ. This angle is

$$\theta = \theta_{spec} + \phi_{tgt},$$

where θ_{spec} is the angle of the spectrometer relative to the incoming beam and ϕ_{tgt} is calculated as a polynomial in the the exit quantities. The rest of the calculation is rather straightforward kinematics. The final missing mass histogram (MMASSC) was subject to test 106 in the test file (see

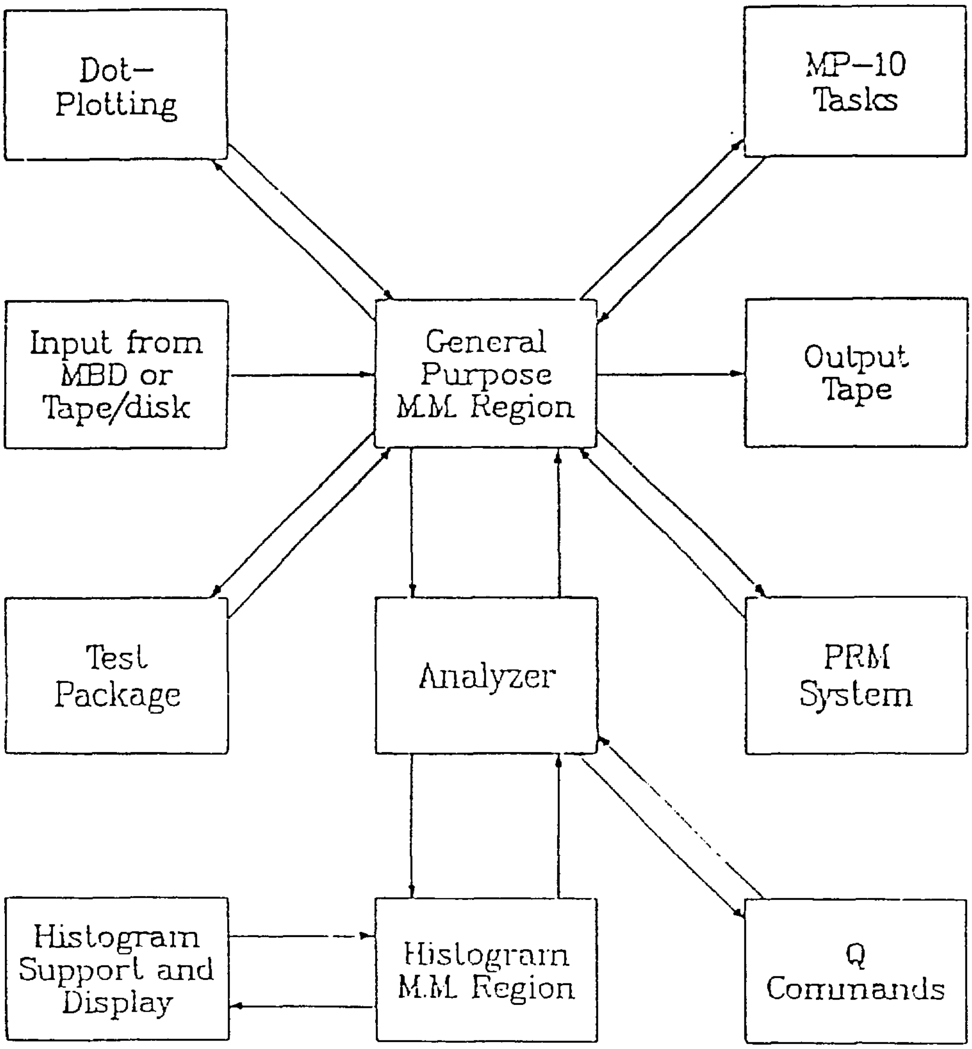

Figure 2.7 The structure of the Los Alamos Q system [Ama 86].

Appendix C). This test is a compound test formed by taking the Logical And of the group of tests collectively called *good chambers*, the group *good focal plane*, the group *good target*, and the particle identification boxes (PID's). A compound test formed by taking the Logical And of two tests is true if and only if both its constituent tests are true. *Good chambers* guarantees that the event in question had signals on both ends of the delay lines of both sets of x and y chambers and that the drift times calculated were within acceptable limits. *Good focal plane* is formed by the Logical And of a series of tests which are gates on the focal plane quantities x_{fp},θ_{fp} ,ϕ_{fp}, and y_{fp}. *Good target* is a similar test performed on the analogous target quantities y_{tgt}, θ_{tgt}, and ϕ_{tgt} (x_{tgt} is not a calculable quantity for this device). These focal plane and target gates were set very loosely and do not constitute a very severe restriction on the data. The PID's, the final component of this composite test, deserves some added attention. Backgrounds at the Clamshell are reasonably high and their reduction presented a major challenge. These backgrounds stem from several major sources: first there are a large number of neutrons in the experimental area, and second there was no detector at the object side (target side) of the spectrometer to insure that all particles encountered at the focal plane had traversed the spectrometer. The second is a particularly important point as particles could easily get to the focal plane without passing through the magnet due to the physically close proximity of the focal plane detectors and the top of the scattering chamber. The third source of background is due to Coulomb scattering of beam contaminate electrons and muons. The PID cut that was finally employed uses the fact that pions at the energies of this experiment, $T_\pi < 65$ Mev, are not minimum ionizing, and in fact their dE/dx

rises rather sharply as their kinetic energy drops. The actual cut was made by first making a dot plot of missing mass vs. the mean pulse height in S2. The results of such a plot are shown in Figure 2.8. Scintillator pulse height in a passing detector is proportional to the rate of energy loss of the detected particle. Hence the curved band of particles in the plot represents pions and possibly muons while the lower straight band is most likely electrons which are almost always minimum ionizing. Now, since the boxes used for defining tests in the Q test package must be rectangular, it was necessary to make the pion band into a straight line. To this end two new data words were defined, S2PRMM and S3PRMM. These were calculated by first fitting the equation of a curve that seemed to typify the pion distribution in the dot-plot and then using these coeffiecients in `POL.DAT` to straighten out the parabola. A final dot-plot showing missing mass vs. S2PRMM is shown in Figure 2.9 and the PID box is indicated. The same sort of test was performed on S3PRMM to provide some redundancy. To insure that the tests were functioning properly, rejected spectra were histogrammed and in a typical case it was found that less than 4% of events that represent scattering to the ground state or the two large collective states at 3.68 MeV and 7.55 MeV in excitation were being rejected by the box cuts and more importantly, that the percentage of rejected events that were presumably good remained constant across the focal plane.

Peak Fitting

The final peak fitting was done using the Colorado code `SPECTR`. This requires that the Q format histograms first be put into a format that

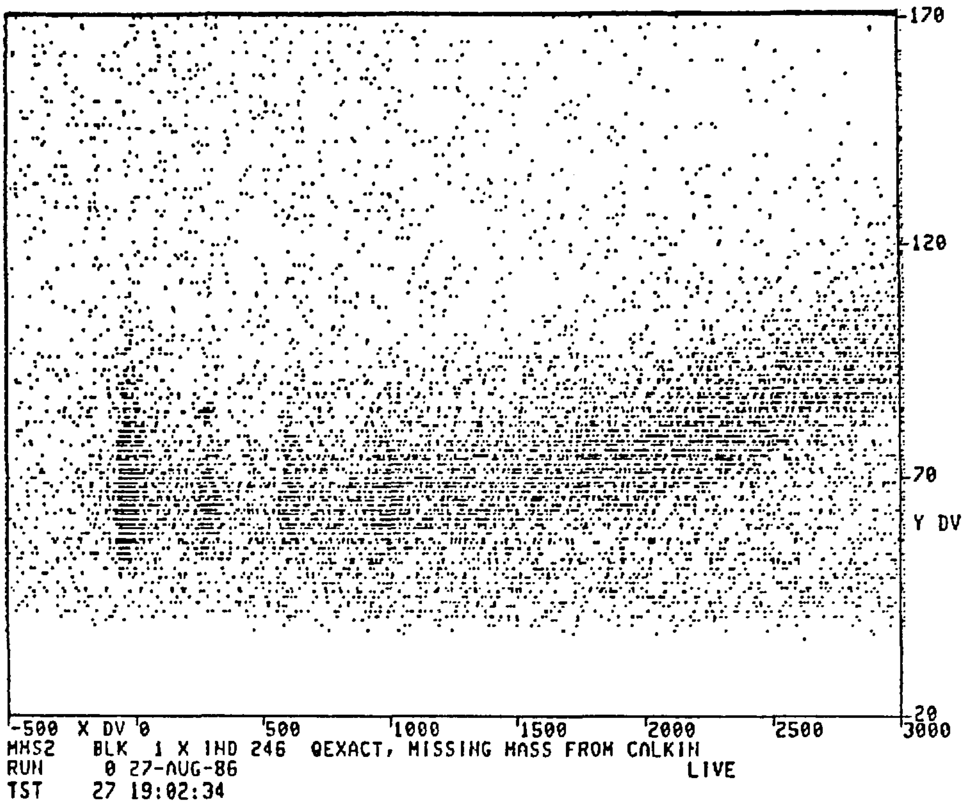

Figure 2.8 A dot-plot of the pulse height from the scintillator S2 against the missing mass of the particles. The curved band consist of pions and some muons.

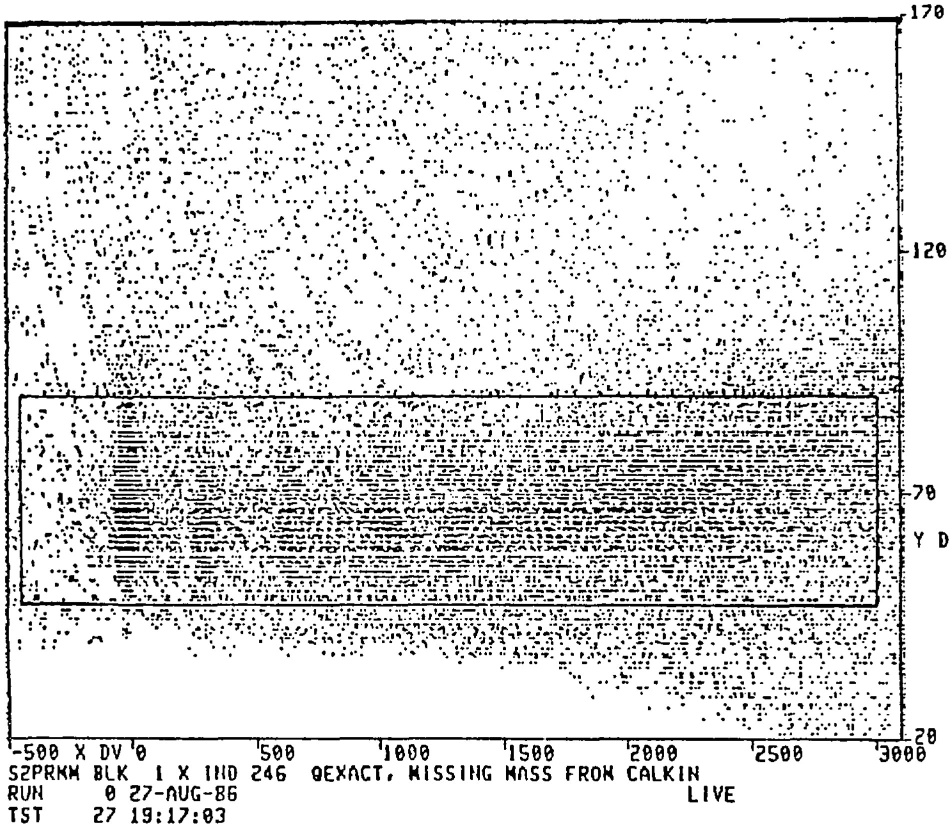

Figure 2.9 A dot-plot of the 'corrected' pulse height from the scintillator S2 against the missing mass of the particles. The particle identification box (PID) is shown.

is compatable with SPECTR. The software for this translation was already in place and so this presented no difficulties. Once the files were in SPECTR format it was necessary to get a good energy calibration of the ^{13}C spectra. The centroids of peaks with known excitations were used in a least squares fitting routine to obtain the appropriate slope in channels/MeV. The states in ^{13}C that were used in this calibration were the ground state and the excitations at 3.68 MeV, 7.55 MeV, and 8.86 MeV. There was some worry that the collective states in ^{13}C (in particular the states at 3.68 MeV and 7.55 MeV) would contain unresolved doublets. Strictly speaking this is true but the other unresolved states were expected to be much weaker and hence not effect the calibrations. Even so, the energy calibration was checked against calibrations obtained from the elastic, 4.44 MeV, 7.65 MeV and 9.64 MeV states in the ^{12}C spectra which were taken for this purpose as well as for background subtraction and normalization. The two results were found to be in good agreement.

At this point the real peak fitting was done. The peak shape was taken to be an asymmetric Gaussian whose parameters were fixed by fitting the elastic peak. The separations of the peaks were fixed at their known excitation energies using the energy calibration. The backgrounds were chosen to be linear and fixed. The effect of the choice of background on the extracted areas was investigated by varying both the slope and intercept of the background over reasonable limits. In this scheme then the only real freedom in the fitting routine is the height of the peaks. This procedure was chosen in an attempt to eliminate prejudice in extracting the areas of the 9.5 MeV state. Figure 2.10 shows two sample spectra, one for π^+ and one for

π^-. They show the peak shape and the energy calibration. It is apparent that the elastic and presumably all the other peaks have a low energy tail that is not adequately described by the reference peak shape. This was accounted for by adding by hand the estimated contribution of this tail to the areas of the peaks. This was typically a 3% correction and the error in this procedure was folded in with the statistical errors. In addition, the effect of the tail from the elastic peak on extracted areas for the low lying states was investigated by mocking up the tail with a background.

Resolution

The spectra obtained in this experiment have an energy resolution of about 510 keV full width half maximum. For the data taken at 65 MeV this can be broken down in the following way:

$$(\Delta E)^2 = (\Delta E_{tgt})^2 + (\Delta E_{beam})^2 + (\Delta E_{spec})^2$$

where

$$\Delta E = \text{total resolution of the system} \approx 510 \text{ keV}$$

$$\Delta E_{tgt} = \text{contribution from target} \approx 280 \text{ keV at } \theta_{\text{tgt}} = 42 \text{ deg}$$

$$\Delta E_{beam} = \text{contribution from channel tune} \approx 170 \text{ keV}$$

$$\Delta E_{spec} = \text{all other contributions} \approx 390 \text{ keV.}$$

Some of the above require additional explanation. The ^{13}C target had an areal density of 203 ± 3 mg/cm^2 and was isotopically enriched to 99% purity. The density was determined by weighing the target and dividing this weight by the target's measured area. The uncertainty in the areal density is almost

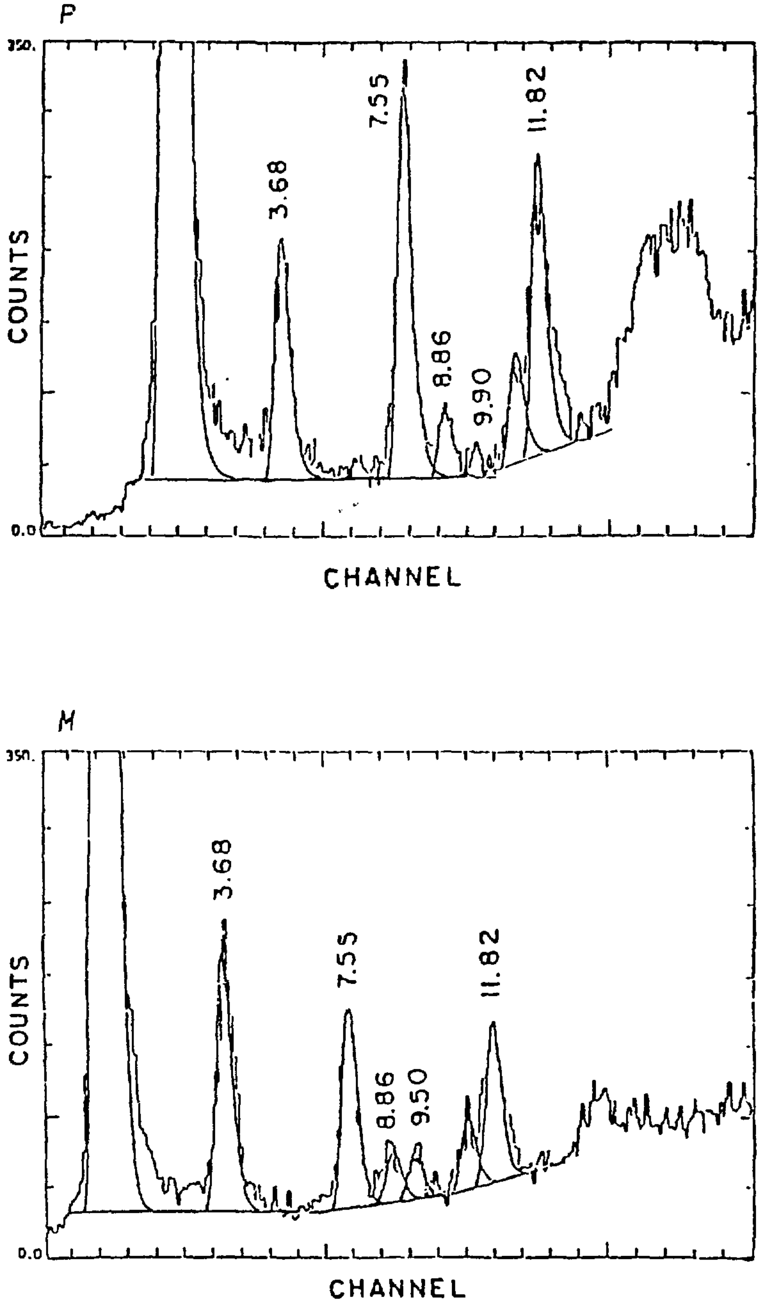

Figure 2.10 Representative missing mass spectra for the scattering of both positive and negative pions from ^{13}C. The data were taken at a lab angle of 105 degrees and have a resolution of approximately 510 keV.

all from the area measurement. This target is a small piece of the target used by Seestrom-Morris for her measurements which were performed at EPICS [See 81]. The target was always placed in transmission geometry with the target angle equal to one half the scattering angle.. Therefore, for elastic events, only the straggling, not the energy loss, contributed to the resolution. The above is a crude estimate that the straggling is approximately 1/3 of the energy loss. The contribution from the channel reflects the spread in energy of pions in the incoming beam. During the taking of the 65 MeV data the momentum spread in the incoming beam was, $\Delta p/p = 0.15\%$. The last term, ΔE_{spec}, is perhaps the most interesting. It was found empirically from the measured resolution and all the other terms. This term should account for such things as the finite positional resolution in the wire chambers and polynomials which are not perfectly optimzed.

Differential Cross Sections

The quantity of interest is the differential cross section $\frac{d\sigma}{d\Omega}$. This quantity is defined by the ratio of the number of interactions per target particle that lead to scattering into a solid angle $d\Omega$ at an angle θ to the number of incoming particles. In practicle terms $\frac{d\sigma}{d\Omega}$ can be written (noting that this is not the same notation used on the SHT computer outputs at LAMPF)

$$\frac{d\sigma}{d\Omega}_{c.m.} = \frac{(Yield)(CorrFac)(Jacobian)}{(Number\ of\ target\ nucleons)(\alpha d\Omega)(\eta_{fp})(Survival\ Fraction)},$$

where

$$(Number\ of\ target\ nucleons) = \frac{\rho_{tgt} \times N_A}{\cos\theta_{tgt} \times A}.$$

Here,

$$\rho_{tgt} \text{ has units of } \frac{\text{mg}}{\text{cm}^2},$$

so

$$(Number\ of\ target\ nucleons)\text{has units of } \frac{\#}{\text{cm}^2}$$

and

$$N_A = Avogadro's\ number \text{ and } A = N + Z.$$

The remaining factors will be discussed in more detail.

$CorrFac$ contains all the efficiency factors that are expected to be independent of δ, such as computer live time, chamber efficiencies and drift efficiencies. It can be expressed

$$CorrFac = 1/(CompLt \times ChmbrEff \times \frac{Loop}{Event} \times DriftEff).$$

The chamber efficiency is the product of eight terms, one for each end of all the delay lines (there are two chambers and each chamber has both an x and y delay line). Each of these terms is a ratio of the form

$$\frac{\text{number of events with a signal at both ends of the delay line}}{\text{number of events with signal at one end of the delay line.}}$$

In order to define the drift efficiency it will be useful to make some other definitions first. Events that pass the test *Good Anodes* are those events which had signals at both ends of all four delay lines. Events that pass the test *Good Chambers* are events that passed *Good Anodes* which also have reasonable drift times (ie. have drift times that fall within the gates set on the histograms). The Drift efficiency is the ratio of those events that passed *Good Chambers* to those events that passed *Good Anodes*. These chamber effiencies are of course only relative. The actual method chosen for their calculation is not critical as any scaling factor will cancel out in a relative measurement (the meaning of "relative measurement" is discussed below). The computer live time is the fraction of events for which the computer was not busy. Loops per event is the fraction of events for which the analyser is called and is 1.0 for replayed runs. The dimensionless factor, Corr Fac, was typically about 1.2 for the data runs in these measurments.

Yield, as defined here, contains the number of counts in the peak of interest divided by a scaler called a relative monitor count which is presumed to be proportional to the number of incident pions. This experiment utilized several different relative monitors. TOR1 is a toroidal counter positioned around line A that has a current induced in it that is proportional to the charge in the primary proton beam near the A-1 production target. TOR2 is a similar device that is located further downstream on line A near the A-2 production target. Finally, BOT is an ion chamber that views the spallation products coming off the A-1 target.

In addition to the above monitors, all of which either directly or indirectly view the primary proton beam, there were two in-cave monitors. These two monitors , called π-μ telescopes, were mounted on the LEP beam pipe just upstream of the scattering chamber in the cave. Each telescope consisted of two scintillator counters set up to view the muons resulting from pion decays in the beam (see Appendix D on pion decay). The ratios of all the monitors to the A-1 toroid (TOR1) were checked and all were found to be constant except the ratio of π-μ counts to TOR1, which exhibited some bounce. These irregularities coincided with movements of the spectrometer, angle changes, leading one to the conclusion that they are a reflection of the strong fringe magnetic fields associated with the Clamshell. This made it impractical to use these in-cave monitors as the beam monitors. This is not optimal, as none of the other monitors provide as direct a measurement of the pion flux. However, it has been found in the past that the number of pions in the LEP beam is not very sensitive to variables such as the position of the primary proton beam on the A-1 production target [Fra 83]. Also in experiments performed at EPICS it has been found that the ratio of in-cave monitor counts (at EPICS these in-cave monitors are ion chambers) to TOR1, TOR2, and BOT is quite constant [Ull 86a]. So although it is not ideal, the lack of in-cave monitors is not a catastrophe. Due to this problem with the muon telescopes and the fact that all the other relative monitors were consistent, TOR1 was arbitrarily chosen for the analysis of this data. Therefore the quantity designated $Yield$ is given by the ratio of counts in the peak of interest to the beam scaler TOR1.

The next factor of interest is designated $\alpha d\Omega$. At LEP neither the absolute solid angle of the Clamshell (the solid angle is approximately 40 msr) nor the actual number of pions incident on target is known. Therefore the common practice is to make measurements relative to a known cross section. In fact, what one is doing in these relative measurements is using a known cross section to measure the product of the spectrometer solid angle, $d\Omega$, and the quantity α which is equal to the number of incident pions per relative monitor count.

The factor η_{fp} is another factor that is measured experimentally. This represents the change in detection efficiency as a function of δ (δ =

$\frac{p-p_{op}}{p_{op}}$) or position on the focal plane. This quantity is given many names in the literature. A few of these are the relative solid angle, the acceptance, or the focal plane efficiency. This quantity is mapped out by doing a δ-scan, in which the procedure is to look at pions elastically scattered from a large Z target, chosen for quick counting and minimum kinematic broadening. This is done for several settings of the spectrometer's magnetic field at a fixed scattering angle, so that the only things differing from run to run are the position of the peak on the focal plane, the amount of run time, and the survival fraction of the outgoing pions. All of these effects except the first are eliminated if one plots the quantity

$$\frac{(Yield)(CorrFac)}{(Survival fraction)}$$

as a function of δ. This was done and Figure 2.11 shows the results of this procedure found by scattering positive pions whose kinetic energy was 65 MeV from lead. Each point has a maximum statistical error of 3 %. The normalization of η_{fp} is arbitrary as it also appears in the measurement of $\alpha d\Omega$ and hence any normalization will cancel. The quantity that enters cross sections is the ratio of the η_{fp} used in the determination of $\alpha d\Omega$ to the value of η_{fp} for the peak of interest.

Since pions have a finite lifetime a correction must be made for pions that scattered at the target but decayed before reaching the detectors. The derivation of this correction is straightforward and it is shown in Appendix D. The final factor in the expression for $\frac{d\sigma}{d\Omega}$ is the familiar Jacobian which relates the solid angle in the lab to the solid angle in the center of mass.

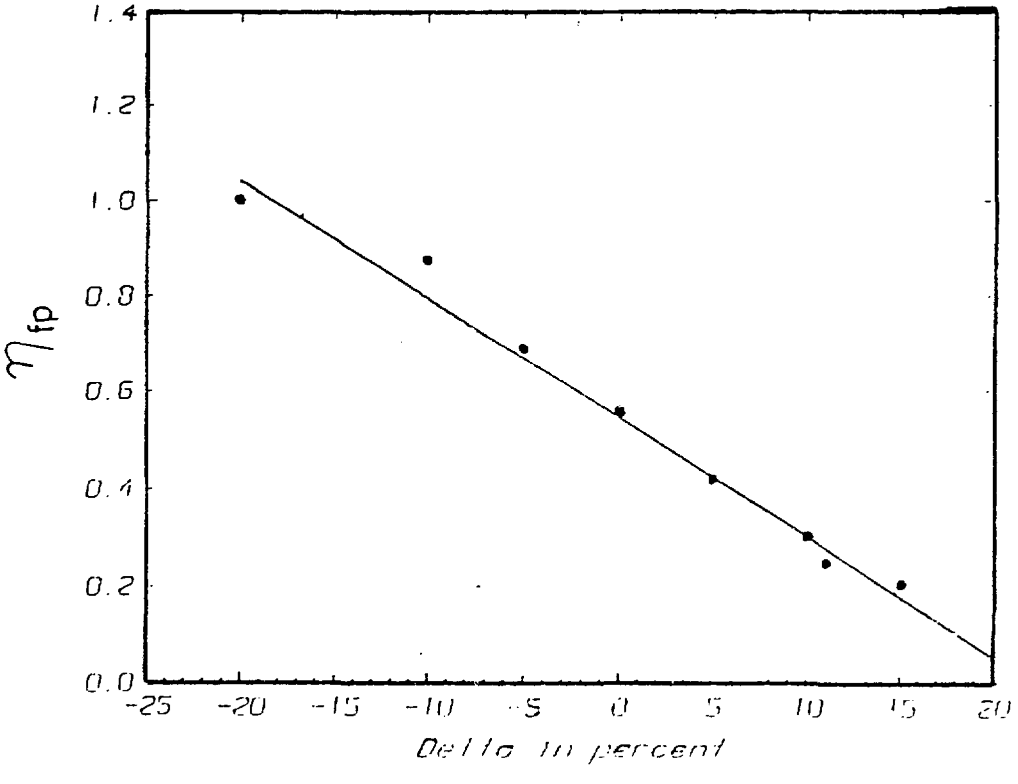

Figure 2.11 The focal plane efficiency, η_{fp} of the Clamshell spectrometer. The line was obtained by a least squares fit to the data.

Normalization Procedure and Systematic Uncertainties

The normalization is determined by the measurement of the product $\alpha d\Omega$. In this experiment $\alpha d\Omega$ was extracted by comparing measurements of pions scattered from a solid CD_2 target to the deuteron data of Balestri et al.[Bal 83]. For redundancy and background subtraction, elastic scattering data from a ^{12}C target were also taken. These ^{12}C measurements were compared to the data of Blecher et al.[Ble 83]. The CD_2 target consisted of several strips which were placed together in the target frame and had a total areal density of 177 ± 3 mg/cm^2. The ^{12}C target had a density of 223 ± 4 mg/cm^2. The presence of carbon in the CD_2 spectra was accounted for by making background subtractions using the companion ^{12}C runs. This process was checked by comparing the results to areas obtained using fixed background at angles where it was expected that no large inelastic carbon peaks would be under the deuterium elastic peak. Several measurements were made for both charges of pions. It was found that all measurements of the quantity $\alpha d\Omega$ made with deuterium agreed to within their statistics and that all measurments of this same quantity made with ^{12}C data were also internally consistent. However, the values of $\alpha d\Omega$ found in these two ways were found to disagree by amounts greater than would have been expected given their errors. This discrepancy is not just due to a poor focal plane normalization (an incorrect value of η_{fp}) as the sign of the difference between the two sets changes with the sign of the pions.

As a matter of policy the following scheme was chosen. The overall π^+ normalization was taken from the π^+ data of Blecher [Ble 83] and the relative normalization for π^- data was established by the π^+/π^- ratio of

Balestri et al. [Bal 83] This scheme was chosen for a number of reasons. Balestri used a range telescope and was able to make checks that the device had the same efficiencies for detection of positive pions and negative pions. In addition, Balestri's experiment was performed at Saclay. This is an electron accelerator and hence π^+ and π^- fluxes are approximately equal. Also Balestri had an in-beam monitor to count both positive and negative pions. All these facts lead to a very high confidence in the ratio of π^+ and π^- cross sections obtained by Balestri. The experiment of Blecher et al. was performed at LEP using the old Bicentennial magnet. Their π^+ measurements were normalized directly to π^+p cross sections. Hence these π^+ measurements should be good within their reported uncertainties. No conclusions of this work are strongly dependent upon this choice, as the discrepancy between the π^+ normalizations from the two sets is of order 20%.

In all figures where cross sections are shown (see chapter 4) only the statistical errors and errors due to uncertainties in the fitting, where present, will be included in the error bars. In addition to these errors there is an overall uncertainty in the normalization of the data. This uncertainty has several independent sources. First there is an the uncertainty associated with the data that were used to normalize this work. The current π^+ data were normalized to the data of Blecher et al.[Ble 83], and hence the normalization uncertainty of 7% associated with those data will contribute. The uncertainties in target thicknesses, 2.5% for the ^{12}C target used to measure $\alpha d\Omega$ and 2% for the ^{13}C target, will also enter. Another source of error is the statistical error in the elastic scattering measurements that were used to determine the product of the solid angle and beam flux, $\alpha d\Omega$. This statistical error was typically 3%. In addition there is an uncertainty associated with the beam monitoring. By checking the agreement of the values $\alpha d\Omega$ which were made with the same target but at different times and angles this contribution to the overall uncertainty is estimated to be less than 6%. Finally, since no muon rejector was used during these measurements and muons cannot be effectively eliminated with pulse height cuts (as electrons can), an estimate of the number of misidentified events is necessary. The LAMPF Users Handbook [LUH 80] estimates that for a beam energy of 50 MeV there is one muon for every ten positive pions in the beam. The time of flight measurements reported by Frank et al.[Fra 83] gave a similar result for π^- beams. Muons interact with the target via electro-weak processes only. For the range of angles over which data were taken, the Rutherford (Coulomb) cross section is never greater than one tenth of the elastic scattering cross section. No data were taken in this experiment at lab angles of less than 45 degrees. This leads to the conclusion that the number of events that should be associated with muons is of the order of 1%. Adding all of the above contributions in quadrature yields an overall uncertainty of 10% for the π^+ data.

In addition to these errors, the π^- data must also include uncertainty in the deuterium cross sections [Bal 83] that were used to determine the relative π^+, π^- normalization. The inclusion of this additional uncertainty yields an overall uncertainty of 11% for the π^- data.

Before presenting all the measured cross sections, scattering theory will be discussed in order to provide a means of interpreting the data.

CHAPTER III

THEORY

In this chapter the theoretical treatment of πA scattering will be considered. The emphasis will be on the distorted wave impulse approximation (DWIA) with medium corrections, as this was the actual method used in the analysis. Before multiple scattering theory is examined in a formal way, it is instructive to look at the general properties of πN scattering and at the optical analogy, in which pion scattering in matter is treated in the same manner as light impinging on an attenuating medium.

The Optical Analogy

In this picture, pions (or any other particle) fall upon a semi–infinite slab that consists of a spatially homogenous array of scattering centers characterized by a density of scatterers, ρ, which is the number of scatterers per unit volume [Kol 80]. The incoming pions are represented by a plane wave propagating in the z direction with a free space wave number, k. It is assumed that the effect of the medium is small in the sense that the wave propagation in the medium is not radically different from that in free space. The usual assumption that the outgoing wave is a sum of the incoming plane wave and a spherical scatterred wave is made. One finds that the wave function $\psi(z)$ for the outgoing particle, after it has traveled a distance s into the medium is

$$\psi(z) = e^{ikz} + 2\pi \int_0^\infty f \frac{e^{ikr}}{r} \rho s b \, db$$

where b is the classical impact parameter. Next it is assumed that ρ is a constant, or at least varies slowly, and that all the scatterers are characterized by the same amplitude, f, so that both are approximately independent of r. Then by noting that $r^2 = b^2 + z^2$ one obtains

$$\psi(z) = e^{ikz} + 2\pi s f \rho \int_z^\infty \frac{e^{ikr}}{r} r \, dr.$$

The integral is evaluated by introducing an exponential factor, $e^{-\lambda r}$, and then letting λ go to zero after integration. Performing the integration gives

$$\psi(z) = e^{ikz}(1 + \frac{i2\pi s f \rho}{k}).$$

If the particle traverses N sheets, each of thickness s, such that the total distance into the medium is $z = Ns$ the result in the large N limit is

$$\psi(z) = \lim_{N \to \infty} e^{ikz}(1 + \frac{i2\pi z f \rho}{kN})^N$$

or

$$\psi(z) = e^{ikz} \exp(\frac{i2\pi z f \rho}{k}).$$

It is customary to define the wave vector in the medium to be

$$\vec{K}_{med} = (1 + \frac{2\pi f \rho}{k^2})\vec{k} = n\vec{k},$$

where n is the index of refraction. Since f is generally complex, so is the index of refraction n. The imaginary part of this effective index of refraction will cause the pion flux in the forward direction to be attenuated exponentially. It is this effect that is known as optical absorption.

If the above wave is taken to be a solution of a wave equation (here taken to be the Schrödinger equation for simplicity) it is then possible to make some rather interesting observations about the potential. Suppose ψ is a solution of

$$(\nabla^2 + k^2)\psi(z) = 2mV\psi(z).$$

Then inserting the expression for the outgoing wave function gives

$$V = \frac{-k^2}{2m}\left(1 + \frac{4\pi f\rho}{k^2} + \left(\frac{2\pi f\rho}{k^2}\right)^2 - 1\right)$$

or in the limit of small f

$$V \approx \frac{-k^2}{m}(n-1) = \frac{-2\pi}{m} f\rho. \tag{3.1}$$

This result is interesting as it implies that the effective potential is complex and that it can be simply related to the fundamental amplitude, f. Models of scattering which employ complex potentials are called optical models and the complex potentials used are called optical potentials. Remembering that the amplitude, f, is proportional to the on-shell t matrix [Tay 72], the result above is a justification of the often used $t\rho$ form for the optical potential. This point will be discussed in more detail later.

The Scattering Amplitude

It is useful to examine the amplitude for πN scattering in some detail since the goal of multiple scattering theory will be to establish a more rigorous connection between the fundamental πN amplitude and the amplitude for πA scattering. The most general form of the amplitude for the scattering of a spin 0 particle and a spin $\frac{1}{2}$ particle that is invariant with respect to spatial inversions (parity),rotations,and time reversal is [Tay 72]

$$F(\vec{k}',\vec{k}) = f\mathbf{1} + ig\hat{n}\cdot\vec{\sigma},$$

where $\hat{n}$ is a unit vector normal to the scattering plane, $\hat{n} = \frac{\vec{k}\times\vec{k}'}{|\vec{k}\times\vec{k}'|}$. For this case the total angular momentum, j, the relative orbital angular momentum, l, and the total isospin, T, are constants of the motion. Therefore, it is convenient to expand the amplitude as follows [Kol 71]

$$F(\vec{k}',\vec{k}) = \sum_T Q_T \sum_l (2l+1) \sum_j P_{l,j}\alpha^l_{2T,2j} P_l(\cos\theta) \tag{3.2}$$

where the Q_T and the $P_{L,j}$ are projection operators defined by

$$Q_{\frac{1}{2}} = \frac{1}{3}(1 - \vec{\phi}\cdot\vec{T}) \qquad Q_{\frac{3}{2}} = \frac{1}{3}(2 + \vec{\phi}\cdot\vec{T})$$

$$P_{l,j=l-\frac{1}{2}} = \frac{l - \vec{\sigma}\cdot\vec{L}}{2l+1} \qquad P_{l,j=l+\frac{1}{2}} = \frac{l + 1 + \vec{\sigma}\cdot\vec{L}}{2l+1}.$$

Here $\vec{\phi}$ is the pion's isospin operator, while $\vec{T}$ is the isospin operator for the nucleon. The $\alpha^l_{2T,2j}$ are related to the π-nucleon phase shifts by

$$\alpha^l_{2T,2j} = \frac{e^{i\delta^l_{2T,2j}} sin(\delta^l_{2T,2j})}{k}.$$

It is helpful to use the following identity

$$\vec{\sigma}\cdot\vec{L} = \vec{\sigma}\cdot(\vec{r}\times\vec{k})$$

and note that

$$\vec{k}P_l(\cos\theta) = -i\vec{\nabla}P_l(\cos\theta) = -i\hat{e}_\theta\frac{1}{r}\frac{\partial}{\partial\theta}P_l(\cos\theta).$$

One gets

$$\vec{\sigma} \cdot \vec{L} P_l(\cos\theta) = +i\vec{\sigma} \cdot \hat{n} P_l'(\cos\theta) \tag{3.3}$$

where

$$P_l'(\cos\theta) = \frac{\partial}{\partial\theta} P_l(\cos\theta).$$

Using equation (3.3) and substituting the explicit form for the angular momentum projection operators into equation (3.2) yields

$$F(\vec{k}', \vec{k}) = \sum_T Q_T \sum_l [(l+1)\alpha^l_{2T,2l+1} + l\alpha^l_{2T,2l-1}] P_l(\cos\theta)$$

$$-i\vec{\sigma} \cdot \hat{n}[\alpha^l_{2T,2l-1} - \alpha^l_{2T,2l+1}] P_l'(\cos\theta).$$

For pion energies around the (3,3) resonance only the s and p-wave terms ($l = 0, 1$) are important. Keeping only these two terms and using the explicit forms of the isospin projection operators gives

$$F(\vec{k}', \vec{k}) = f_{0,0} + f_{1,0}(\vec{\phi} \cdot \vec{T}) + f_{0,1} + f_{1,1}(\vec{\phi} \cdot \vec{T}) \tag{3.4}$$

$$g_{0,1}(\vec{\sigma} \cdot \hat{n}) + g_{1,1}(\vec{\sigma} \cdot \hat{n})(\vec{\phi} \cdot \vec{T}).$$

The coefficients $f_{T,l}$ and $g_{T,l}$ need some explanation. The isospin representation chosen is not the $T_{total} = \frac{1}{2}$ or $\frac{3}{2}$ basis that was used in defining the Q_T. As the isospin dependence is projected out of equation (3.2) the terms are grouped into symmetric (isoscalar) and antisymmetric (isovector) combinations of the $T = \frac{1}{2}$ and $\frac{3}{2}$ amplitudes (see equation (3.5) at bottom of page). In the indices of the f's and g's a $T = 0$ signifies isoscalar and $T = 1$ denotes an isovector amplitude. Therefore, $f_{0,0}$ and $f_{0,1}$ are the isoscalar spin-nonflip amplitudes and $f_{1,0}$ and $f_{1,1}$ are the isovector spin-nonflip amplitudes. The $g_{T,l}$ are the isoscalar ($g_{0,1}$) and isovector ($g_{1,1}$) spin-flip amplitudes. There are no s-wave spin-flip terms since spin-flip terms are manifestations of the spin-orbit piece of the πN interaction and hence the s-wave cannot contribute. Finally the $f_{T,l}$ and $g_{T,l}$ can be expressed in terms of the $\alpha^{l}_{2T,2j}$ as follows:

$$
\begin{aligned}
f_{0,0} &= \frac{1}{3}[\alpha^{0}_{1,1} + 2\alpha^{0}_{3,1}]\cos\theta \\
f_{1,0} &= \frac{1}{3}[-\alpha^{0}_{1,1} + \alpha^{0}_{3,1}]\cos\theta \\
f_{0,1} &= \frac{1}{3}[\alpha^{1}_{1,1} + 2\alpha^{1}_{1,3} + 2\alpha^{1}_{3,1} + 4\alpha^{1}_{3,3}]\cos\theta \\
f_{1,1} &= \frac{1}{3}[-\alpha^{1}_{1,1} - 2\alpha^{1}_{1,3} + \alpha^{1}_{3,1} + 2\alpha^{1}_{3,3}]\cos\theta \\
g_{0,1} &= \frac{1}{3}[-(\alpha^{1}_{1,1} + 2\alpha^{1}_{3,1}) + (\alpha^{1}_{1,3} + 2\alpha^{1}_{3,3})]\sin\theta \\
g_{1,1} &= \frac{1}{3}[-(-\alpha^{1}_{1,1} + \alpha^{1}_{3,1}) + (-\alpha^{1}_{1,3} + \alpha^{1}_{3,3})]\sin\theta.
\end{aligned}
\tag{3.5}
$$

Equations (3.4) and (3.5) connect the free πN amplitude to the α's and hence the phase shifts that are experimentally determined. By using these expressions, the first order optical potential is calculated in the $t\rho$ approximation, from an expression similar to equation (3.1).

Scattering Theory

In this section the problem of πA scattering is examined in a more formal theoretical framework. First, it is useful to look at the distorted wave Born approximation. The multiple scattering series as derived by Watson [Wat 57] will then be discussed.

An understanding of scattering theory requires the introduction of several operators. The first operator of interest is the Green operator, G, which is related to the inverse of the Hamiltonian. There is also the free Green operator, $G_{\circ}$, which is related to the inverse of the free Hamiltonian, $H_{\circ}$. These operators have several familiar representations. The coordinate space representation is called the Green function and the momentum space representation is called the propagator. The formal equations defining G and $G_\circ$ are

$$G(z) \equiv (z - H)^{-1}$$

$$G_\circ(z) \equiv (z - H_\circ)^{-1}$$

where z is any complex number. The Lippmann-Schwinger equation that relates G and $G_\circ$ to the scattering potential, V, is

$$G = G_\circ + G_\circ V G. \tag{3.6}$$

The next operator of interest is the full T or transition operator which is defined by

$$T(z) = V + VG(z)V. \tag{3.7a}$$

Using equation (3.6) and equation (3.7a) it is easy to show that

$$G_\circ T = GV \tag{3.7b}$$

which is often used as the defining equation for T. The on-shell (on-shell implies that the kinematic condition $E^2 = k^2 + m^2$ is satisfied for the scattered particle) matrix elements of T are related to the scattering amplitude $F(\vec{k}', \vec{k})$ by

$$T_{fi} = \lim_{\epsilon \to 0} \langle \phi_f \Psi_{j_f m_f} | T(E + i\epsilon) | \Psi_{j_i m_i} \phi_i \rangle = \frac{-1}{(2\pi)^2 m} F(\vec{k}', \vec{k}). \tag{3.8}$$

Hence, the differential cross section, $\frac{d\sigma}{d\Omega}$, is proportional to the square of the on-shell T matrix, T_{fi}. Note that in the above matrix element the expectation value of the transition operator is taken between initial and final states of the system. These states must include both the relative motion of the projectile and the target nucleus and the nuclear wave functions, Ψ_{jm}.

In addition to these operators it is necessary to introduce appropriate wave functions for the system

$$\psi^{\pm} = \phi + G^{\pm} V \phi,$$

or as it is more frequently seen

$$\psi^{\pm} = \phi + G_{\circ}^{\pm} V \psi^{\pm}, \tag{3.9}$$

where $G^{\pm}$ and $G_{\circ}^{\pm}$ are the functions $G(z)$ and $G_{\circ}(z)$ evaluated at $z = E \pm i\epsilon$. The two signs represent two possible choices of boundary conditions at large r. The wave function ϕ is the free wave function of the system and the functions $\psi^{\pm}$ are eigenfunctions of the full Hamiltonian and asymptotically have the form of an incident wave plus a scattered wave.

The Born Series and DWBA

Now using equations (3.7a) and (3.7b) the following expression is obtained

$$T = V + V G_{\circ} T$$

which can be iterated to obtain the Born series for T

$$T = V + V G_{\circ} V + V G_{\circ} V G_{\circ} V + \ldots. \tag{3.10}$$

The physical interpretation of this series is that the scattering can be expressed as a sum of terms in which each successive action of the potential is followed by periods of free propagation. This series will converge rapidly if V is weak. In that case terms of high order in V can be neglected.

Consider a situation where the potential V can be split into two parts $V = U_{el} + U_x$. The potential, U_{el}, is one for which the wave equation can be solved easily, usually identified with an optical potential that describes elastic scattering, while U_x is the interaction that drives inelastic transitions. The Lippmann-Schwinger equation which accounts for the action of U_{el} is

$$\chi^{\pm} = \phi + G_{\circ}^{\pm} U_{el} \chi^{\pm} \tag{3.11}$$

(Compare to equation (3.9)). The functions $\chi^{\pm}$ are known as distorted waves and in this case are eigenfunctions of the Hamiltonian, $H_{el} = H_{\circ} + U_{el}$. An alternative expression for the on-shell T matrix is

$$T_{fi} = \langle \phi_f | V | \psi_i^{\pm} \rangle .$$

This expression and equation (3.11) lead, after some manipulation to

$$T_{fi} = \langle \chi_f^- | U_{\circ} | \phi_i \rangle + \langle \chi_f^- | U_x | \psi_i^+ \rangle ,$$

where $\psi^{\pm}$ are eigenfunctions of the full Hamiltonian. These can be expressed in terms of the distorted waves as

$$\psi^{\pm} = \chi^{\pm} + G_{el} U_x \psi^{\pm} , \tag{3.12}$$

where G_{el} is the Green function associated with $H_{el} = H_{\circ} + U_{el}$. Inserting equation (3.12) for $\psi_i^{\pm}$ into the expression for T_{fi} yields

$$T_{fi} = \langle \chi_f^- | U_{\circ} | \phi_i \rangle + \langle \chi_f^- | U_x | \chi_i^+ \rangle + \mathit{other\ terms}. \tag{3.13}$$

The approximation in which the higher order terms are neglected (i.e. $\psi^{\pm} \approx \chi^{\pm}$) is called the distorted wave Born approximation. This approximation is expected to be good if U_x is in some sense small. Perhaps a better statement is that the distorted wave Born approximation will be good if the elastic channel is the dominant channel.

Multiple Scattering and the Impulse Approximation

Now that the basic machinery of scattering theory has been developed it is necessary to extend the results to account for the scattering of a projectile by a nucleus. This process will be described by using the multiple scattering expansion [Wat 57] or Watson series. In this picture the interaction of a projectile with a nucleus is treated as a sum of interactions of the projectile with the individual nucleons. Only two-body interactions will be used and, as mentioned, it will be assumed that the potential V describing the πA interaction can be written as

$$V = \sum_{j=1}^{A} v_j$$

where v_j is the effective in-medium interaction between the incident pion and the j^{th} nucleon. The full transition operator can be written (See equations (3.7a) and (3.7b))

$$T = \sum_{j=1}^{A} v_j + \sum_{j=1}^{A} v_j G_\circ T. \tag{3.14}$$

It is important to observe that the propagator $G_\circ$ in this equation is very complicated in that it contains not only the kinetic energy operator of the projectile but the nuclear Hamiltonian as well.

Iterating equation (3.14) gives the Born series for T

$$T = \sum_{j=1}^{A} v_j + \sum_{j=1}^{A} v_j G_\circ \sum_{k=1}^{A} v_k + \cdots .$$

It is convenient to group all the terms that involve successive scatterings from the same nucleon together so that the entire scattering of the incoming pion with the k^{th} nucleon is accounted for by a single transition operator [Kol 80]. This operator will be designated τ_k and it satisfies the following Lippmann-Schwinger equation

$$\tau_k = v_k + v_k G_\circ \tau_k .$$

In terms of the τ_k the Born series for T becomes

$$T = \sum_{k} \tau_k + \sum_{j} \tau_j G_\circ \sum_{k \neq j} \tau_k + \cdots .$$

This is the Watson series or multiple scattering expansion. It is an infinite series of terms that describes the πA T operator in terms of single, double, triple, and higher order multiple scatterings of the pion with individual nucleons such that no two successive scatterings are from the same nucleon. The operator τ_i that describes the in-medium scattering of the pion and the i^{th} nucleon is unknown due to the presence of the nuclear Hamiltonian in the Lippmann-Schwinger equation for τ_i. For this reason it is common to replace this operator with the free πN t operator t^{free}. This approximation is called the impulse approximation. It is expected to be good if nuclear effects are small. This condition should hold when the projectile energy is much greater than the Fermi energy of the nucleons in the nucleus.

The last thing that must be done is to relate the multiple scattering T operator to the optical potential that is employed in the computer codes used in the analysis. After making the impulse approximation the equation for T is

$$T = \sum_{k} t_k^{free} + \sum_{j} t_j^{free} G_\circ \sum_{k \neq j} t_k^{free} + \cdots \tag{3.15}$$

This operator still contains explicit reference to the nuclear variables through $G_\circ$. An optical potential is a potential that satisfies a one-particle wave equation in the projectile's coordinates and correctly describes elastic scattering. A natural choice for the first order potential is, therefore, the ground state expectation value of (3.15). To first order this gives

$$U_1^{opt} = \langle 0 | \sum_{j} t_j^{free} | 0 \rangle . \tag{3.16}$$

If the implied integration over the nuclear degrees of freedom is carried out one is left with the desired result, a potential that is a function of only the projectile's coordinates. Taking the momentum space matrix elements of this optical potential yields

$$\begin{aligned} \langle \vec{k}', \vec{P}' | U^{opt} | \vec{k}, \vec{P} \rangle = \sum_{i=1}^{A} \int \frac{d\vec{p}_i'}{(2\pi)^3} \frac{d\vec{p}_i}{(2\pi)^3} \Phi_0^\dagger(\vec{p}_i') \Phi_0(\vec{p}_i) \\ \times \langle \vec{k}', \vec{p}_i' | t_i^{free}(\vec{k}', \vec{k}, \vec{p}_i, E) | \vec{k}, \vec{p}_i \rangle \end{aligned} \quad . \tag{3.17}$$

Here the $\Phi(\vec{p}_i)$ are the nuclear wavefunctions and the $\vec{p}_i$ are the momenta of the constituent nucleons. Note that the functional dependence of t is shown. Now assume that

$$\langle \vec{k}', \vec{p}_i' | t_i^{free} | \vec{k}, \vec{p}_i \rangle = (2\pi)^3 \delta(\vec{k}' + \vec{p}_i' - \vec{k} - \vec{p}_i) t_i(\vec{k}', \vec{k}, \vec{p}_i, E),$$

ie. the scattering is kinematically free, and further assume that the dependence of t on the nucleon momenta, $\vec{p}_i$, is negligible. Then equation (3.17) can be written

$$\langle \vec{k}', \vec{P}' | U^{opt} | \vec{k}, \vec{P} \rangle = A \langle \vec{k}' | t | k \rangle \rho(\vec{k} - \vec{k}'),$$

where

$$\begin{aligned} \rho(\vec{k} - \vec{k}') &= \frac{1}{A} \sum_{i=1}^{A} \int \frac{d\vec{p}_i}{(2\pi)^3} \Phi_0^{\dagger}(\vec{p}_i) \Phi_0(\vec{p}_i) \\ &= \int \exp\big(i(\vec{k} - \vec{k}') \cdot r\big) \rho(r) dr. \end{aligned}$$

If it is now assumed that the forward scattering dominates, one can extract a configuration space optical potential

$$U_{opt}(r) = t(\vec{q} = 0) A \rho(r).$$

$\vec{q}$ is the momentum transfer $\vec{q} = \vec{k} - \vec{k}'$. This result, $U_1^{opt} = t\rho(r)$, is formally identical to the result obtained in equation (3.1) (see also equation (3.8)). It was pointed out that this result is only approximate. Most of the approximations should be good for medium energy pion scattering. However this first order treatment ignores modifications of the pion propagation due to the presence of the nuclear medium. It is possible to expand the optical potential to higher orders in the density and get terms that are proportional to ρ^2, ρ^3, etc. This is often done in an attempt to account for the many-body effects present in πA scattering.

The Computer Codes

All the calculations of inelastic scattering were performed using the computer codes `DWPIES` [Sic 85], `MSUDWPIES`, and `ALLWRLD` [Car 81a][Car 81b]

. `DWPIES` and `MSUDWPIES` are both based on codes originally written by R.A. Eisenstein and G.A. Miller [Eis 74] [Eis 76]. These codes assume that the Klein-Gordon equation

$$(-\nabla^2 + m^2)\psi = E^2\psi \text{ which is just } E^2 - p^2 = m^2$$

is the correct wave equation for pions. The electromagnetic interaction is included by the addition of a potential $\phi(r)$ computed from a uniform spherical charge distribution. The πA potential is assumed to transform like the timelike piece of a four vector. This amounts to the replacement $E \rightarrow E - e\phi - V_{\pi A}$. The equation of motion that is actually solved uses the approximation $E^2 \approx (E - e\phi)^2 - 2EV_{\pi A}$. The codes solve the scattering problem by numerically integrating the equation of motion for each partial wave from the origin out to a match point. The radial wavefunctions are then compared to the asymptotic Coulomb wave functions and phase shifts are obtained.

The Specific Optical Potential

In the analysis that was done, the treatment of E. Siciliano and M. Johnson has been followed (see for instance[Joh 83a],[Joh 83b][Sic 86]). Their work is an extension of earlier work done by the group at Michigan State University, (MSU) [Str 79],[Str 80].

Siciliano assumes an optical potential with terms that are quadratic as well as linear in the nuclear densities. The higher order terms are split into two groups, those which are due to correlations, and those that are due to true absoption. First, the terms linear in the densities will be discussed. The first order potential is

$$\begin{aligned} U^1_{opt}(r) = &- k^2\left[\lambda^1_{s,0}\rho(r) + \lambda^1_{s,1}\left(\frac{\Delta\rho(r)}{2T_0}\right)(\vec{\phi}\cdot\vec{T})\right] \\ &\vec{\nabla}\cdot\left[\lambda^1_{p,0}\rho(r) + \lambda^1_{p,1}\left(\frac{\Delta\rho(r)}{2T_0}\right)(\vec{\phi}\cdot\vec{T})\right]\vec{\nabla} \\ &- \frac{1}{2}\nabla^2\left[(p_1-1)\left[\lambda^1_{p,0}\rho(r) + \lambda^1_{p,1}\left(\frac{\Delta\rho(r)}{2T_0}\right)(\vec{\phi}\cdot\vec{T})\right]\right]. \end{aligned} \tag{3.18}$$

In the above equation $\rho(r)$ and $\Delta\rho(r)$ are the nucleon and excess neutron densities respectively. As before, $\vec{\phi}$ is the isospin operator for the pion while $\vec{T}$ is the isospin operator for the nucleus. The λ^1's are coupling constants that are related to the free πN amplitudes (See equation (3.5)) by kinematic factors. The λ^1's do not contain the angular functions $P_l(\cos\theta)$ or $P_l'(\cos\theta)$. For example $\lambda^1_{p,0} = f_{0,1}\left(\frac{4\pi}{p_1\kappa^3\cos\theta}\right)$. The other λ^1's have similar relationships with the f's.

In the above expression k is the pion's wave number in the πA center of momentum frame and κ is the pion's wave number in the πN center of momentum frame. The factor p_1 in the last term of equation (3.18) arises from the transformation between the πN and πA systems. In fact, the entire Laplacian term has its origin in this transformation [Kis 74]. This transformation is necessary because the πN amplitudes are known in the πN center of momentum system, while πA scattering is most conveniently calculated in the πA center of momentum system. The gradient operators in $\vec{\nabla}\cdot[\cdots]\vec{\nabla}$ reflect an assumed $k\cdot k'$ dependence of the p-wave piece of the amplitude [Kis 55]. This form ($k\cdot k'$) was chosen as it is perhaps the simplest non-local (momentum dependent) potential. Finally, the factor $2T_0$ is just a convienient notation for $(N-Z)$. The potential presented above is just

$t\rho$ with the angle or frame transformation included. This potential by itself does not provide an adequate description of πA scattering as there are many important medium effects that it does not take into account.

Medium Modifications

The first order potential shown is augmented by terms that are quadratic in the nuclear densities. These terms reflect processes involving more than one nucleon such as true absorption and various correlation effects. Before discussing these terms, there is one correction to the potential due to the nuclear medium that enters in first order. This effect is called Pauli blocking and the formulation of its contribution in the πA optical potential used is due to Landau andMc Millan [Lan 73]. Pauli blocking refers to the fact that when a pion interacts with a nucleon in a nucleus it can not scatter that nucleon into an occupied state. In the Landau McMillan formulation, the effect is calculated by considering pion scattering in nuclear matter. The net result of this prescription is that the imaginary terms in the optical potential are multiplied by a blocking factor which depends on the ratio of the Fermi momentum to the pion's momentum. This factor is 0.392 for pions with a kinetic energy of 65 MeV. The Fermi wave number, k_f, was taken to be 1.4fm^{-1} for this purpose.

The medium modifications take a form that is completely analogous to the first order potential. That form is (excluding isotensor terms)

$$\begin{aligned} U^2_{opt} = & -k^2[\lambda^2_{s,0}(\frac{\rho^2(r)}{\rho_0})+\lambda^2_{s,1}(\frac{\rho(r)}{\rho_0})(\frac{\Delta\rho(r)}{2T_0})(\vec{\phi}\cdot\vec{T}) + S(r)] \\ & +\vec{\nabla}\cdot[\lambda^2_{p,0}(\frac{\rho^2(r)}{\rho_0})+\lambda^2_{p,1}(\frac{\rho(r)}{\rho_0})(\frac{\Delta\rho(r)}{2T_0})(\vec{\phi}\cdot\vec{T}) + L(r)]\vec{\nabla} \\ & -\frac{1}{2}\nabla^2[(p_2-1)[\lambda^2_{p,0}(\frac{\rho^2(r)}{\rho_0})+\lambda^2_{p,1}(\frac{\rho(r)}{\rho_0})(\frac{\Delta\rho(r)}{2T_0})(\vec{\phi}\cdot\vec{T})]] \end{aligned} \tag{3.19}$$

Here S(r) and L(r) are due to correlations while the terms with the λ^2's are due to πNN absorption. The factor p_2 in the last term is another kinematic factor assocaited with the frame transformation (see the discussion of the first order potential).

Siciliano et al. [Sic 86] assume that the s-wave correlation term, $S(r)$, is due only to Pauli correlations (these are short range correlations that result from the Pauli exclusion principle). The explicit isospin and density dependence of this term are expressed in the following equations

$$\begin{aligned} S &= S_0 + S_1(\phi \cdot T) \\ S_0 &= -\frac{3k^2}{8\pi^2 p_1} k_f[(\lambda^1_{s,0})^2 + \frac{1}{2}(\lambda^1_{s,1})^2]\rho(r) \\ S_1 &= -\frac{3k^2}{8\pi^2 p_1} k_f[2\lambda^1_{s,0}\lambda^1_{s,1} - \frac{1}{2}(\lambda^1_{s,1})^2]\rho(r). \end{aligned} \tag{3.20}$$

Two things are important. First, in this treatment the effect is described by terms that are linear in the nuclear density, $\rho(r)$. Second, the magnitude of the effect is completely determined by the first order coupling constants (the λ^1's) and the value of k_f (here taken to be 1.4 fm^{-1} as above).

The term $L(r)$ describes p-wave correlation effects. It is intended to account for several different phenomema. They are p-wave Pauli correlations, the Lorentz-Lorenz Ericson-Ericson effect (LLEE), and some contributions due to exchange of ρ mesons [Bay 75]. L can be expanded, in a manner similar to that employed in the s-wave piece, as

$$L = L_0 + L_1(\phi \cdot T) \tag{3.21a}$$

where

$$\begin{aligned} L_0 &= -\frac{\alpha}{3} X(\lambda^1_{p,0})^2(\rho(r))^2 \\ L_1 &= -\frac{2\alpha}{3} X^2[1 + \frac{\alpha}{6}\lambda^1_{p,0}\rho(r)]\frac{\rho(r)\Delta\rho(r)}{2T_0} \end{aligned} \tag{3.21b}$$

and

$$X = [1 + \frac{\alpha}{3}\lambda^1_{p,1}\rho(r)]. \qquad (3.21c)$$

The important thing to note is that the magnitude of the p-wave correlation is determined by the correlation strength α and the first order λ's. The dimensionless parameter α was taken to be 1.6 [Sic 86] in all the calculations shown in this work.

The numerical strengths of the absorption terms were taken from the work of Alons et al.[Alo 86]. They treat the second order strengths (the λ^2's) as parameters, and obtained values for them by fitting experimental data. The data set that they fit included data from experiments performed at pion energies ranging from 0 MeV (pionic atom data) to 80 MeV. The higher energy data included both elastic scattering, single charge exchange to the isobaric analog state and double charge exchange to the double isobaric analog state. Like the first order potential, the second order potential (eq (3.19))is broken into s and p-wave channels and each of these channels is then further decomposed into isoscalar, isovector and isotensor pieces. The isotensor piece provides a direct mechanism for double charge exchange and therefore has been and will be neglected throughout this work. That means that there are in principle four complex strength parameters to be fit in a phenomenological treatment. These parameters are the second order s-wave isoscalar and isovector strengths, $\lambda^2_{s,0}$, and $\lambda^2_{s,1}$ and the corresponding p-wave strengths, $\lambda^2_{p,0}$ and $\lambda^2_{p,1}$. Using the first order potential and correlation terms previously described the isoscalar second order parameters were fit [Alo 86] to elastic scattering from N=Z (T=0) nuclei. These terms were then held fixed during the fitting of the isovector terms to single charge exchange data. In the present set of parameters only two of the possible four isovector parameters were determined. They were $Re\lambda^2_{s,1}$ and $Im\lambda^2_{p,1}$. The others were taken to be zero.

Matter Densities and Form Factors

The ground state matter densities appear in the optical potential which is used for calculating elastic scattering cross sections as well as for generating the distorted waves used in inelastic calculations. One needs some sort of method for obtaining these densities. Two ground state densities were used in this work. They were the three parameter Fermi distribution used in the analysis of [See 81] and a density that was derived from Hartree-Fock calculations using a Skyrme-III nucleon-nucleon force.

The calculation of inelastic transitions require additional nuclear structure input, which again enters through the DWBA. By using the Watson series the optical potential U_{el} was identified with the ground state average of the free πN t matrix. Similarly the inelastic potential U_x can, to first order, be identified as

$$U_x = \langle f| \sum_j t_j^{free} |0\rangle \tag{3.22}$$

where $|f\rangle$ is the final state nuclear wave function. Using arguments similar to those employed for the elastic optical potential this can be written $U_x = t\rho_{tr}(r)$ where $\rho_{tr}(r)$ is the transition density in coordinate space. The Fourier transform of ρ_{tr} is called the form factor. The models for calculating ρ_{tr} will be discussed in the next chapter. It should be noted that the current version of `DWPIES` allows only first order terms in U_x. Therefore, the medium effects are only included in the distorted waves for inelastic calculations.

All the calculations shown in the next chapter for the data at $T_\pi =$ 65 MeV were performed using the first order potential discussed above with coupling strengths determined from Arndt's FP85 phase shift solution [Arn 85] and the second order parameters of Alons et al. This is by no means a unique prescription but it is a consistent one.

CHAPTER IV

COMPARISON OF THEORY TO DATA

In this chapter, the experimental angular distributions will be compared with the theoretical calculations described in the previous chapter. This will be done for each state that was analyzed. In addition, the results will be compared with the results of similar experiments that have been performed at different energies.

Elastic Scattering

A large fraction of the pions that scatter from the nucleus leave the nucleus in its ground state. These events are called elastic events. It is important to have a reasonable description of elastic scattering as this process also enters the inelastic calculations through the distorted waves, $\chi^{\pm}$. Elastic scattering is sensitive to the ground state matter distributions ρ_n and ρ_p. This point was discussed briefly in the previous chapter. At resonance energies the scattering is highly diffractive. This means that the elastic peak has an angular distribution that is proportional to $\frac{J_1(kR\theta)^2}{(kR\theta)^2}$ (this is an approximation, but it does give the correct qualitative behavior). This implies that the positions of the minima in the angular distribution at a fixed incident energy are only dependent upon some characteristic radius of the matter distribution. One reasonable measure of this characteristic radius is the rms charge radius as found by electron scattering. Because electrons interact electromagnetically, electron scattering is mostly sensitive to the distribution of the protons. The rms radius for the neutrons is usually taken to be equal to the proton radius or is extracted in some model-dependent fashion from π^- elastic scattering or from high energy proton scattering. Before discussing the actual matter distributions used in the distorted wave calculations it is important to note that there are two types of matter distributions reported in the literature. These are the nucleon charge or matter distributions and the distributions of point nucleons. These differ in that the point distributions have the form factors of the individual nucleons unfolded. The effect of this unfolding on the radii of the charge distributions is shown in the equation below

$$\langle r^2_{point} \rangle = \langle r^2_{charge} \rangle - \langle r^2_{proton} \rangle.$$

In this equation $\langle r^2_{charge} \rangle$ is the square of the rms radius of the nuclear charge distribution (the 'actual' charge distribution) as measured by electron scattering and $\langle r^2_{proton} \rangle$ is the square of the rms radius of the proton as measured in electron scattering [Bil 71]. One could, of course, define analogous quantities for neutrons. The matter distributions that go into the impulse approximation optical potential should be the point distributions because the effects of the nucleon form factor are included, to some extent, in the free πN t matrix, t^{free}. The three-parameter Fermi distribution used in the present analysis was originally determined by Blanpied et al. by fitting data for the scattering of 800 Mev protons [Bla 78] by ^{13}C. During their analysis Blanpied et al. kept the radius of the point proton distribution fixed to the value unfolded from electron scattering results [Hei 70][Bil 71]. They then varied the neutron parameters to obtain a best fit to elastic scattering data. Seestrom-Morris [See 81] started with all of Blanpied's parameters but found that there was little need for different neutron and proton distributions. Therefore, she first used Blanpied's proton parameters to describe both the neutron and proton densities. She then found that to fit the positions of the diffractive minima at $T_\pi = 162$ MeV it was necessary to adjust these parameters. The net effect of these adjustments was to decrease the rms radius of the point distribution (neutrons and protons both have the same distribution) to $r_{rms} = 2.28$ fm [See 81]. This is slightly below the value $r_{point} = 2.29$ fm obtained by unfolding the proton radii from electron scattering results [Hei 70][Bil 71]. The three-parameter Fermi distribution has the form

$$\rho_{ground} = (1 + w\frac{r^2}{R^2})(1 + \exp((r - R)/z))^{-1}.$$

The values used for the three parameters in this work are those used by Seestrom-Morris, $R = 2.40$ fm, $z = 0.41$ fm, and $w = -0.16$.

The other ground state distributions used were theoretical as opposed to phenomenological. More accurately, they have the phenomenology buried at a deeper level in the form of parameters in a $N - N$ interaction. The form of the interaction used is due to Skyrme [Sky 59] and the particular set of values for the parameters is set *III* from the work of Beiner et al. [Bei 74]. This form of the $N-N$ interaction is used as input for self consistent calculations. In this manner, ground state distributions for both neutrons and protons are obtained. The root mean square radius of the proton distribution used was $r_{rms} = 2.467$ fm (this was determined by a numerical integration), which is larger than the point rms radius unfolded from electron scattering data. The neutron distribution is different from the proton distribution in this model and the neutron density used has a rms radius of $r_{rms} = 2.395$ fm. This is close to the value of $r_{rms} = 2.35 \pm 0.03$ fm for neutrons obtained by Johnson [Joh 79] from analysis of low energy π^- elastic scattering data but does not agree well with the value of 2.54 ± 0.01 obtained by Blanpied et al. It is hard to say what the correct value is because this is a very model dependent number. Figure 4.1 shows both the three-parameter Fermi and the Skyrme-*III* matter distributions. These distributions are normalized so that their volume integrals are 1.

Figures 4.2 and 4.3 show the present elastic scattering data as well as the data of Blecher et al. [Ble 83]. In addition, three calculated curves appear on the figures. Two of the curves use identical reaction mechanism but different matter densities (solid and dot-dashed). The final curve (dashed) was calculated without any second order terms in the optical potential. These curves show that there is some sensitivity to the choice of matter distributions, particularly at large angles. It should be noted that the position of the minimum is not very sensitive to the rms radius. This is because the observed minimum is not diffractive in nature but is due to destructive interference of the s and p-wave amplitudes. The curves calculated with the Skyrme densities seem to do a better overall job. I do not place a lot of significance in this because the effect could be due to the fact that Alons et al. [Alo 86] used these Skyrme distributions when they fit their parameters. The third curve in the figure shows the dramatic effect of the second order terms in the optical potential, which were set to zero for the dashed curve. The

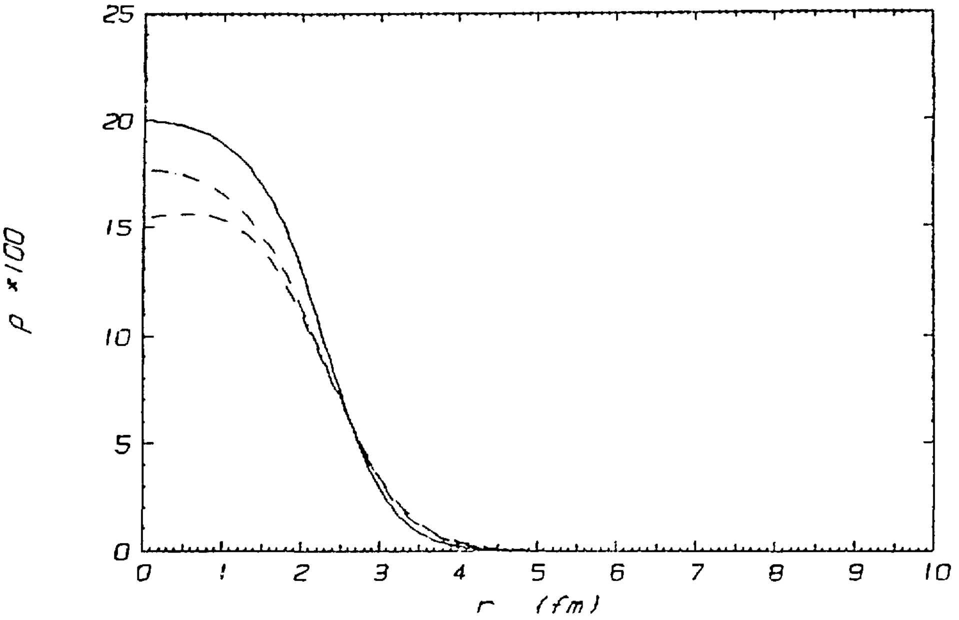

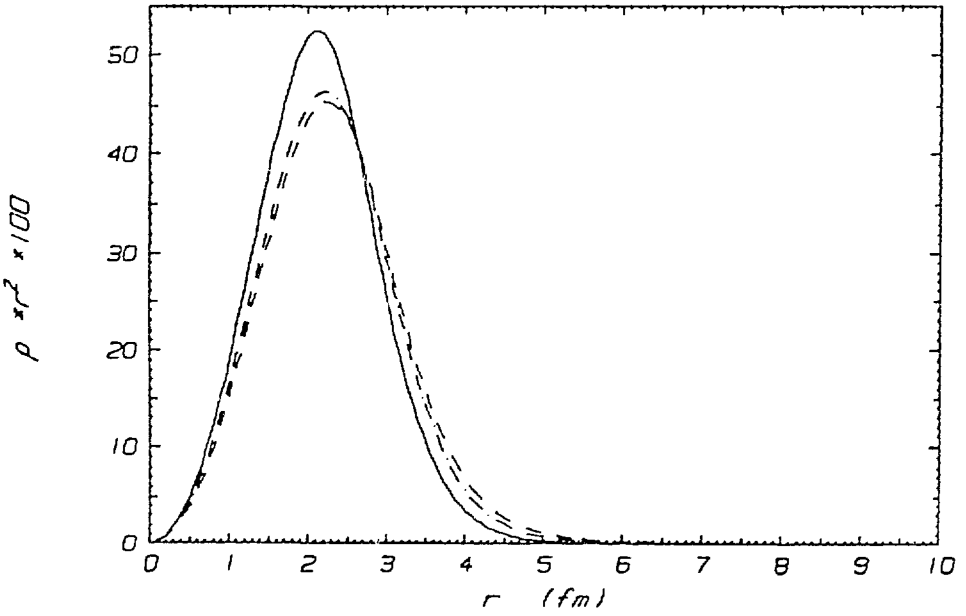

Figure 4.1 The ground state matter distributions used in the calculations. The solid line is the 3-parameter Fermi distribution. The dot-dashed line is the Skyrme neutron density while the dashed line is the Skyrme proton density.

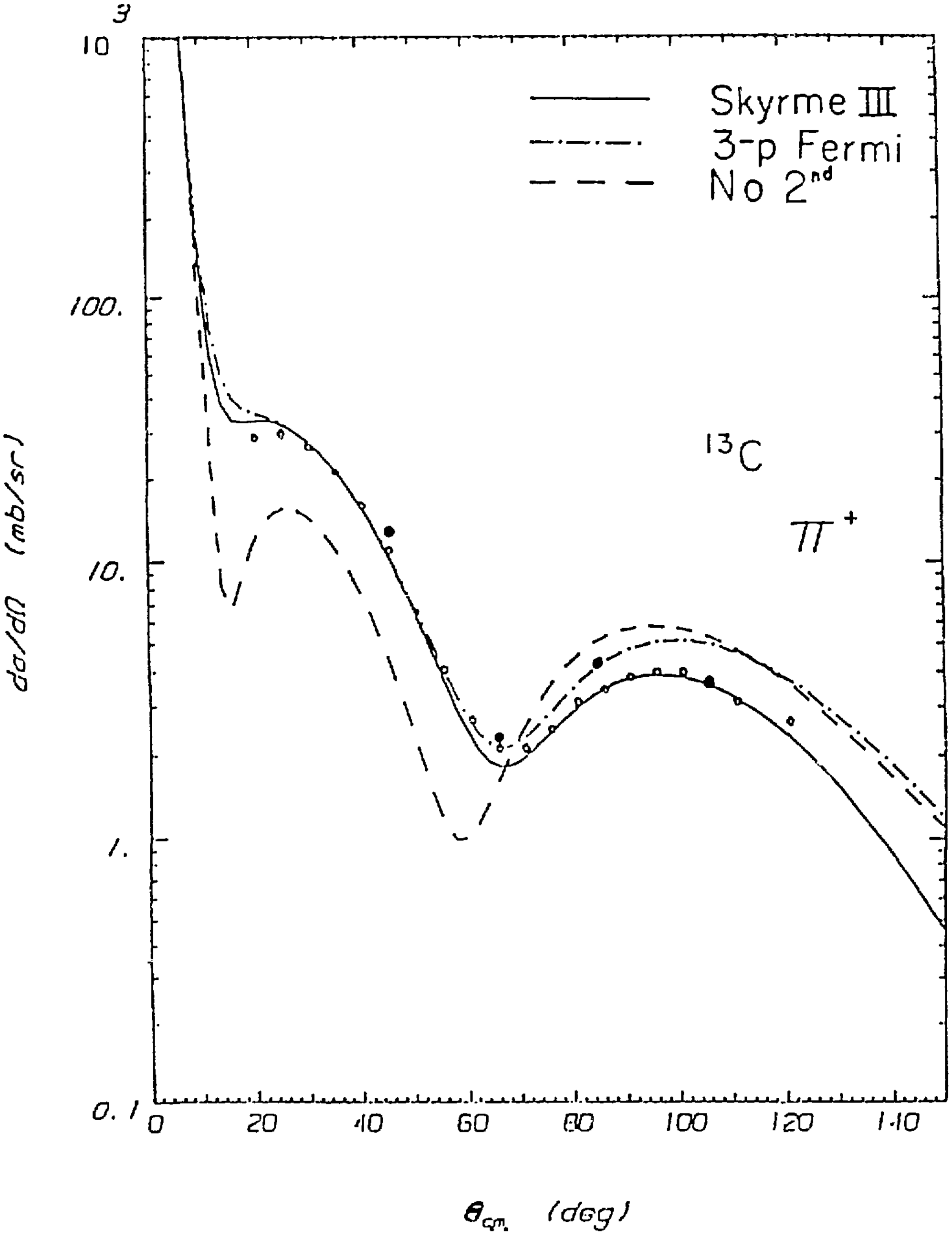

Figure 4.2 Data for π^+ elastic scattering at T_π = 65 MeV (solid circles). Also shown are the data of Blecher et al (open circles). The curves are distorted wave calculations using two different ground state matter distributions and also one which shows the effects of turning off the second order parameters.

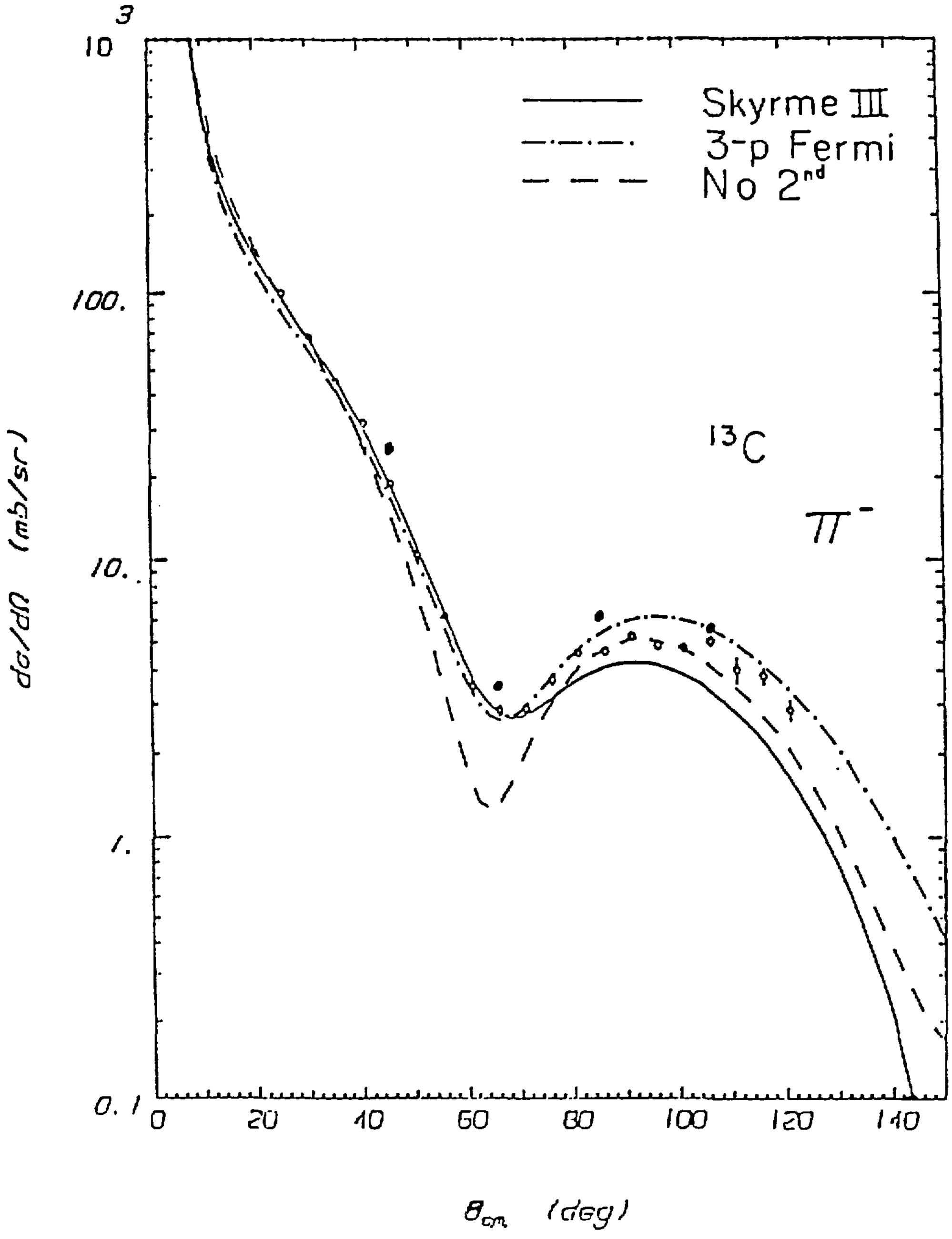

Figure 4.3 Data for π^- elastic scattering at T_π = 65 MeV (solid circles). Also shown are the data of Blecher et al (open circles). The curves are distorted wave calculations using two different ground state matter distributions and also one which shows the effects of turning off the second order parameters.

effect of these terms is particularly apparent in the π^+ calculations where there is strong destructive interference between the Coulomb and nuclear interactions.

Although the point which corresponds to a lab angle of 84° is a little high, the present data for the scattering of positive pions are in good agreement with the earlier data of Blecher. This is to be expected as the absolute π^+ normalization of the present data was taken from Blecher's ^{12}C measurements that were performed in conjunction with his ^{13}C measurements. The present π^- data are consistently 15 to 20% high relative to the older data. This reflects the normalization to the deuterium measurements of Balestri et al. [Bal 83]. This point was discussed in Chapter 2.

The Collective Model

The majority of the states that were seen in this experiment are believed to be collective in nature. These collective states are bulk excitations of the nucleus as a whole. Examples of this type of transition are states that are analogous to surface vibrations of a liquid drop or states which are rotations of a deformed nucleus about a fixed axis. In this model [Boh 75] the ground state is taken to be non-spherical. This leads to a non-spherical potential which can be written

$$U(r) = U_\circ(r) + \delta U(r). \tag{4.0}$$

$U_\circ$ is identified with U_{el}, the optical potential for describing elastic scattering, and $\delta U(r)$ can be interpreted as the potential U_x that drives the inelastic transitions. Consider, for example, a two parameter Fermi distribution

$$U(r, R) = U(1 + \exp((r - R)/z))^{-1}.$$

This can be deformed by giving the radius parameter an angular dependence

$$R(\hat{\vartheta},\phi) = R_\circ + \sum_{lm} \delta_{lm} Y^l_m(\theta,\phi). \tag{4.1}$$

If this expression for R is used and a Taylor series expansion of $U(r,R)$ about $R = R_\circ$ is made one obtains the following expression

$$U(r,R) = U(r,R_\circ) + \left.\frac{\partial U}{\partial R}\right|_{R=R_\circ} \sum_{lm} \delta_{lm} Y^l_m(\theta,\phi) + \cdots. \tag{4.2}$$

The second term can be identified as δU to first order in the deformation lengths, δ_{lm} [Sat 80]. For a potential that is only a function of the quantity $(r - R)$ the partial derivative with respect to R in equation (4.2) can be replaced by minus the partial with respect to r and therefore in this model the interaction is surface peaked. It should also be noted that all multipolarities have the same radial dependence, that of $\partial\rho_{ground}/\partial r$, for their transition densities or equivalently for their inelastic potentials.

In all the figures where our data for scattering to a collective state are compared to calculations, three calculations are shown. These are labeled Skyrme-*III*, 3-parameter Fermi and no 2^{nd} order. The calculations for the Skyrme-*III* curve use the ground state Skyrme densities for generating the distorted waves and use surface peaked derivatives of the Skyrme densities for the transition densities. These transition densities were generated numerically using a simple three point derivative algorithm as discussed by Koonin [Koo 86]. In all cases, the transition density is just the derivative of the ground state density distribution. The calculations with no second order parameters also use the Skyrme densities. The three-parameter Fermi calculation used the Fermi distribution described earlier.

It is customary to report values of the deformation lenghts, δ_{jm}, and indeed these have been extracted. Operationally these are extracted by adjusting the normalization of the theoretical calculations relative to the data as $(\delta_{jm})^2 = \frac{d\sigma/d\Omega}{d\sigma/d\Omega_{DWBA}}$. The values of δ are summarized at the end of the discussion on collective states. Here it should be noted that all the curves in each figure are normalized to the same value of δ and that this value of delta was obtained from the Skyrme-*III* calculation.

The States at 3.68 MeV and 7.55 MeV in Excitation

These states are thought to be formed by coupling the $p_{\frac{1}{2}}$ neutron in the ground state of ^{13}C to the 2^+ state at 4.44 MeV in ^{12}C. Hence the calculations assume that both of these states undergo $\Delta J = 2$ transitions from the ground state even though the selection rules allow other possible modes. The only real differences in the calculations for these two states arise from the distortions of the outgoing pion due to the difference in the excitation energies.

The state at 3.68 MeV is characterized by $J^\pi = \frac{3}{2}^-$. Figure 4.4 shows the data for excitation of this state in π^+ scattering. It is apparent that the effect of the second order parameters, although not as dramatic as in the case of elastic scattering, is still sizeable. The best description of the data seems to be provided by the Skyrme curve. This is true independent of the normalization of the curves.

The π^- cross sections for this state are shown in figure 4.5. The angular distribution of the data points is significantly different from that of the π^+ data to the same state. One expects only minor differences in the angular behavior due to such things as Coulomb-nuclear interference, but this should only affect the most forward angles ($\theta < 20$ degrees). Effects might also be due to differences in the distribution of neutrons and protons. If one lines up the back angle (the points at $\theta_{lab} = 84°$ and $105°$) data in the two angular distributions (π^+ and π^-) and then compares the relative magnitudes of the two forward angle points one finds that the π^- data are higher than those in π^+ by a factor of approximately 1.5.

It was thought that perhaps this was due to the fact that the peak from which the cross sections were extracted is actually an unresolved doublet. In addition to the 3.68 MeV state, this peak contains events associated with a state at 3.85 MeV. The state at 3.85 MeV ($J^\pi = fiveh^+$) is believed to be a non-collective $\Delta J = 3$ transition and was found to be neutron-like at resonance [See 81]. One would expect that if this unresolved peak were the reason that the π^- angular distribution is shaped differently than the π^+ angular distribution that the discrepancy would appear at the back angle points. This does not seem to be the case. The presence of the 3.85 MeV state does not seem to provide an adequate description for the observed difference at forward angles.

The state at 7.55 MeV has spin and parity $J^\pi = \frac{5}{2}^-$. The angular distributions are shown in figures 4.6 and 4.7. Again the angular distributions for π^+ and π^- differ in the same way but to a lesser degree than in the data for the other $L = 2$ transition. This effect is not described by the calculations and is not understood. Since the calculations are sensitive to the specific choice of matter distributions it could be that the differences between the neutron and proton densities used is not of the correct amount. It would also be useful to examine the effect of the inclusion of second order parameters

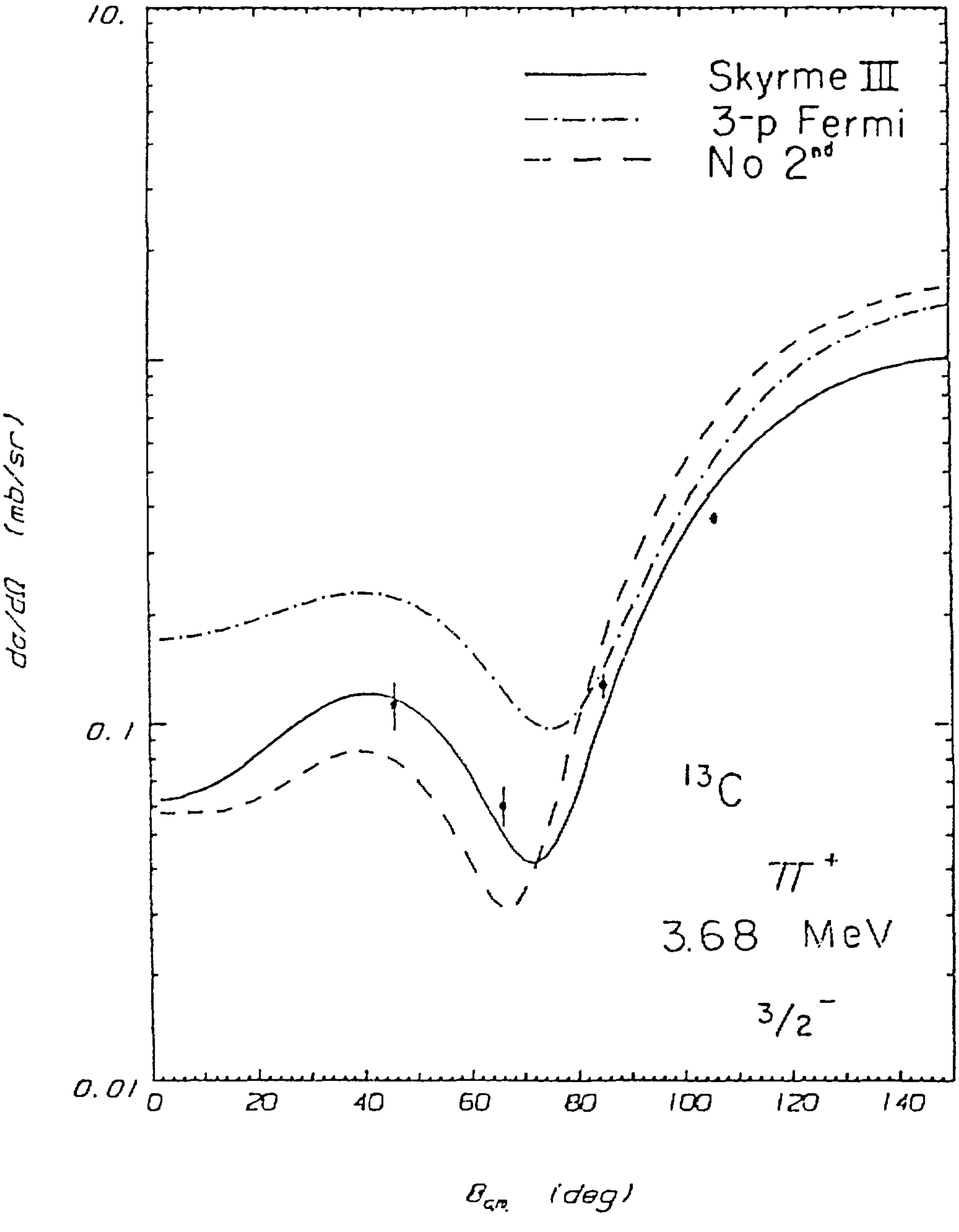

Figure 4.4 The data for scattering π^+ to the $j = \frac{3}{2}$ state at 3.68 MeV. The curves are the distorted wave calculations discussed in the text.

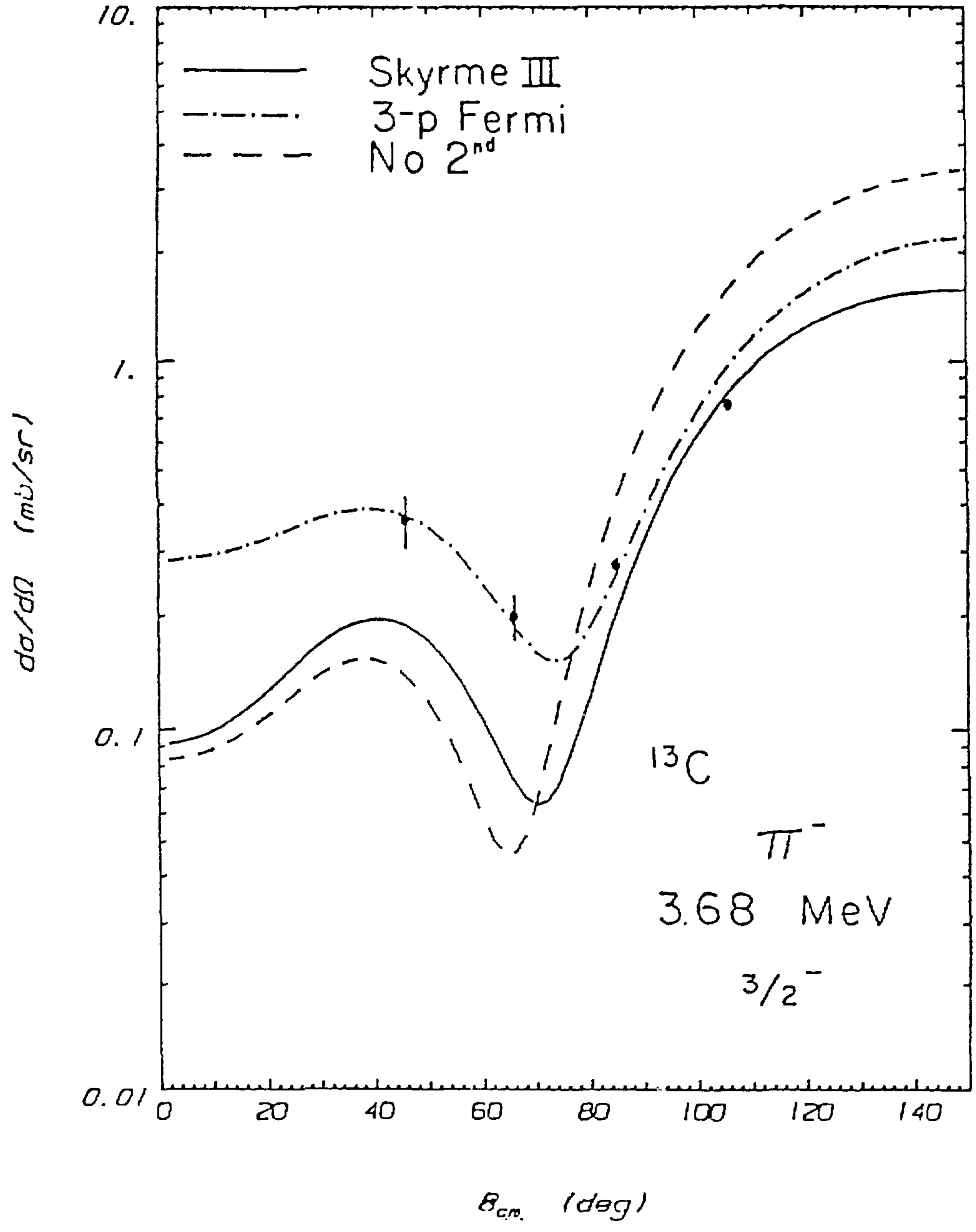

Figure 4.5 The data for scattering π^- to the $j = \frac{3}{2}$ state at 3.68 MeV. The curves are the distorted wave calculations discussed in the text.

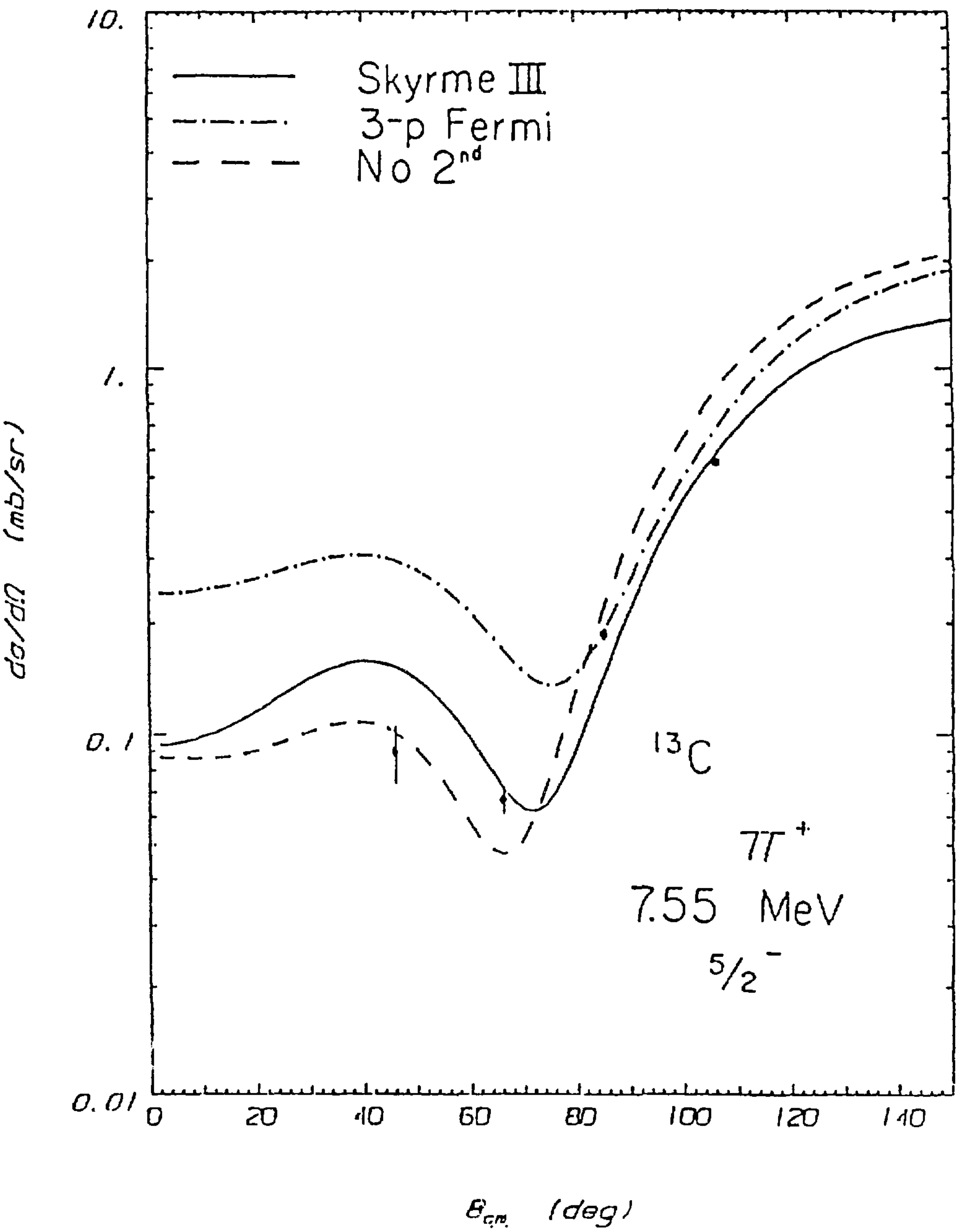

Figure 4.6 The data and distorted wave calculations for the scattering of 65 MeV π^+ to the state at 7.55 MeV in excitation.

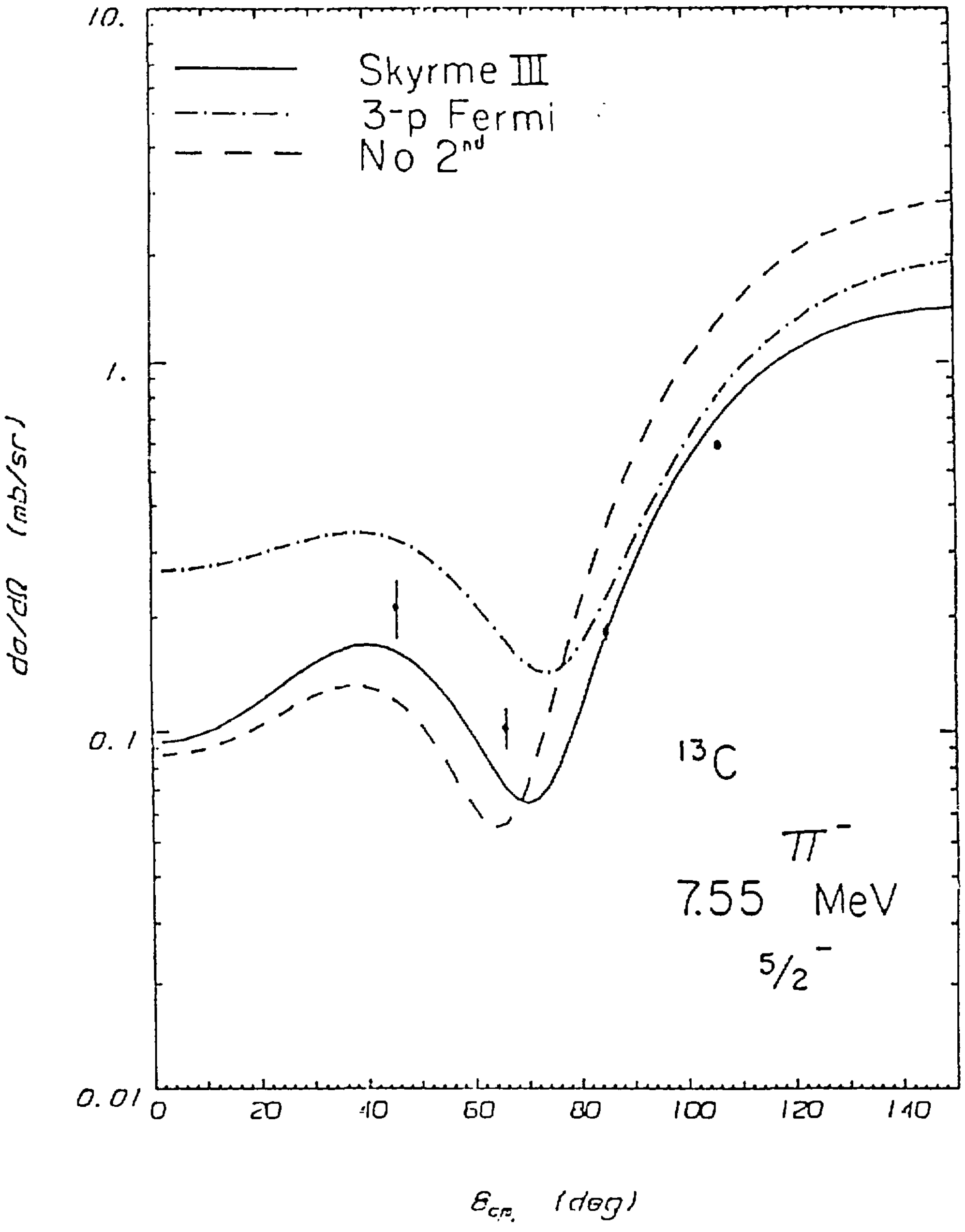

Figure 4.7 The data and distorted wave calculations for the scattering of 65 MeV π^- to the state at 7.55 MeV in excitation.

in the transition term. Of course more complete angular distributions would also be helpful.

The State at 11.82 MeV

This state is believed to be a $\frac{5}{2}^{+}$ state that undergoes an octupole $\Delta L = 3$ transition from the ground state. The calculations all assume that this is a $\Delta L = 3$ transition. Unlike the two $\Delta L = 2$ transitions, here the π^{+} and π^{-} distributions seem to have the same shape and that shape is reasonably well accounted for by the calculations which include the second order terms. The elimination of the second order terms has a fairly large effect on the predicted distributions for both π^{+} and π^{-}. The data and calculations for this transition are shown in figures 4.8 and 4.9.

The Monopole Transition at 8.86 MeV in Excitation

In the collective model one can picture monopole excitations as spherical breathing modes of the nucleus. To do this requires some special considerations. Nuclear matter appears to have very limited compressibility. Therefore, it is important to impose the constraint of volume conservation. If the density is expanded (this is the same as expanding the potential) in the form

$$\rho(r) = \rho_{\circ}(r) + \delta\rho(r).$$

The constraint of volume conservation can be expressed as [Sat 73]

$$\int \delta\rho \; r^{2} dr d\Omega = 0.$$

Imposing this condition leads to a transition density $\delta\rho$ of the following form

$$\delta\rho = \rho_{tr} = 3\rho_{ground} + r\frac{d\rho_{ground}}{dr}.$$

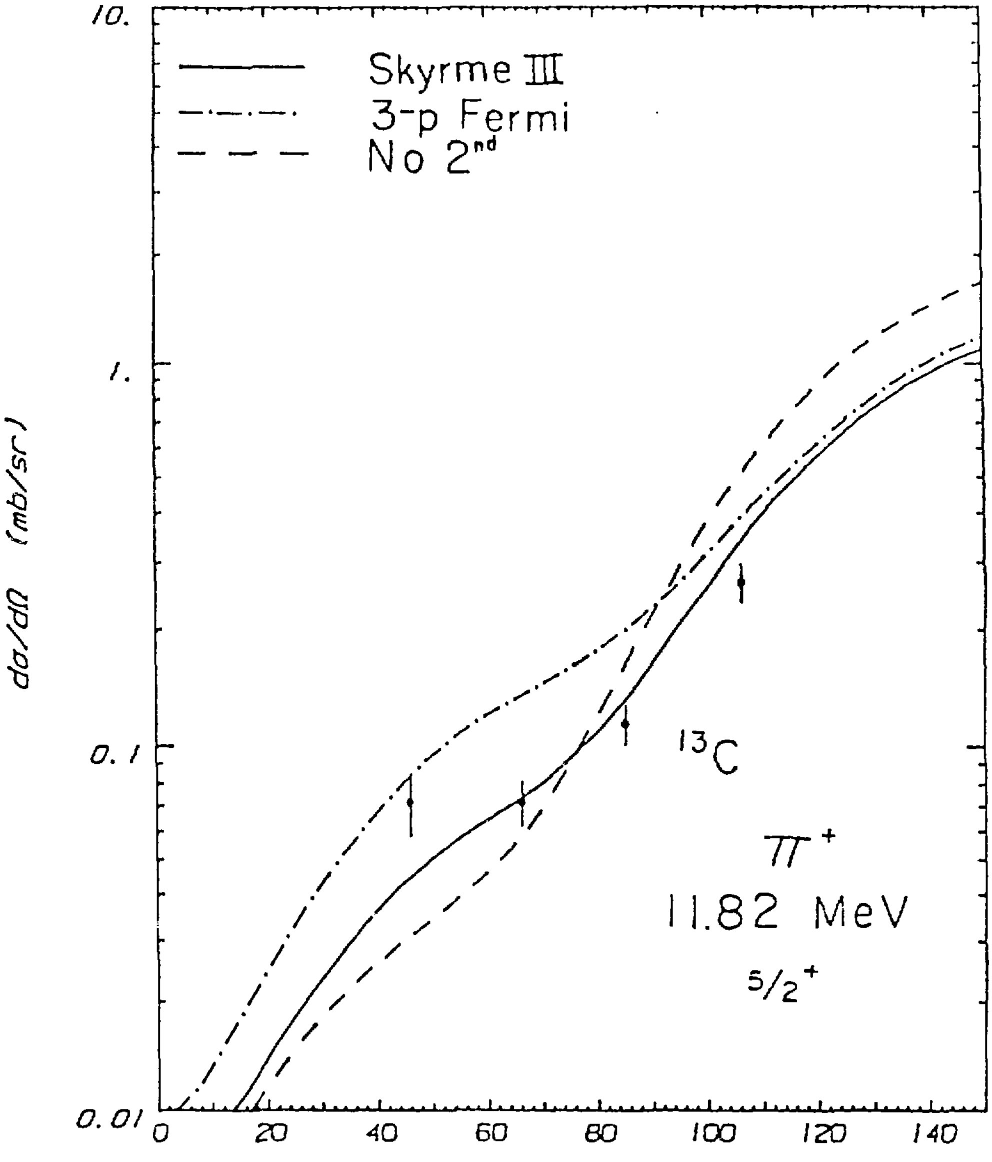

Figure 4.8 The measured angular distributions for the scattering of positively charged pions to the state at 11.82 MeV in excitation. The beam energy was 65 MeV. The curves assume that this is a $L = 3$ transition.

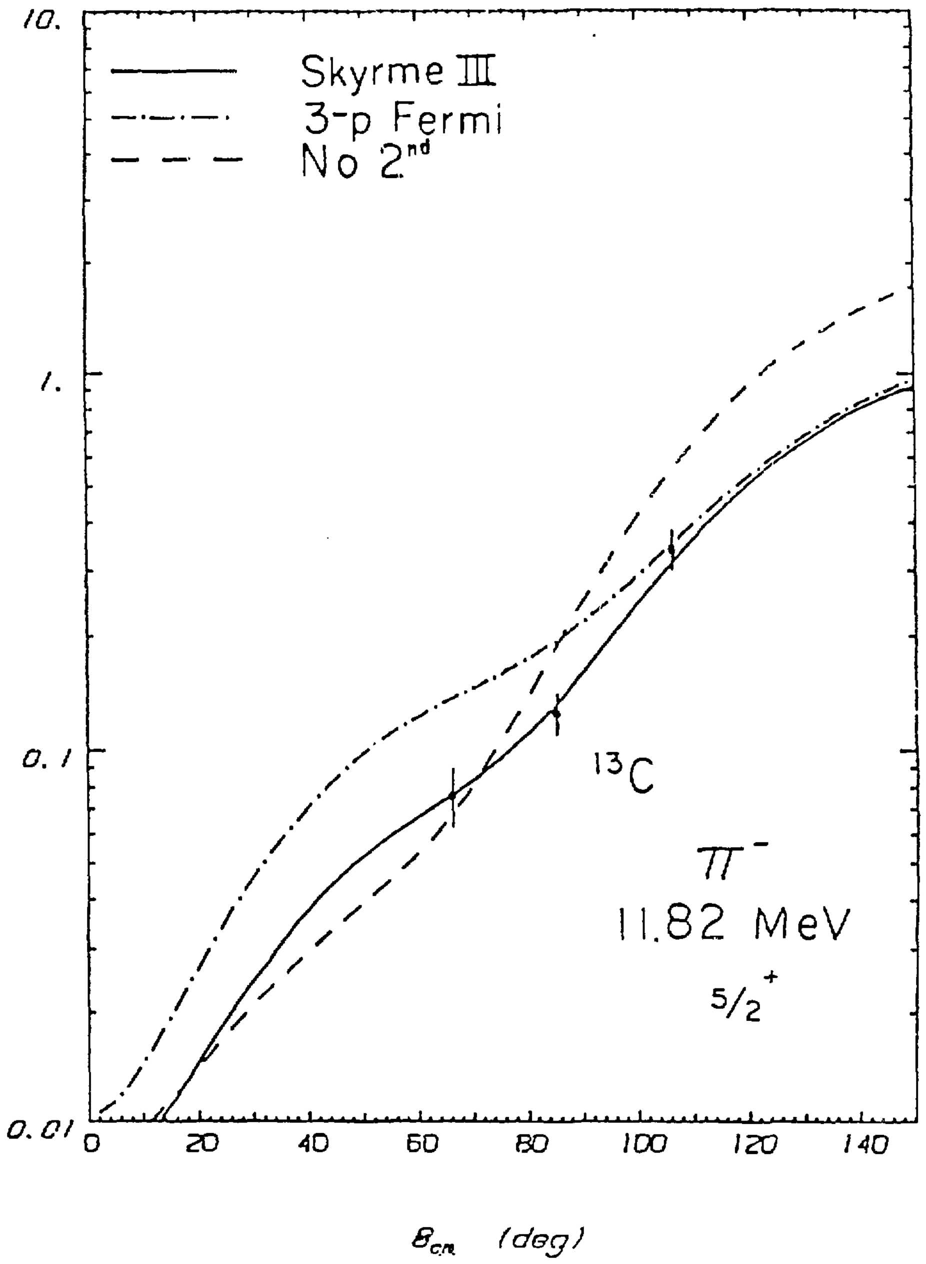

Figure 4.9 The measured angular distributions for the scattering of negatively charged pions to the state at 11.82 MeV in excitation. The beam energy was 65 MeV. The curves assume that this is a $L = 3$ transition.

This form of the transition density was used in the calculations of the angular distributions for the $\frac{1}{2}^-$ state at 8.86 MeV. Figure 4.10 shows the monopole transition densities as well as the surface peaked densities that were used for the calculations of the states of higher multipolarity. The most apparent feature of the $\Delta L = 0$ densities is the presence of a node near the nuclear surface.

Figures 4.11 and 4.12 show the results for π^+ and π^- scattering to this state. The π^+ and π^- data have almost identical angular shapes and are well described by the calculation that utilizes the Skyrme densities. The position and depth of the minimum are quite sensitive to the details of the calculation.

Summary of the Results for the Collective Excitations

The results will be summarized by comparing the extracted deformation parameters with those obtained from higher energy pion scattering as well as those from experiments involving other probes. There are many prescriptions for extracting the deformation length, $\delta_{jm} = \beta R$ in pion scattering experiments. Often the βR's for the neutron and proton distributions are varied separately to fit the π^- and π^+ angular distributions simultaneously. In this work separate βR's were extracted from the π^+ and π^- data. In the hydrodynamic model the βR_+ and βR_- that were obtained in this work can be related to the neutron and proton deformations, βR_n and βR_p [Ull 86a]. In this sense the two sets of deformation lengths contain the same information.

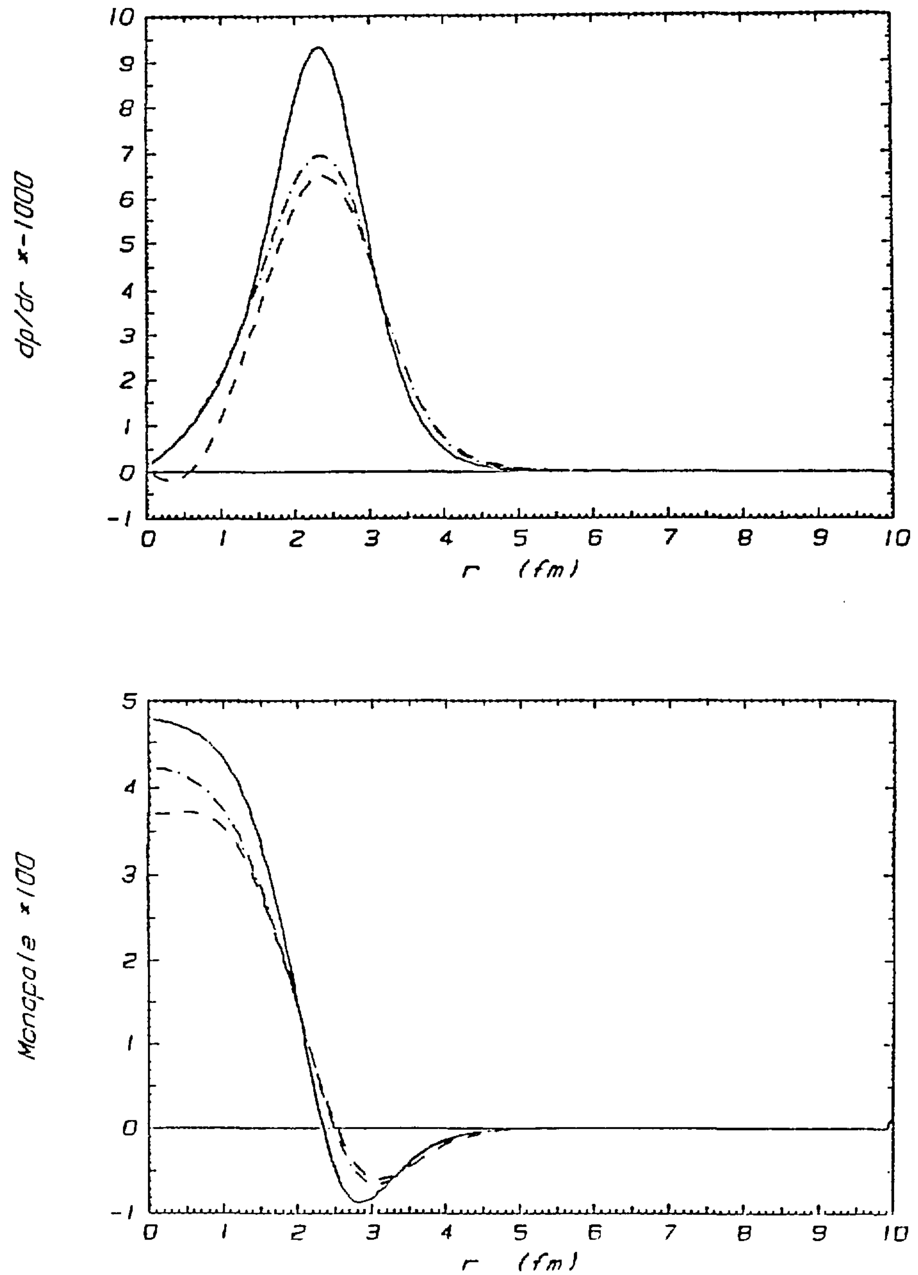

Figure 4.10 The transition densities used in the distorted wave calculations. The top figure shows the derivative densities used for all multipolarities except zero. The lower figure shows the monopole transition densities. In both cases the solid curves were generated from the three-parameter Fermi distribution discussed in the text while the dot-dashed and dashed curve were generated from the Skyrme neutron and proton densities respectively.

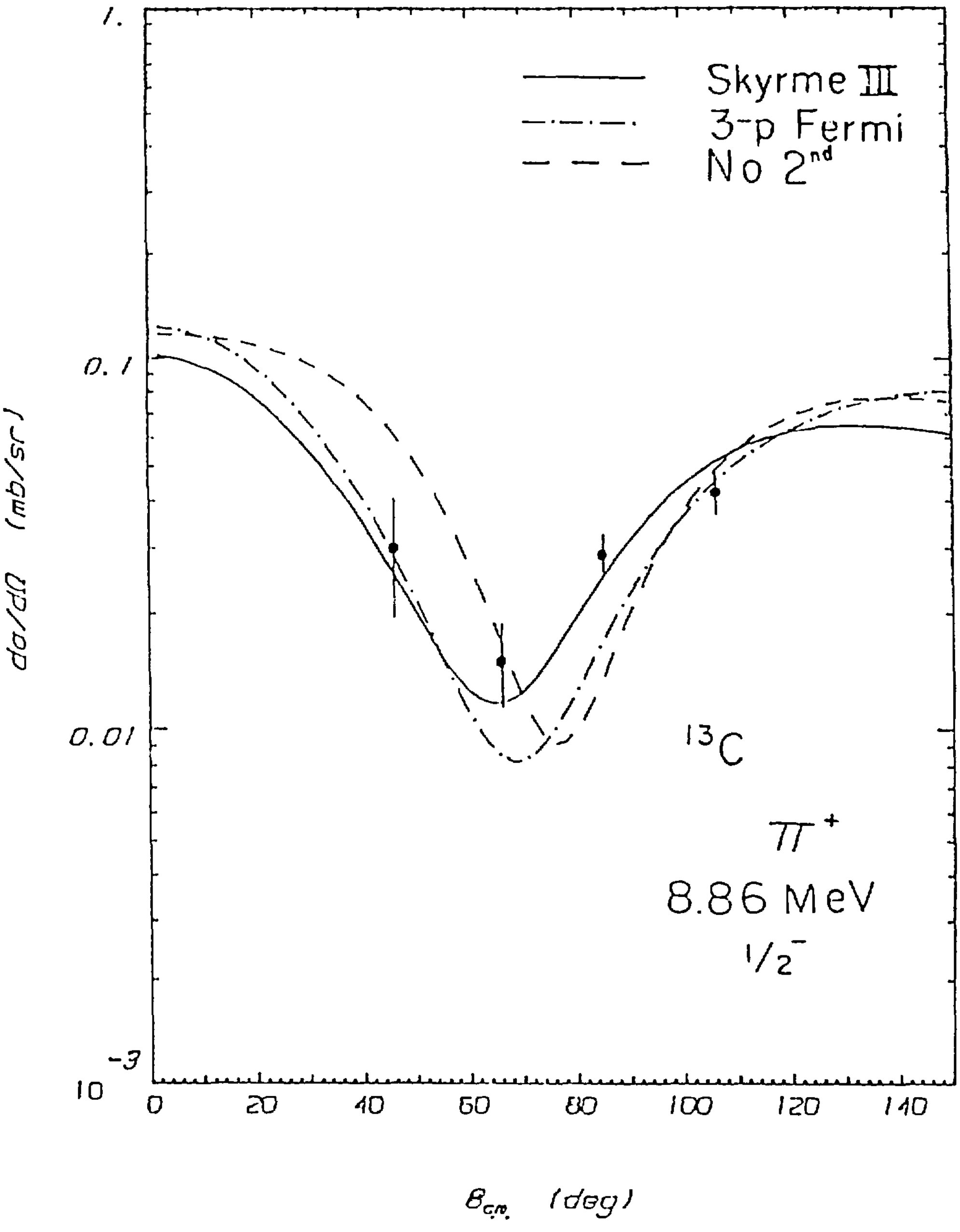

Figure 4.11 The data and calculations for π^+ scattering to the monopole transition at 8.86 MeV in excitation.

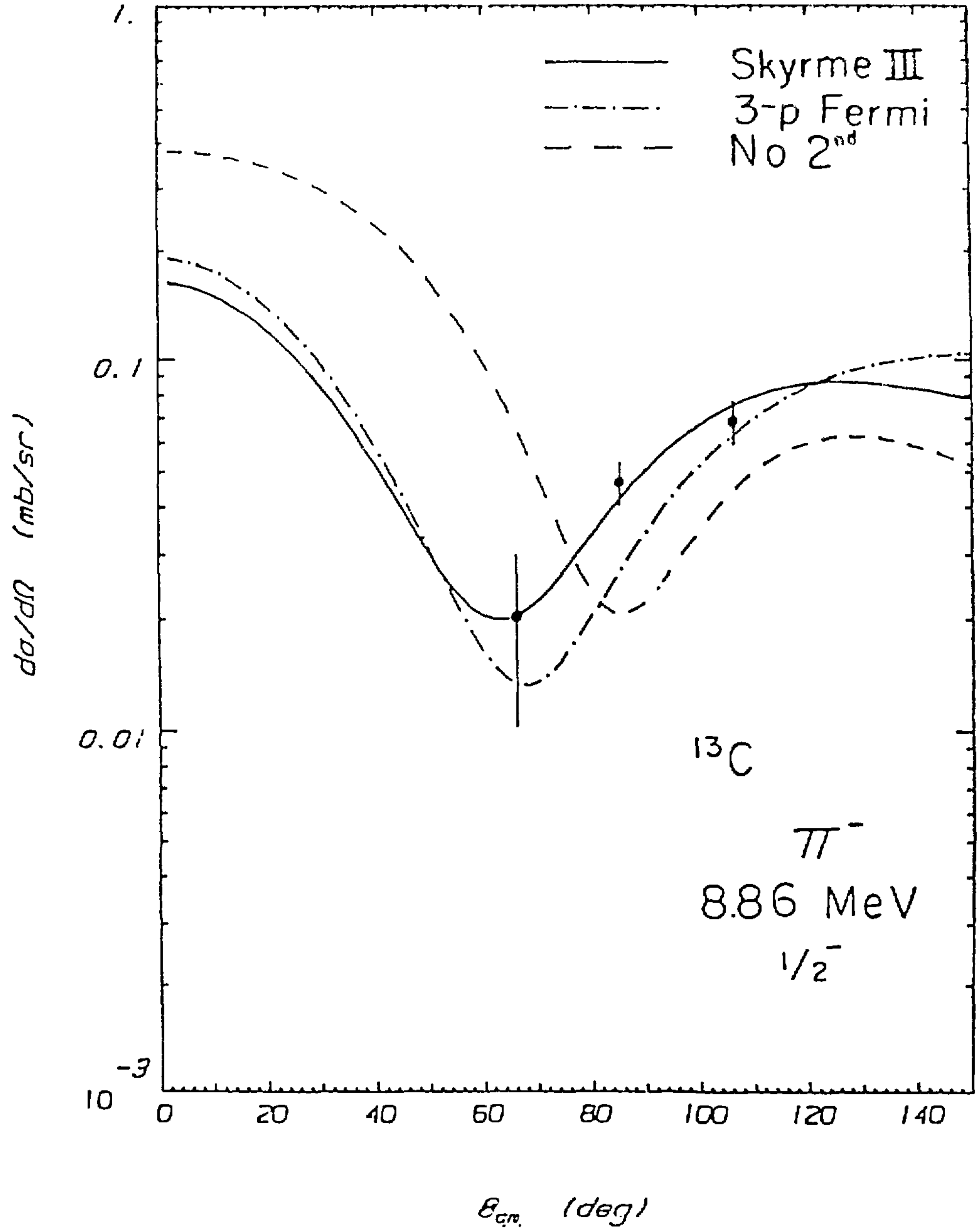

Figure 4.12 The data and calculations for π^- scattering to the monopole transition at 8.86 MeV in excitation.

Although there have been several inelastic scattering experiments performed using pions at higher energies [Ant 84][Sch 79][See 81], there were no published values of βR_- and βR_+ with which to compare ours. Antonuk et al. did not compare their data at T_π=100 MeV to any calculations. This is also the case with the data of Schwarz that were taken at T_π=180 MeV. Seestrom-Morris does report values of βR_n and βR_p but not $\beta R_\pm$. It was decided to obtain values for $\beta R_\pm$ at these energies by comparing the published data to new calculations. Antonuk published no distorted wave calculations with his data. Although Seestrom-Morris did publish calculations, new ones were made so that the all the calculations would be as consistent as possible.

The calculations at 100 MeV were performed using the second order parameters of Alons even though this is outside the energy region over which the parameters were fit. The calculations at T_π=162 MeV use the second order parameters of Greene et al. [Gré 84]. These parameters also include an energy shift as discussed by Cottingame [Cot 80]. All the calculations used the Skyrme densities for consistency. Figures 4.13-4.19 show the results of these calculations. The description of the data at 100 MeV is only fair. The fit to the data at 162 MeV is poor as the calculations do not have the correct diffractive behavior. This was expected since the Skyrme densities have larger rms radii than the density used by Seestrom-Morris in her analysis. However, at this energy the magnitudes of the calculations are mostly sensitive to the shape of the tails of the densities and not so much to their rms radii. Therefore, the βR's obtained from these calculations should be good within the quoted errors. Errors for all the βR's were obtained by examining the worst acceptable cases and do not include the overall normalization uncertainties of the data. Some calculations were made at $T_\pi = 180$ MeV for the purpose of comparison to the data of Schwarz et al. The π^+ and π^- calculations had almost identical magnitudes at this energy. For this reason it was decided to report only the value $\frac{\beta_+}{\beta_-}$ for these data as this quantity is not as sensitive to experimental normalizations as the individual deformation lengths are. The values quoted for this quantity here are just the ratios of the data found in [Sch 79].

Table 4.1 (at the end of this section) shows the results of this analysis as well as values of βR from 800 MeV proton scattering [Bla 78]. Comparing directly to the proton values is difficult as protons are sensitive to both the neutron and proton distributions in the nucleus. By this it is meant that protons are not as selective as pions. One might compare the quantity $\beta R_{avg} = (N\beta_- R + Z\beta_+ R)/A$ to the proton values although the justification is not as clear as at resonance. If one uses this prescription one finds that the values of βR_- and βR_+ obtained from this experiment seem to be in reasonable agreement with the proton results.

Now in comparing the present results for $\beta R_\pm$ with the results from the other pion experiments one does not necessarily expect perfect agreement as low energy pions are more sensitive to the nuclear interior than are pions of resonant energy. In addition 65 MeV pions do not discriminate as well between neutrons and protons as the pions in the 3,3 dominated experiments. Still one does expect qualitative agreement. As can be seen from the table, all the pion data agree (within errors) that all these collective excitations are somewhat proton-like in nature. In other words, these states are all more

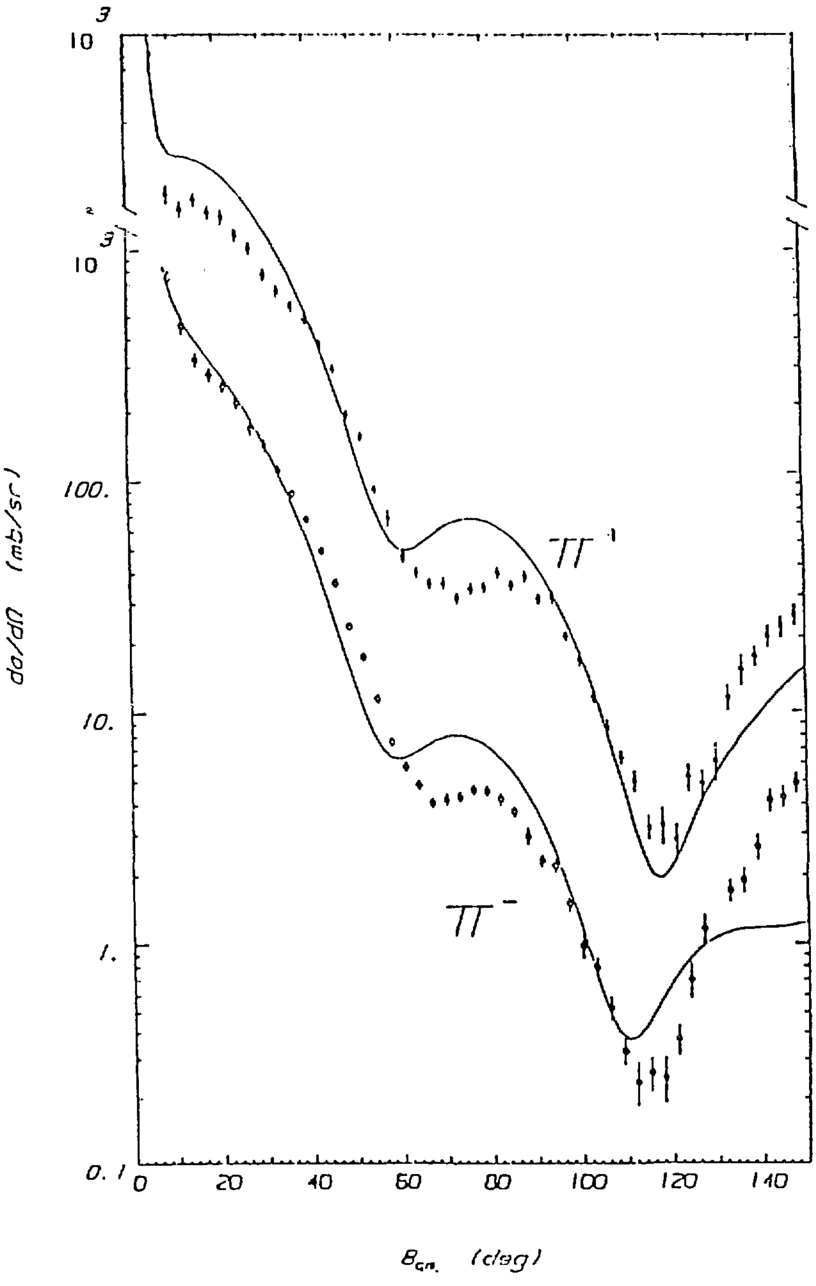

Figure 4.13 Elastic scattering at T_π=100 MeV. The data are those of Antonuk et al. [Ant 84] (π^+ solid points (top), π^- open points). The curves are the distorted wave calculations discussed in the text.

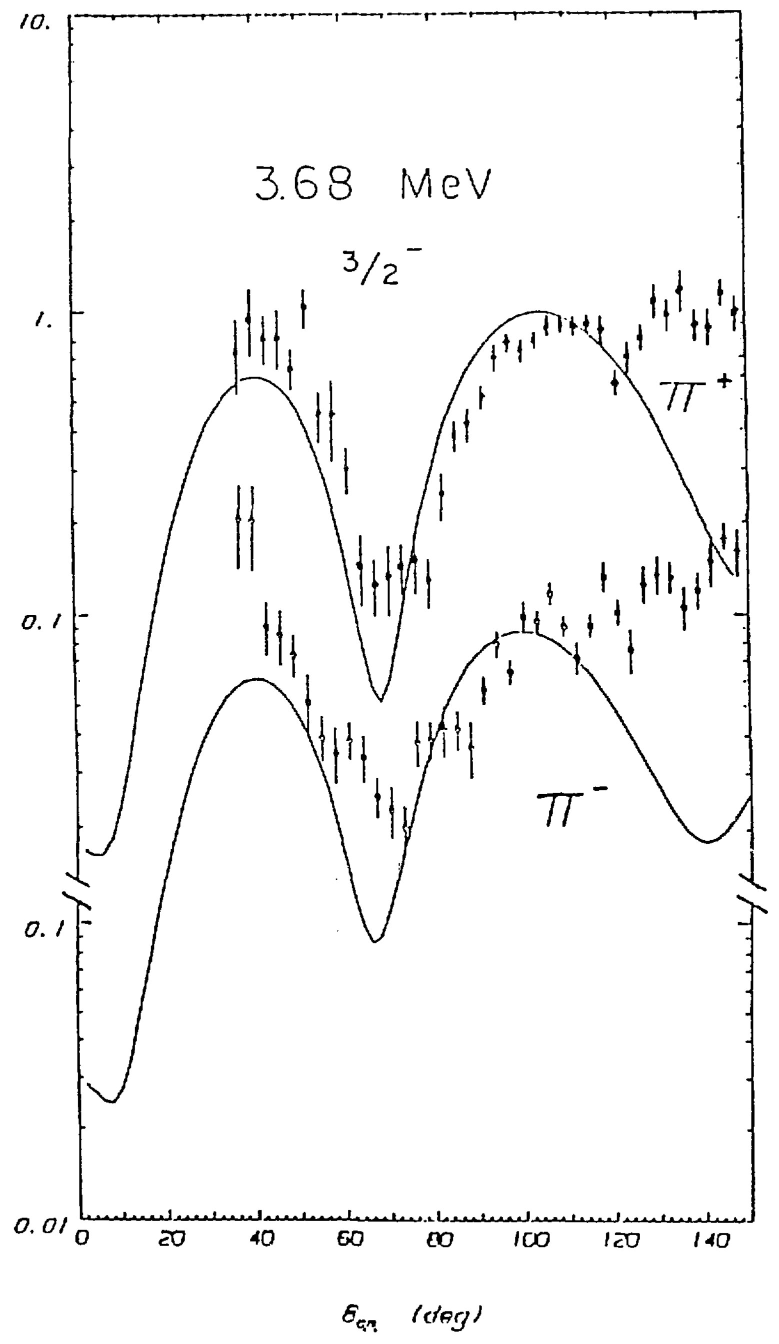

Figure 4.14 Measured and calculated cross sections for the scattering of 100 MeV pions to the state at 3.68 MeV. The data are those of Antonuk et al. [Ant 84] (π^+ solid points (top), π^- bottom). The curves are the distorted wave calculations discussed in the text.

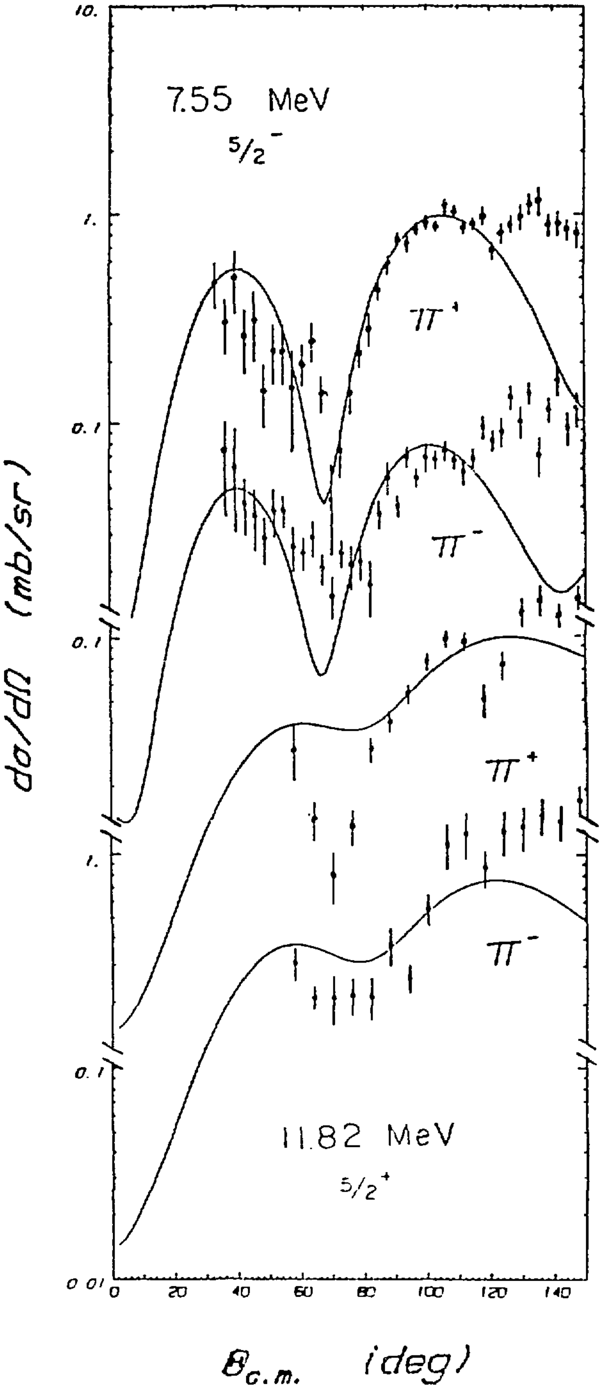

Figure 4.15 Measured and calculated cross sections for the scattering of 100 MeV pions to the states at 7.55 MeV (top two) and 11.82 MeV (lower two) in excitation. The data are those of Antonuk et al. [Ant 84] (π^+ solid points, π^- open points). The curves are the distorted wave calculations discussed in the text.

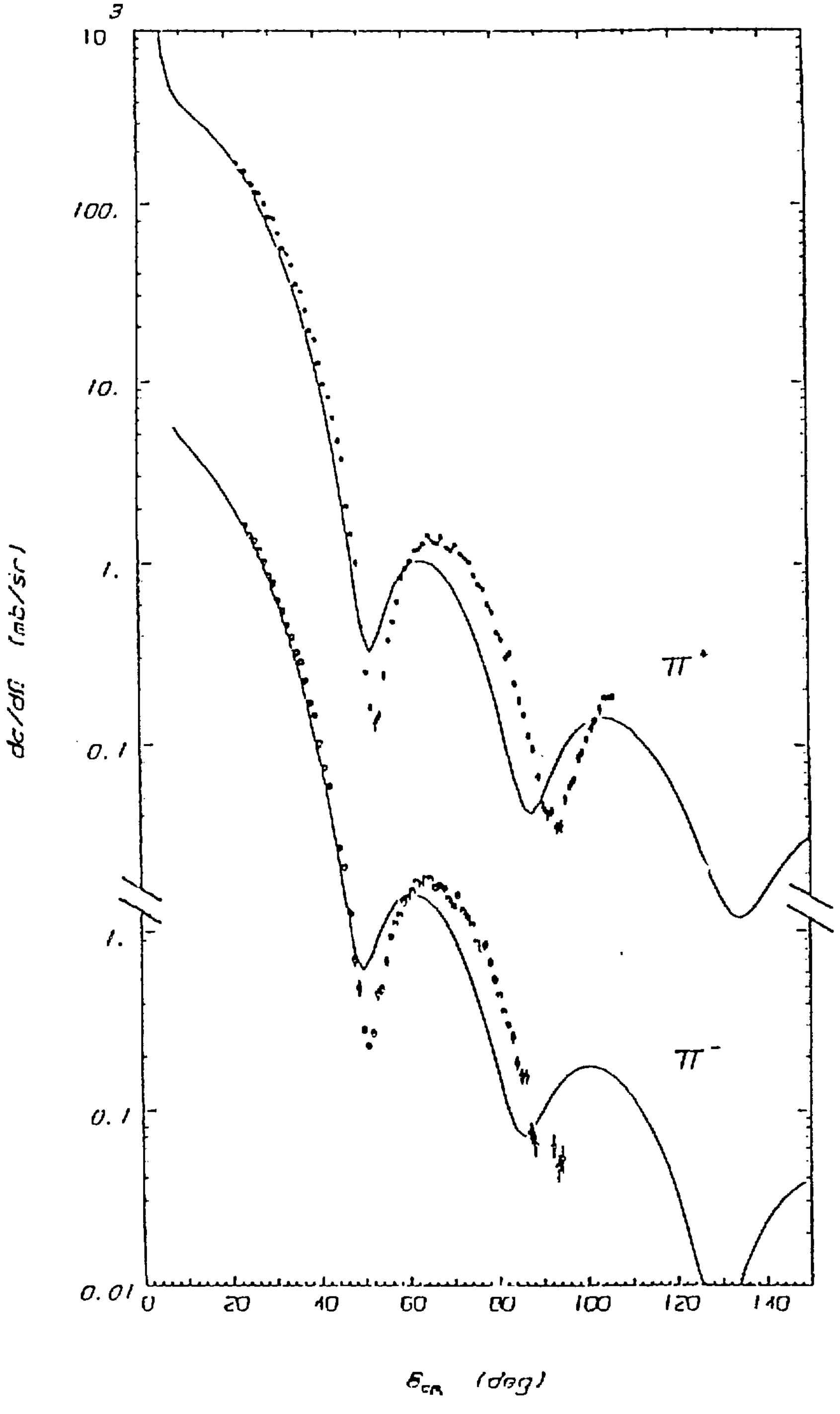

Figure 4.16 Measured and calculated cross sections for elastic scattering of pions at $T_\pi = 162$ MeV. The data are those of Seestrom-Morris [See 81]. The curves are the results of distorted wave calculations. The π^+ data are the solid points while the open points are for π^-.

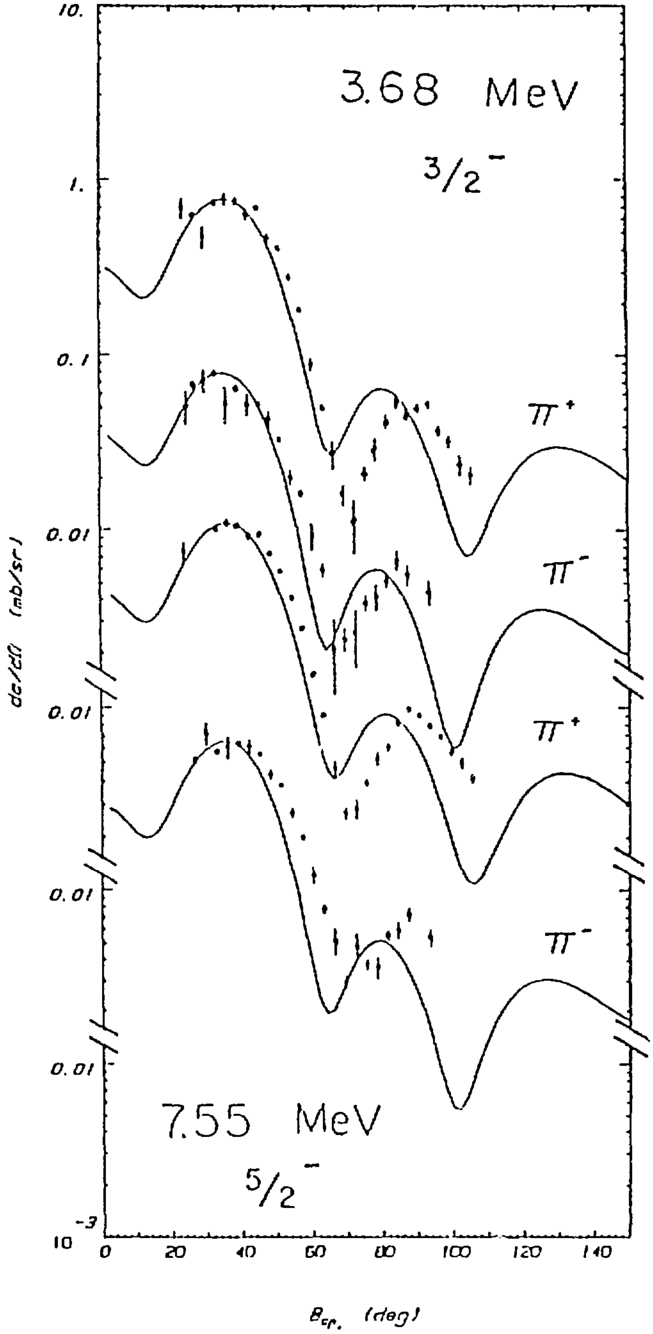

Figure 4.17 Measured and calculated cross sections the $L = 2$ transitions at 3.68 MeV (upper two) and 7.55 MeV in excitation. The data are those of Seestrom-Morris [See 81] and were taken at an incident pion energy of 162 MeV. The curves are the results of distorted wave calculations. As in all the figures the π^+ data are the upper set in each pair (solid points).

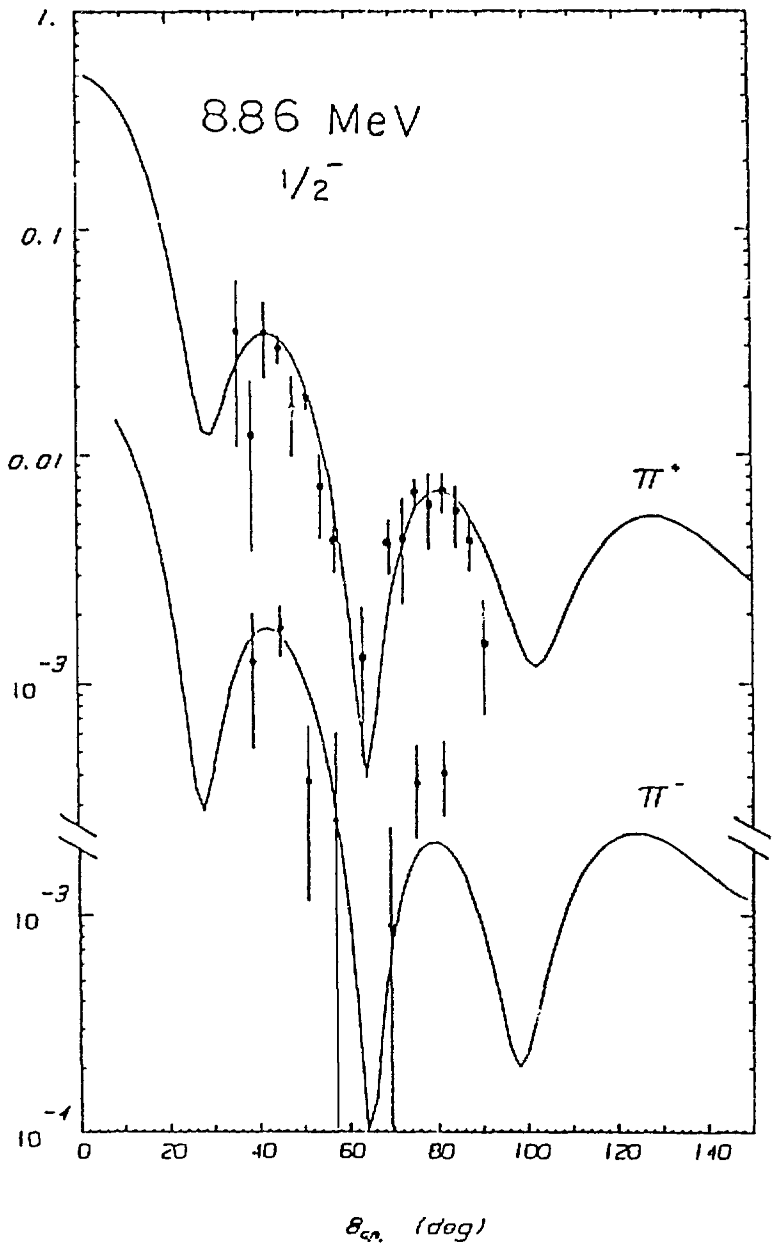

Figure 4.18 Measured and calculated cross sections for the scattering of pions to the state at 8.86 MeV (π^+ solid points, π^- open). The data are those of Seestrom-Morris [See 81] and were taken with an incident energy of 162 MeV. The curves are the results of distorted wave calculations.

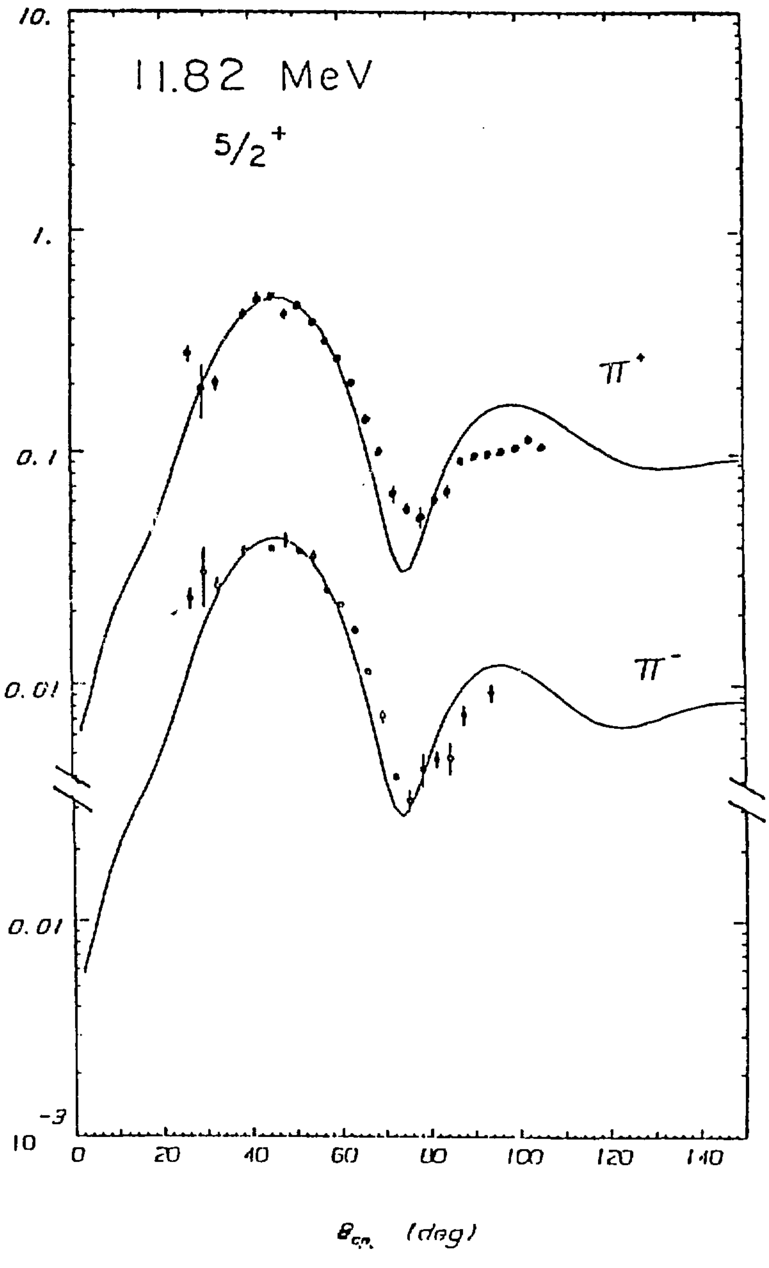

Figure 4.19 Measured and calculated cross sections for the scattering of pions to the state at 11.82 MeV (π^+ solid points, π^- open). The data are those of Seestrom-Morris [See 81] and were taken with an incident energy of 162 MeV. The curves are the results of distorted wave calculations.

strongly excited by positive pion beams. The absolute values of βR_+ and βR_- show less than spectacular agreement from experiment to experiment. This is probably due in part to the inconsistencies in the calculations at the different energies. Although an effort was made to make these calculations as consistent as possible, a truly consistent set is not possible at this time. These discrepancies could also reflect inconsistencies in the normalization of the experimental data. The ratio $\frac{\beta R_+}{\beta R_-}$ is expected to be less sensitive to these problems than either individual value. All the experiments show good agreement of this ratio for the two $L = 2$ transitions. The results for the $L = 3$ transition at 11.82 MeV seem to show a definite trend towards decreasing values of this ratio as the energy is increased. Given the quality of the available data it is hard to make any definitive statements about this behavior. Of the pion experiments only this experiment and the EPICS experiment at 162 MeV were able to resolve the $\Delta L = 0$ transition at 8.86 MeV. The agreement of the individual values of $\beta R_\pm$ obtained from these two sets of data is not very good. The resonant data have a much larger ratio of β_+/β_- than found at low energies. However, if one compares the values of $\beta_{avg} = (N\beta_- + Z\beta_+)/A$ for these two sets the agreement is very good. The state appears to be more proton-like at resonance than at low energies. Such a difference could be explained by a "tail" on the proton transition density which extends it to greater r values than the neutron transition density. This would effect the surface-dominated resonant cross sections far more than the cross sections for the deeply penetrating low energy pions. This type of effect would be particularly important for this transition as the monopole form factor has a node. In addition, it has been speculated that two-step processes, such as coupling through the $L = 2$ states, might be important for describing the monopole transitions in other nuclei and could perhaps be important here [Whi 86].

Peterson et al. report a value for the deformation parameter of $\beta = 0.10$ [Pet 81], obtained from the analysis of alpha scattering data to the state at 8.86 MeV. This value is in excellent agreement with the values of β_{avg} extracted from the two pion experiments. Because Peterson reports only values of β (not βR) for all the excitations a direct comparison of this work and his results is only possible for this state (the 8.86 MeV). However, in their paper Peterson et al. calculated asymmetries for resonant pion scattering. The asymmetry, A, is defined

$$A = \frac{d\sigma(\pi^-) - d\sigma(\pi^+)}{d\sigma(\pi^-) + d\sigma(\pi^+)}.$$

The asymmetry is another measure of the neutron or proton content of an excitation. They calculated these asymmetries by applying isospin relations to a unified analysis of $(\alpha, \alpha'), (^3He, t)$ and $(^3He, ^3He)$ reactions on ^{13}C. Their predicted asymmetries are in reasonable agreement with the measured asymmetries of Seestrom-Morris [See 81]. In order to predict the pion asymmetries Peterson et al. assumed (3,3) dominance for the pion reaction mechanism. Therefore, it is difficult to directly compare low energy data to their results. As a last note the measured asymmetries at resonance and the measured asymmetries at 65 MeV are different. One expects this as the reaction mechanism is quite different (as are the distortion effects). For this reason only deformation lengths are compared in this work.

The Spin Flip Transition at 9.5 MeV

All the transitions considered thus far have two features in common. First the collective model can be used to give an adequate description of their nuclear structure. Second, the spin-flip piece of the πA interaction is expected to play only a negligible role in their excitation. Neither of these conditions is expected to hold for the 9.5 MeV state which will now be considered.

This state is presumed to have a very pure single neutron particle hole structure. It is formed by promoting a $p_{\frac{3}{2}}$ neutron to the $d_{\frac{5}{2}}$ orbital. This is illustrated in figure 4.20. The spin and parity quantum numbers associated with this state are $J^{\pi} = \frac{9}{2}^{+}$. This is the highest value of J possible given this configuration of particles. States of this type are said to be stretched and are "nice" because they have comparatively simple nuclear structure.

Somehow this nuclear structure must be input into the distorted wave calculations. A prescription for accomplishing this can be found in the work of Lee and Kurath [Lee 80a] [Lee 80b]. They use the momentum space representation of the distorted wave impulse approximation and separate the πA T-matrix for inelastic scattering into two factors (essentially $t\rho$) one of which contains the reaction mechanism and another which contains the nuclear structure. This is no different than the approach that was used for the description of the collective states except that now they treat the

	3.68 MeV $\Delta L = 2$	7.55 MeV $\Delta L = 2$	8.86 MeV $\Delta L = 0$	11.82 MeV $\Delta L = 3$
$T_\pi = 65$ MeV				
βR_+	1.34±0.11	1.30±0.10	*0.1±0.01	1.48±0.13
βR_-	1.4±0.25	1.1±0.10	*0.09±0.01	1.02±0.07
βR_{avg}	1.37±0.14	1.19±0.07	*0.095±0.01	1.23±0.08
$\beta R_+/\beta R_-$	0.95±0.2	1.18±0.12	*1.11±0.15	1.45±0.11
$T_\pi = 100$ MeV				
βR_+	1.92±0.29	1.67±0.10		1.73±0.29
βR_-	1.73±0.43	1.30±0.15		1.45±0.35
$\beta R_+/\beta R_-$	1.11±0.3	1.28±0.13		1.2±0.3
$T_\pi = 162$ MeV				
βR_+	1.48±0.07	1.48±0.10	*0.130±0.008	2.12±0.09
βR_-	1.41±0.004	1.10±0.09	*0.075±0.01	1.84±0.08
$\beta R_+/\beta R_-$	1.04±0.05	1.34±0.11	*1.73±0.15	1.15±0.06
$T_\pi = 180$ MeV				
$\beta R_+/\beta R_-$	1.05±0.05	1.16±0.10		1.14±0.05
$T_{pro} = 800$ MeV				
βR	1.44±0.07	1.23±0.06		1.32±0.07

Table 4.1 The extracted deformation lengths, $\beta R_\pm$ (in fm), from this experiment as well as those extracted from other pion data [See 81][Ant 84][Sch 79]. Also included are the deformation lengths obtained by Blanpied et al. [Bla 78] from the analysis of 800 MeV proton scattering data. The results are discussed in the text.
* for this state the values quoted are $\beta_\pm$ not $\beta R_\pm$

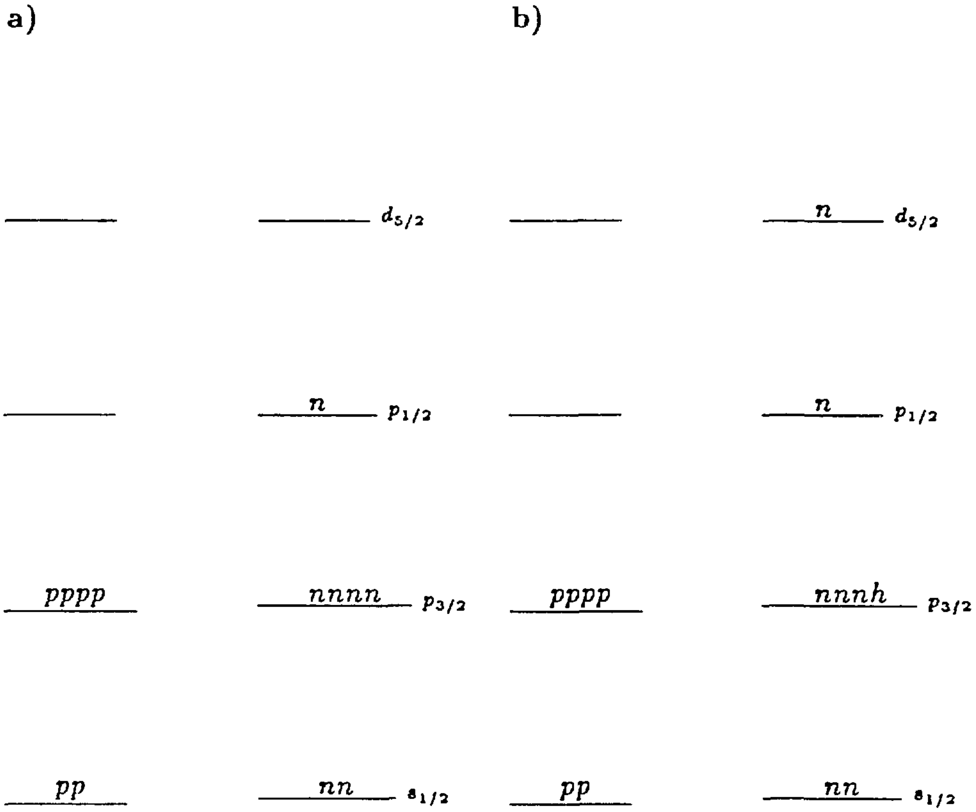

Figure 4.20 a) The shell structure of the ground state of ^{13}C. b) The particle-hole structure of the $\frac{9}{2}^+$ state at 9.5 MeV in excitation.

nuclear structure in terms of single-particle wave functions. This is called a microscopic approach to distinguish it from macroscopic treatments of structure such as the collective model. Lee and Kurath have shown [Lee 80b] that the nuclear structure piece of T, for non-normal parity transitions in $1p$-shell targets, can be written

$$\begin{aligned} F_L^{fiJT} S(r) = &\sum_l \langle J_f T_f ||| [b_{2l}^\dagger \times h_{1p}^\dagger]_{J(LS)T} || J_i T_i \rangle \\ &\times \sqrt{6 \hat{J} \hat{l}} \begin{pmatrix} l & 1 & L \\ 0 & 0 & 0 \end{pmatrix} R_{2l}(r) R_{1p}(r). \end{aligned} \tag{4.3}$$

In this equation $b_{2l}^\dagger$ is a particle creation operator. For the $\frac{9}{2}^+$ state $l = 2$, indicating the d shell. The operator $h_{1p}^\dagger$ creates a hole in the $1p$-shell, $l = 1$. These operators are coupled to the quantum numbers of the transition, J, L, S, and T, which for the transition of interest are $\Delta J = 4, \Delta L = 3, \Delta S = 1$. ΔT is determined by the neutron character of this transition. The radial wave functions of the particle and hole, R_{2l} and R_{1p} also appear in equation (4.3). The other factors in this expression are associated with the angular momentum coupling and therefore present little difficulty.

In order to make microscopic distorted wave calculations one needs the radial wave functions for the particle and hole and one needs the reduced matrix elements of the particle-hole creation operator. The radial wave functions were calculated by ALLWLRD [Car 81a] using a harmonic oscillator well. The reduced matrix elements for the particle-hole operators are usually calculated separately for the neutron and proton pieces or equivalently the isovector and isoscaler pieces of transitions. This was done by Lee and Kurath [Lee 80b] and they obtained values of $Z_n = 0.635$ and $Z_p = 0.001$

were the Z's are the nuclear matrix elements for promoting a neutron or proton from the $p_{\frac{3}{2}}$ orbital to the $d_{\frac{5}{2}}$ orbital. The isovector and isoscaler Z's are related to the neuton and proton matrix elements by

$$Z_0 = \frac{1}{\sqrt{2}}(Z_n + Z_p)$$

$$Z_1 = \frac{1}{\sqrt{2}}(Z_n - Z_p).$$

The Lee and Kurath values for these matrix elements are then $Z_0 \approx Z_1 = 0.449$. From a consistent analysis of electron, proton,^3He, and resonant pion scattering Hicks et al.[Hic 86] found that the above values are quenched. The values that they found empirically are $Z_0 = 0.27$ and $Z_1 = 0.28$. These values of Z_0 and Z_1 were used in all the calculations contained in this work.

This state is excited via the spin-flip piece of the πA interaction. In the calculations performed here the strength of this part of the interaction was obtained from the πN phase shifts of Arndt's FP85 solution [Arn 85] by using expressions similar to those for g_1 and g_0 in chapter 2. Therefore the calculations are completely constrained and absolutely normalized.

Figure 4.21 shows calculations of the angular distributions for scattered pions of both charges with incident energy of 162 MeV. The data are those of Seestrom-Morris et al.[See 81]. The distorted waves were generated by the code `MSUDWPI` using the same parameters that were used in the calculations of the collective states at this energy. The curves give an excellent description of the data in both shape and magnitude.

Figure 4.22 shows a similar set of calculations and a comparison to the experimental results of Antonuk et al. [Ant 84] at T_π=100 MeV. The data do not seem to have the characteristic shape that one expects for a

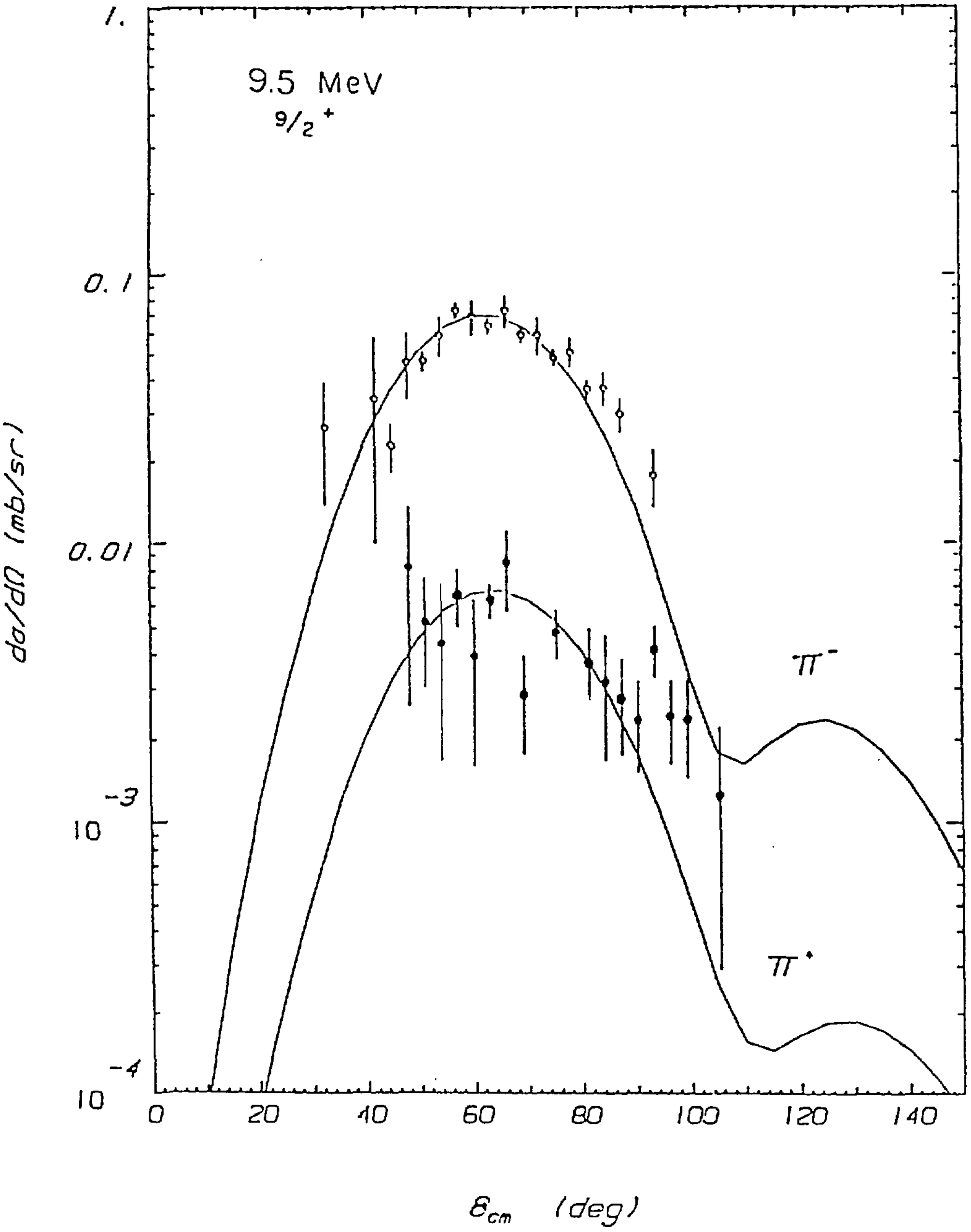

Figure 4.21 The data (π^+ solid points, π^- open) and absolutely normalized calculations for the scattering of pions to the $\frac{9}{2}^+$ state at 9.5 MeV. The data are those of Seestrom-Morris and were taken at an incident energy of 162 MeV.

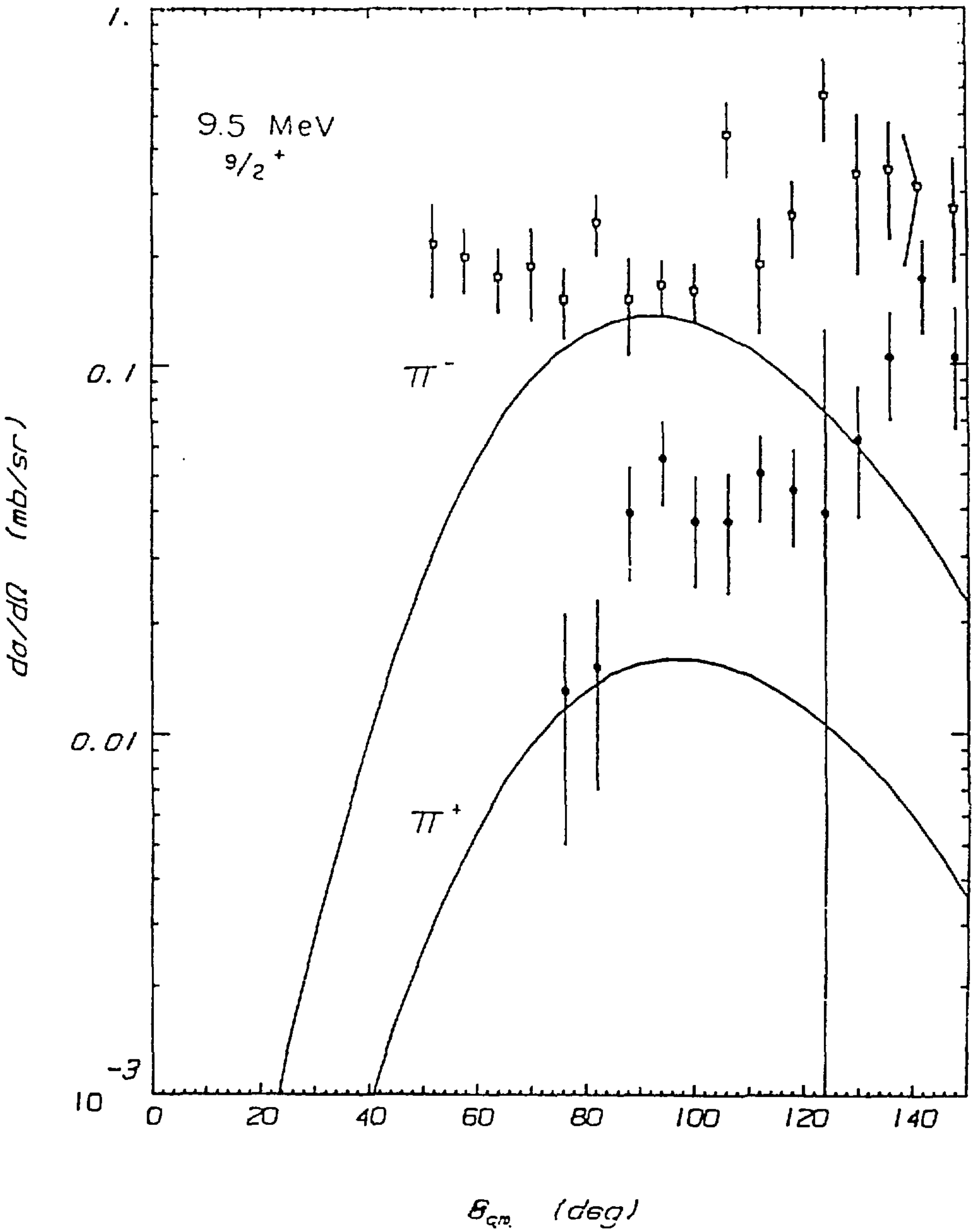

Figure 4.22 The data of Antonuk et al. (π^+ solid points, π^- open) for the scattering of pions to the $\frac{9}{2}^+$ state. The curves are absolutely normalized distorted wave calculations.

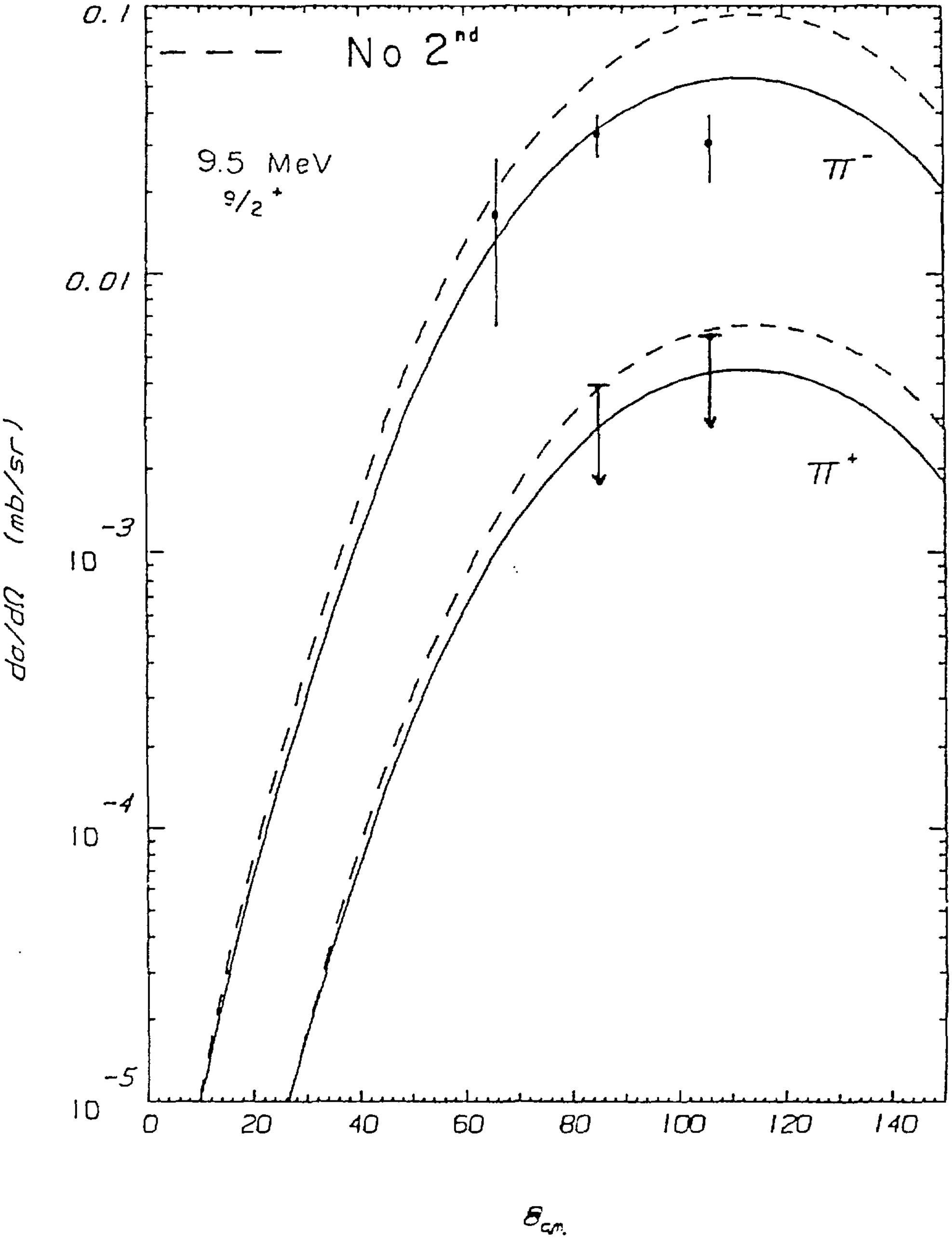

Figure 4.23 Measured π^- cross sections and upper limits for π^+ for scattering to the $\frac{9}{2}^+$ state. The curves are absolutely normalized distorted wave calculations. The dashed curves has the second order terms set to zero.

spin-flip excitation in pion scattering. As pions have an intrinsic spin of zero the only way they can excite non-normal parity states is through a target spin-flip. This can only be accomplished by the spin orbit piece of the πA or πN interaction. The spin- flip piece of the πN amplitude contains the operator $\vec{\sigma} \cdot \hat{n}$ where $\hat{n}$ a unit vector normal to the scattering plane. As the scattering plane is an ill defined concept at zero degrees one expects all spin-flip transitions to have zero cross section at zero degrees. This trend is not evident in the π^- data at this energy. Perhaps there are unresolved states which are influencing the angular behavior of the cross sections for these data.

Finally, Figure 4.23 shows the data and calculations for 65 MeV. As can be seen it was not possible to extract reliable cross sections for π^+ scattering to this state. Therfore, only upper limits are reported. These upper limits correspond to 70% confidence levels as compared to the best fit estimates. These best fit estimates included effects from the uncertainty in the background for this state. The calculated cross section for π^- scattering to this state is in very good agreement with the data. Again it can be seen that the calculations are sensitive to the presence of the second order potential in the distorted waves and that their inclusion provides a better description of the data. It should be pointed out again that these calculations were absolutely normalized.

Data for the State at 9.9 MeV

This transition has been identified as a non-collective $L = 2$ [Ajz 81]. However the angular distribution that was obtained does not seem to have the expected shape. No calculations were made for this state due to lack of guidance as to the correct handling of the nuclear structure. The cross sections are based on few counts and have a high uncertainty. No other pion data for scattering to this state exist in the literature. Figure 4.23 shows the results of our measurements. Note that the cross sections for π^+ and π^- scattering to this state are essentially equal

In addition to the states discussed, a rather strong set of excitations were seen at about 11.0 MeV in excitation, but since the results of the analysis of this bump were not consistent between π^+ and π^- scattering it is impossible to draw any conclusions. There were also several groups of unresolved states observed at higher excitations.

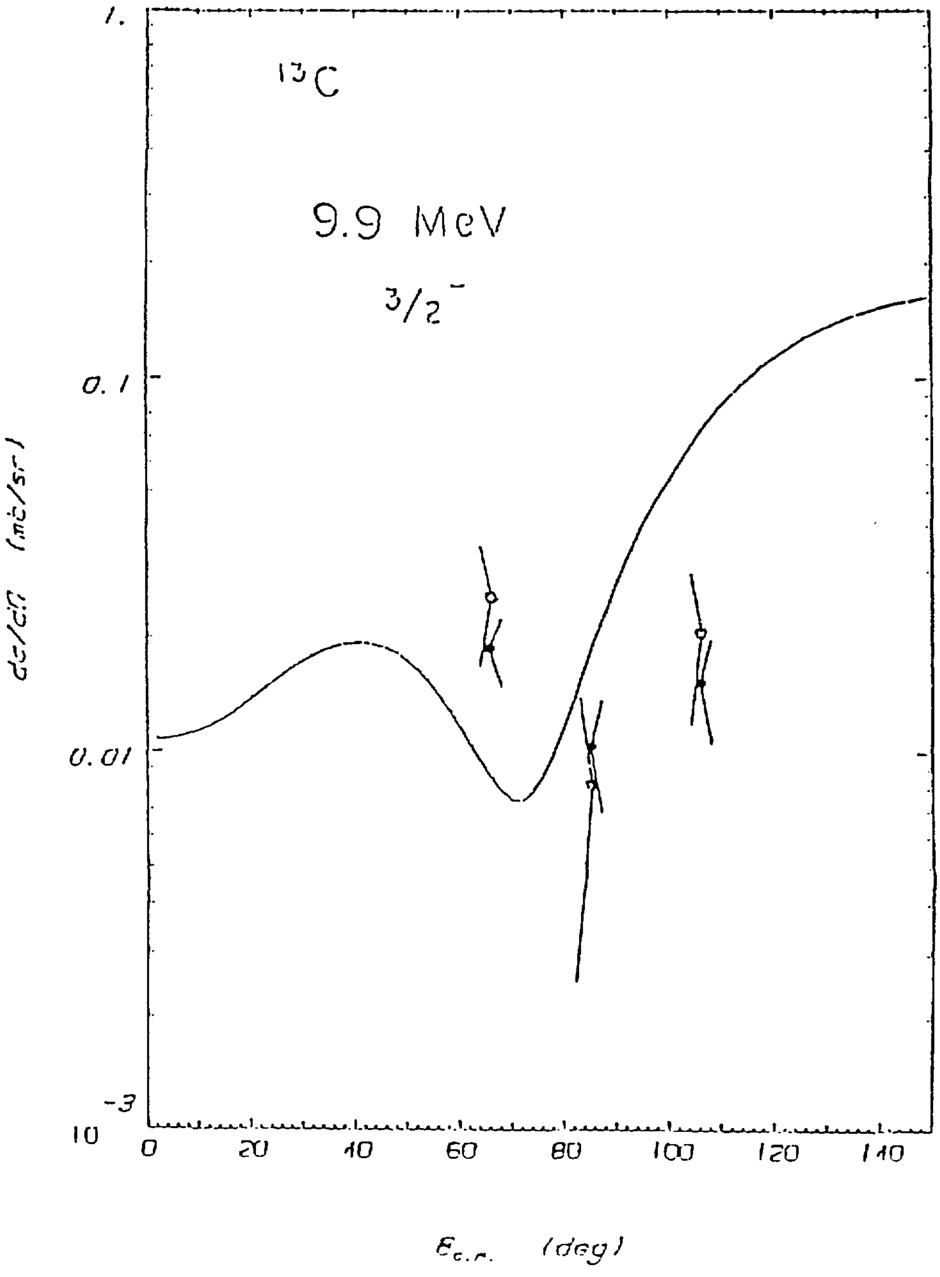

Figure 4.24 The measured cross sections (π^+ solid points, π^- open) for scattering to the state at 9.9 MeV in excitation.

CHAPTER V

EXCITATION FUNCTIONS

Thus far all the data presented have been in the form of angular distributions. In these measurements the beam energy is held fixed and the angle of detection is varied, thus varying the momentum transfer. In this chapter another class of measurements, fixed $|\vec{q}|$ excitation functions, will be examined. In these experiments the magnitude of the three-momentum transfer is held constant and differential cross sections are measured at various laboratory angle and energy combinations that are consistent with the fixed value of $|\vec{q}|$ chosen. The three-momentum transfer $\vec{q}$ is defined by

$$\vec{q} = \vec{k} - \vec{k}'. \tag{5.1}$$

For elastic scattering ($|\vec{k}| = |\vec{k}'|$) the magnitude of $\vec{q}$ is given by

$$|\vec{q}| = q = 2|\vec{k}| \sin\frac{\theta}{2}. \tag{5.2}$$

This result holds in the lab or center of mass provided $|\vec{k}|$ and θ are evaluated in the frame of interest. The magnitude of the pion momentum, $|\vec{k}| = k$, is related to its kinetic energy T by

$$E^2 = (T + m_\pi)^2 = k^2 + {m_\pi}^2.$$

The expression for q (equation (5.2)) can be written

$$q = 2\sqrt{T^2 + 2m_\pi T} \sin\frac{\theta}{2}. \tag{5.3}$$

In order to keep q constant as the kinetic energy, T, is decreased, θ must be increased.

Why Fixed $|\vec{q}|$ Excitation Functions?

One motivation for measuring fixed $|\vec{q}|$ excitation functions is that in the one photon exchange approximation the nuclear structure form factors evaluated from electron scattering data are functions of q only [Don 75]. Therefore, by staying at fixed q the sensitivity to the nuclear structure is minimized. If it were possible to make consistent calculations over a large range of energies the comparison of these calculations with measured excitation functions would be a good way to check the energy dependence of the reaction mechanism used in the calculations. This is not currently possible for pion scattering as there is no consistent treatment of the ρ^2 parts of the πA interaction over a large energy range. The present excitation functions address this problem by providing a wide range of data.

Another motivation for performing these measurements comes from the work of Siciliano and Walker [Sic 81]. They have shown that fixed q excitation functions at energies near the (3,3) resonance provide a clear signature as to whether a given nuclear excitation has natural or unnatural parity. Their treatment was motivated by the Rosenbluth decomposition [Don 75] that is used in the analysis of electron scattering data to separate the transverse and longitudinal pieces of electromagnetic form factors. The result of their work is that the differential cross section for inelastic pion scattering at fixed q may be written

$$\frac{d\sigma}{d\Omega}(q_\circ, T, \theta) = \Gamma(E)\left[4\mathcal{M}^2(q_\circ)\cos^2\theta + \mathcal{S}^2(q_\circ)\sin^2\theta\right]. \qquad (5.4)$$

The form shown above was derived by using eikonal distorted waves, a first order optical potential, and assumes (3,3) dominance for the amplitudes. In this expression $\mathcal{M}$ is the form factor for spin-nonflip transitions while $\mathcal{S}$ is the form factor associated with spin-flip transitions. These form factors are approximately only functions of q_o. More precisely, they do not have a strong energy dependence or at least they have the same energy dependence for values of q near the diffraction maximum. The factor $\Gamma(E)$ in the above expression reflects the common energy dependence of $\mathcal{M}$ and $\mathcal{S}$ as well as the energy dependence of the distortions. Its energy dependence is expected to be like that of the πN total cross section. The net result of this analysis is that over the region where the approximations are expected to be good, fixed-q excitation functions for spin-flip and spin-nonflip states have angular dependences given by $\sin^2\theta$ and $\cos^2\theta$, respectively. Therefore these excitation functions can be used to identify the spin-flip content of a transition. This treatment has been shown to be useful by comparing to the data of Peterson et al. [Pet 80] as well as that of Seestrom-Morris et al. [See 81].

Several of the simplifying assumptions made by Siciliano and Walker are questionable for pion energies below 100 MeV. In particular the assumption that the $p_{3,3}$ partial wave dominates is not expected to be good. However, the contributions from the s-wave piece of the interaction are isotropic by definition and only contribute to spin-nonflip interactions. Therefore the angular behavior of the fixed q excitation funtions may still be qualitatively described by equation (5.4).

The Data

Two sets of excitation functions coresponding to two different values of the momentum transfer will be presented. These values are $q \approx 0.96\ \mathrm{fm}^{-1}$ and $q \approx 1.1\ \mathrm{fm}^{-1}$. These momentum transfers correspond to lab angles of 84 and 105 degrees at a beam energy of 65 MeV. These are the two back angle points in the 65 MeV angular distributions of chapter 4. Due to the large mass mismatch between the projectile and the target nucleus the lab and center of mass frames are almost identical. For reference all quantities quoted in this chapter are evaluated in the center of mass unless otherwise stated. The larger momentum transfer was picked so that the work of Seestrom-Morris [See 81] could be extended to lower energy. The other point, $q \approx 0.96\ \mathrm{fm}^{-1}$, was chosen to allow inclusion of a back angle point measured with an incident pion energy of 50 MeV. At this energy, 50 MeV, and momentum transfer, $0.96\ \mathrm{fm}^{-1}$, the lab angle of the spectrometer is 105 degrees. This is the largest angle that can be accommodated using the spectrometer in its standard configuration. Before the results are presented a few words about the 50 MeV data are necessary.

The data at $T_\pi = 50$ MeV were all taken at a lab angle of 105 degrees. The setup of the Clamshell was identical to the setup used for the measurements at $T_\pi = 65$ MeV. The same type of pulse height cuts were made on these data as were made on the data at 65 MeV. However, as the rate of energy loss dE/dx is higher the polynomial used to straighten the curve associated with pion events in a dot-plot of pulse height against missing mass had to be recalculated at this energy (see chapter 2). These data have a resolution of 500 keV, worse as a fraction of the incident energy than obtained at 65 MeV. These 50 MeV data are for π^- only and were normalized by comparing measurements of pions elastically scattered from a ^{12}C target to the cross sections of Sobie et al. [Sob 84]. The errors shown are mostly statistical but include, when appropriate, additional errors due to uncertainties in the peak fitting process. The systematic uncertainty in these data is estimated to be 13%. This is dominated by the uncertainty in Sobie's data which is reported as 10%.

Excitation Functions for $q \approx 0.96$ fm^{-1}

The figures show measured π^- excitation functions for the states at 3.68 MeV, 7.55 MeV, 9.50 MeV, and 11.82 MeV in excitation. The data shown at 50 MeV and at 65 MeV are from this work. The points at 100 Mev are from the work of Antonuk et al. [Ant 84] while the points at 180 MeV are from the work of Schwarz et al.[Sch 79]. Both these data sets were discussed earlier (chapter 4) and both these experiments were performed at SIN. In addition many of the figures include a point at 162 MeV from the work of Seestrom-Morris [See 81]. All the points from the other publications are those for which the momentum transfer is most nearly equal to 0.96 fm^{-1}. Since the momentum transfers of these points are not exactly 0.96 fm^{-1} approximate signs (instead of equal signs) have been used throughout this work whenever values of the momentum transfer are quoted. The actual momentum transfers of all the points are always within 0.05 fm^{-1} of the quoted value. The collective excitations at 3.68 MeV ($\frac{3}{2}^-$), 7.55 MeV ($\frac{5}{2}^-$), and 11.82 MeV ($\frac{5}{2}^+, \frac{7}{2}^+$) are all expected to be dominated by the spin-nonflip amplitudes and hence should have an angular dependence that looks like $\cos^2\theta$. For the 3.68 MeV and 7.55 MeV states this assertion has been confirmed by the electron scattering data of Yang et al. [Yan 71]. Yang found that the longitudinal form factor is greater than the transverse form factor by a factor of approximately 15 for the 3.68 MeV state and by greater than 30 for the state at 7.55 MeV. Any spin-flip component of these two transition would contribute to the transverse form factor. Therefore, these states should undergo reasonably pure spin-nonflip transitions. The curves shown in the figure are plots of $\cos^2\theta$ that have been normalized arbitrarily. These states are all in qualitative agreement with the predicted angular distributions. The point at 65 MeV was measured at a lab angle of 84 degrees and hence should have approximately zero cross section if the simple $\cos^2\theta$ behavior were rigorously true. It appears that the contribution of the s-wave reduces the depth of the observed minimum.

The $\frac{9}{2}^+$ state at 9.5 MeV in excitation is expected to be purely spin-flip in nature. This has been confirmed by both electron scattering [Hic 86] and by higher q pion excitation functions that were taken at higher energies [See 81]. The curve shown is a plot of $\sin^2\theta$ that is again normalized arbitrarily. Again the curve describes many qualitative features of these data, although the low resolution point of Antonuk seems to be out of place.

Excitation Functions for $q \approx 1.1$ fm^{-1}

These excitation functions are largely from the π^+ data of Seestrom-Morris et al. [See 81]. The new additions presented here are the point at 65 MeV which is a result of the π^+ measurements that I made on the Clamshell

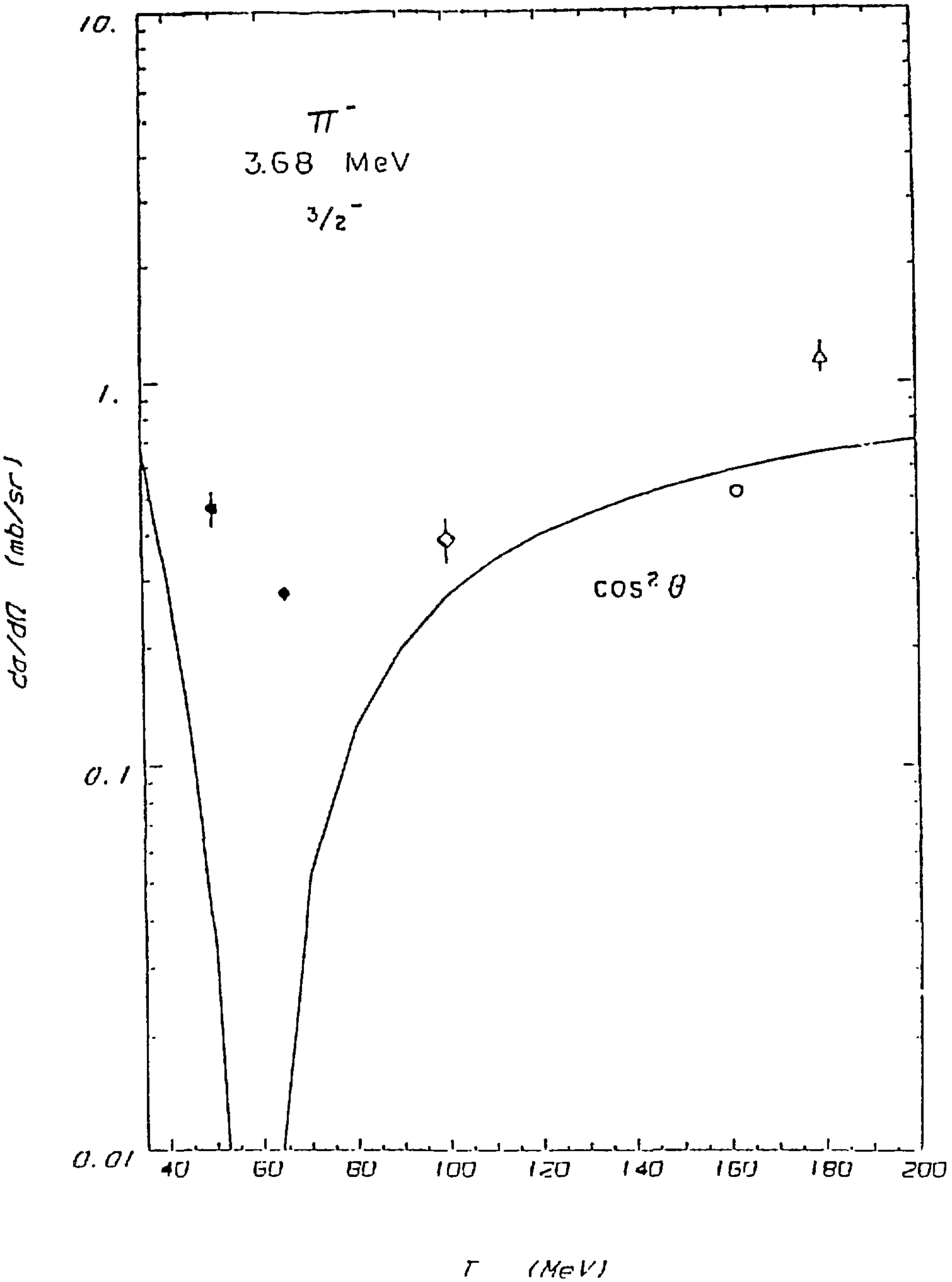

Figure 5.1 Fixed $q \approx 0.96$ fm^{-1} π^- excitation function for the state at 3.68 MeV in excitation. This state is expected to make a natural parity $\Delta J = 2$ transition from the ground state. The curve is a plot of $\cos^2\theta$ which has been normalized arbitrarily. The two solid points were measured in this work. The diamond is from the work of Antonuk [Ant 84]. The open circle is from the work of Seestrom-Morris [See 81] and the triangle is from the work of Schwarz [Sch 79].

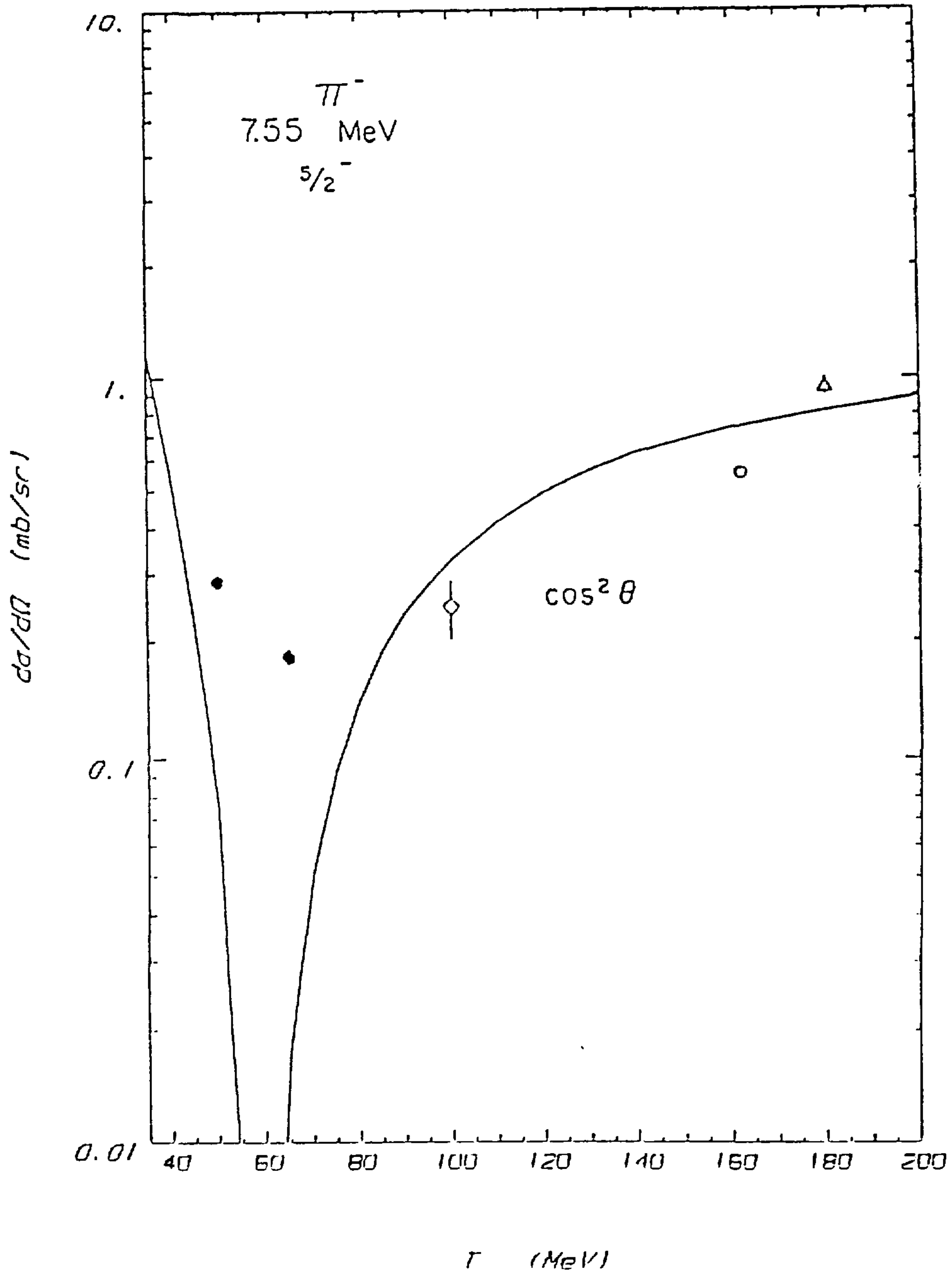

Figure 5.2 Fixed $q \approx 0.96$ fm^{-1} π^- excitation function for the state at 7.55 MeV in excitation. This state is expected to make a natural parity $\Delta J = 2$ transition from the ground state. The curve is a plot of $\cos^2\theta$ which has been normalized arbitrarily. The two solid points were measured in this work. The diamond is from the work of Antonuk [Ant 84]. The open circle is from the work of Seestrom-Morris [See 81] and the triangle is from the work of Schwarz [Sch 79].

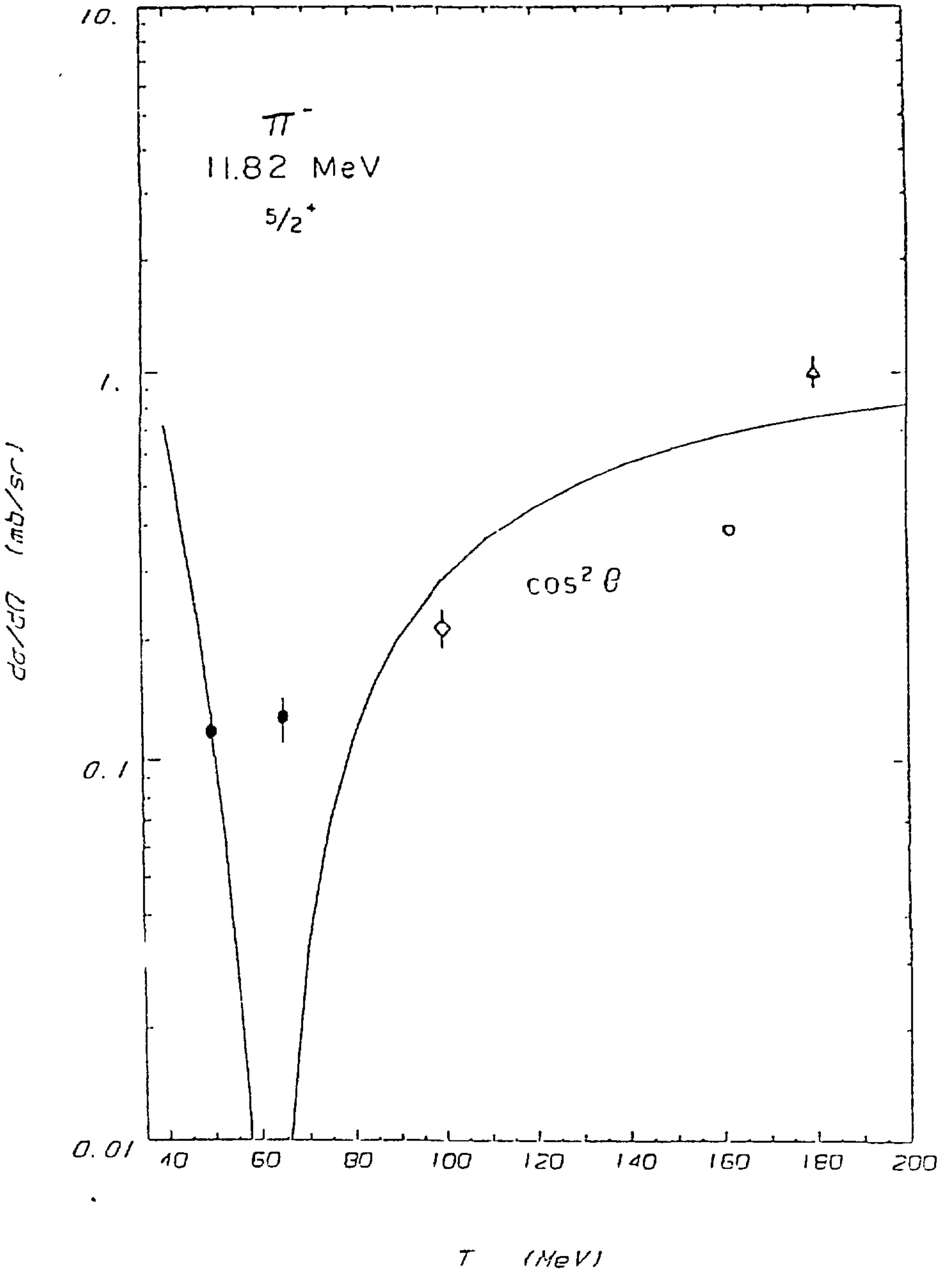

Figure 5.3 Fixed $q \approx 0.96$ fm^{-1} π^- excitation function for the state at 11.82 MeV in excitation. This state is expected to make a natural parity $\Delta J = 3$ transition from the ground state. The curve is a plot of $\cos^2\theta$ which has been normalized arbitrarily. The two solid points were measured in this work. The diamond is from the work of Antonuk [Ant 84]. The open circle is from the work of Seestrom-Morris [See 81] and the triangle is from the work of Schwarz [Sch 79].

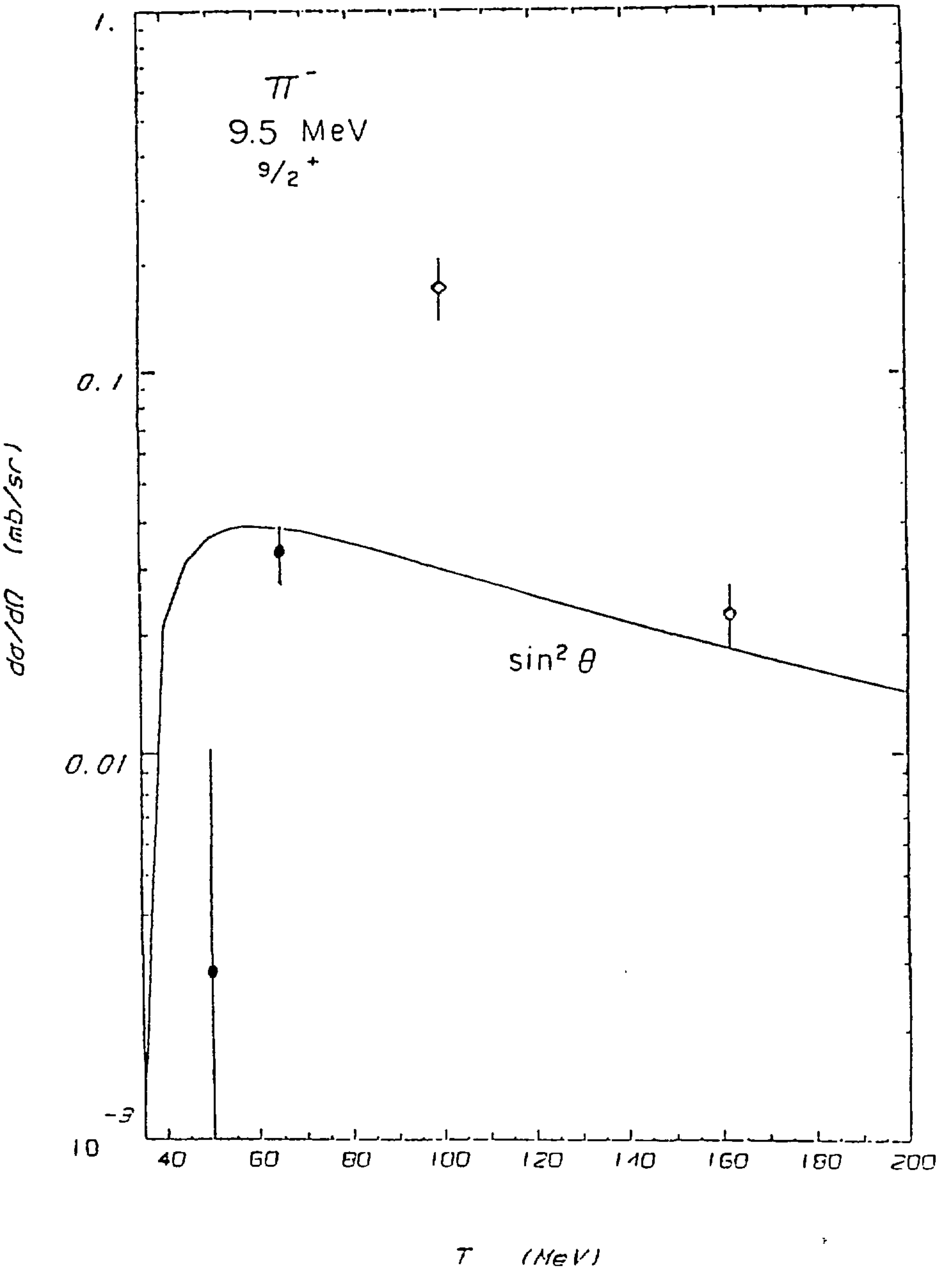

Figure 5.4 Fixed $q \approx 0.96\ \mathrm{fm}^{-1}$ π^- excitation function for the state at 9.50 MeV in excitation. This state is a very pure spin-flip excitation and hence has unnatural parity. The curve is a plot of $\sin^2\theta$ with arbitrary normalization. The two solid points are from this work. The diamond is from the work of Antonuk [Ant 84]. The open circle is from the work of Seestrom-Morris [See 81].

and for comparison the π^+ points of Antonuk and of Schwarz have been included. Actually the point at 65 MeV had a momentum transfer of 1.14 fm^{-1}. The angular distributions for the two $\Delta J = 2$ transitions (the states at 3.68 MeV and 7.55 MeV) are rising rapidly at this q value. Therefore in addition to the actual data point (solid circle) the figures include a solid square point that marks the extrapolation along the calculated angular distribution to a q of exactly 1.1 fm^{-1}. Once again the curves shown are normalized arbitrarily and they seem to describe the data qualitatively. Only the low energy data exhibit the striking rise beyond the zero of the $\cos^2\theta$. This again confirms the simple $\cos^2\theta$ tendency. The excitation function for the $\frac{1}{2}^-$ state at 8.86 MeV is slightly ambiguous as all these data have relatively large errror bars. Selection rules allow for both $\Delta J = 0^+$ and $\Delta J = 1^+$ transitions to this state from the ground state. For this reason both $\sin^2\theta$ and $\cos^2\theta$ are shown. The data seem to confirm that the spin-nonflip $\Delta J = 0^+$ transition is favored. This is the same conclusion reached by Seestrom-Morris [See 81]. In general the method of Siciliano and Walker seems to do better than might have been expected at reproducing the angular trends of the low energy data far below the assumed (3,3) dominance

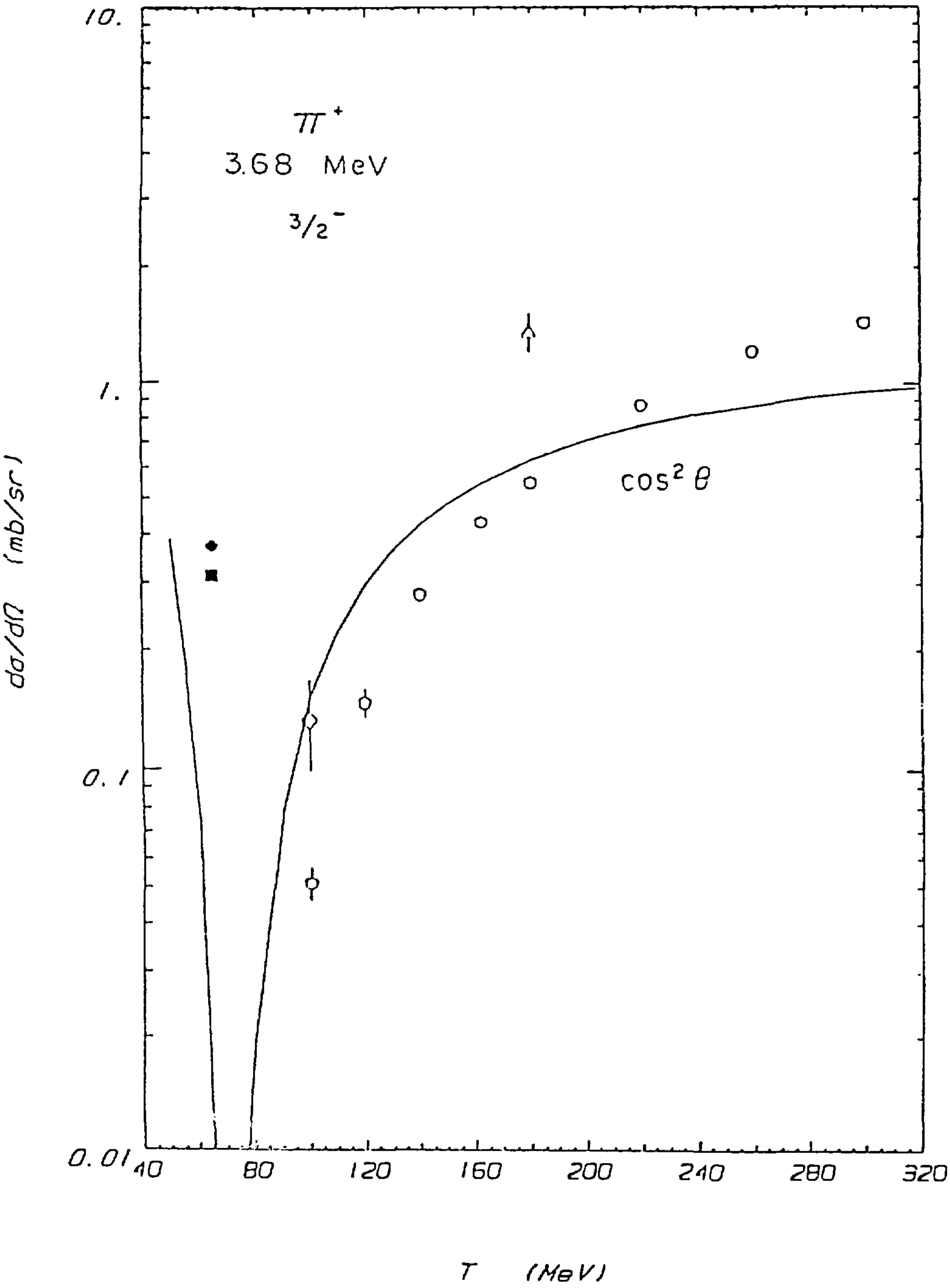

Figure 5.5 Fixed $q \approx 1.1\ \mathrm{fm}^{-1}$ π^+ excitation fuction for the $j = \frac{3}{2}$ state at 3.68 MeV in excitation. The points at 65 MeV are from this work and are described in the text. The open circles are from the work of Seestrom-Morris [See 81]. The diamond at 100 MeV is from the work of Antonuk [Ant 84]. The triangle is from the work of Schwarz [Sch 79]. The curve is $\cos^2\theta$.

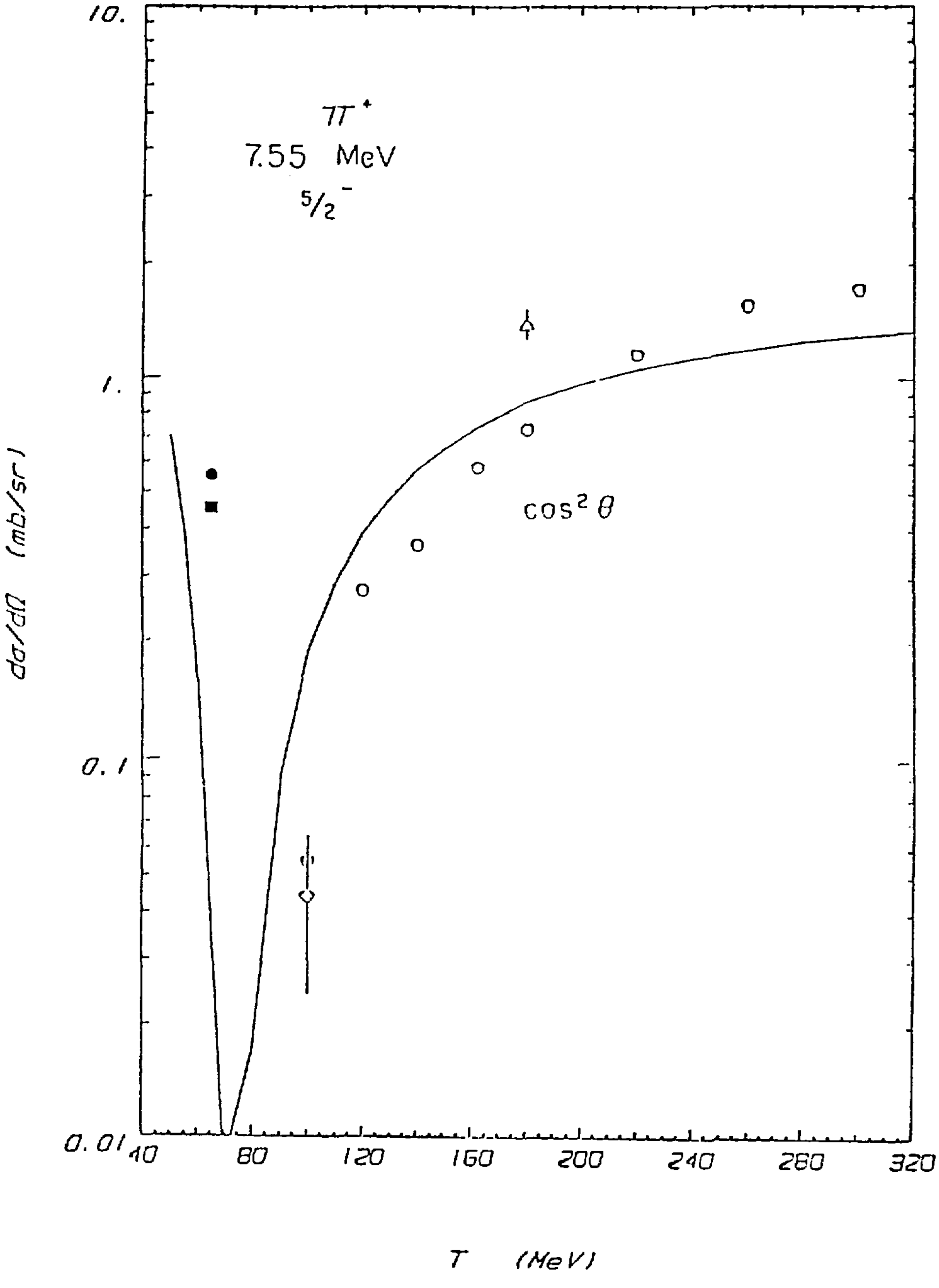

Figure 5.6 Fixed $q \approx 1.1\ \mathrm{fm}^{-1}$ π^+ excitation function for the $j = \frac{5}{2}$ state at 7.55 MeV in excitation. The points at 65 MeV are from this work and are described in the text. The open circles are from the work of Seestrom-Morris [See 81]. The diamond at 100 MeV is from the work of Antonuk [Ant 84]. The triangle is from the work of Schwarz [Sch 79]. The curve is $\cos^2\theta$.

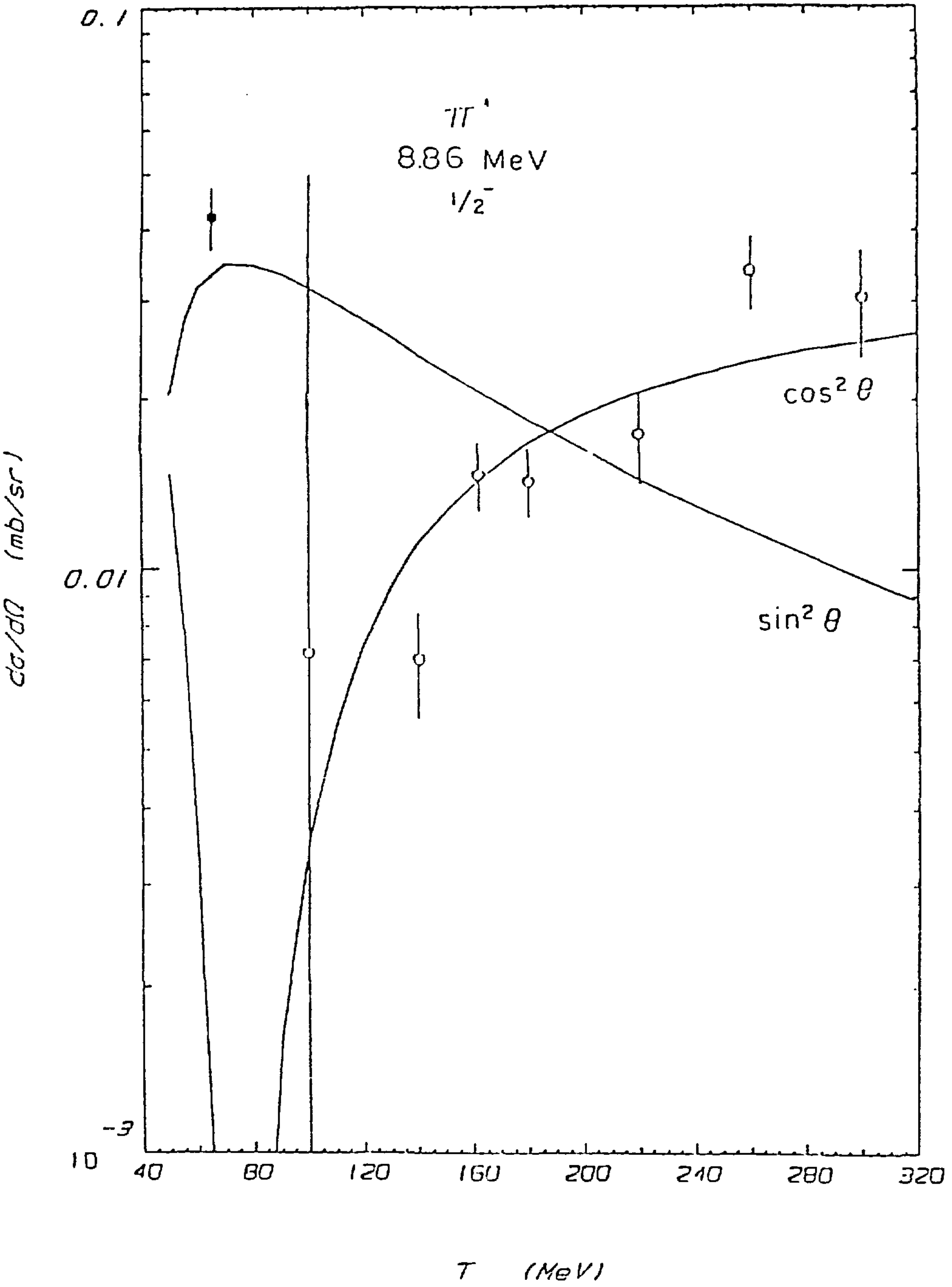

Figure 5.7 Fixed $q \approx 1.1\ \mathrm{fm}^{-1}$ π^+ excitation function for the $j = \frac{1}{2}$ state at 8.86 MeV in excitation. The solid point at 65 MeV is from this work. The open circles are from the work of Seestrom-Morris [See 81]. Both $\sin^2\theta$ and $\cos^2\theta$ are shown.

CHAPTER VI

CONCLUSIONS

This thesis comprises the first study of inelastic transitions in ^{13}C performed with low energy pions. Coarse angular distributions were obtained for the excitations at 3.36 MeV, 7.55 MeV, 8.86 MeV, 9.5 MeV and 11.82 MeV for both positively and negatively charged pions at an incident energy of 65 MeV. In addition, these same excitations were measured at one angle at an incident energy of 50 MeV. These 50 MeV π^- data along with one of the angular points at 65 MeV provided a fixed $q = 0.96$ fm^{-1} excitation function.

Experimental Remarks

This experiment was one of the first performed on the new Clamshell spectrometer at Los Alamos. During this experiment many things were learned about the spectrometer and its associated equiptment. In addition, it became apparent that the system had some problems that needed to be addressed. Unfortunately many of these problems remained unsolved or in some cases were not even realized during the time that these data were taken. These problems have since been corrected.

It was found that the energy resolution of data taken with the Clamshell is very sensitive to the exact channel tune. In particular it is very sensitive to the setting of the last vertical quadrupole (QM03). This effect can be compensated for by using the spectrometer as part of an on-line tuning procedure. The data that comprise this work have a resolution of 510 keV at an incident energy of 65 MeV. Since these data were taken the resolution of the Clamshell has been improved.

The backgrounds at the spectrometer were quite large. This was most likely due to the physically close proximity of the detector array to the scattering chamber and to Coulomb scattering of electrons and muons. The background at the device has since been reduced by adding a muon rejector that consists of an array of plastic scintillators and ranging materials. The added information from these additional detectors makes it easier to reject events associated with electrons and muons. It is also now possible to place a scintillator detector, S1, on the object side of the spectrometer. This has two effects. First, it insures that particles travel through the spectrometer to reach the focal plane. Second, it allows one to make time of flight measurements to aid in the rejection of contaminant particles.

The strong fringe fields of the spectrometer's magnet limited the usefulness of the in-cave beam monitors. This problem can be fixed by providing better shielding for the phototubes on these scintillators. An alternative solution is to take normalization data for every angle that real measurements are made.

None of the problems encountered were fatal and all were the types of things that one might expect at a fledgling facility.

Final Summary of Results

The data obtained in this experiment were compared with other similar data from other probes and with distorted wave calculations. In addition, comparisons were made to previously existing higher energy pion data. Distorted wave calculations were made for all the pion data sets on ^{13}C so that a consistent set of deformation parameters could be extracted. In the case of the 100 MeV data of Antonuk et al. this is the first such analysis that has been performed. It was found that the ratios of $\frac{\beta_+}{\beta_-}$ obtained from these data for the two collective $\Delta L = 2$ transitions are in good agreement with those extracted from the pion data of others at T_π =100, 162, and 180 MeV [Ant 84][See 81][Sch 79]. The values of all the deformation lengths, $\beta R_\pm$, obtained from this work are in good agreement with those measured in high energy proton scattering by Blanpied et al. The angular distribution of the monopole transition at 8.86 MeV was well described by using a simple collective form factor with a surface node. The values of $\beta_\pm$ obtained from distorted wave calculations for this state do not show as much preference for positive pions as those obtained from a similar analysis of resonance pion data from EPICS [See 81]. However, the extracted values of β_{avg} from both pion data sets are in good agreement with the value reported by Peterson et al. [Pet 81] which was obtained from an analysis of alpha scattering data.

The calculations of inelastic transitions all show large effects due to the presence of second order terms in the optical potential that generates the distorted waves. This behavior was expected but it is in sharp contrast with the situation at resonance where the medium effects are clearly visible only around the diffractive minima. Although more data would allow for stronger conclusions, it appears that the phenomenological parameters of Alons et al. [Alo 86] provide an adequate description of these data.

The magnitude of the cross section for π^- scattering to the stretched state at 9.5 MeV is well accounted for the calculations presented. This indicates that an impulse approximation treatment of the spin-flip piece of the πA amplitude is adequate even at 65 MeV. This is somewhat surprising as the impulse approximation is expected to be best at high energies. Although only an upper limit for π^+ scattering to this state was measured, this upper limit is not in conflict with an impulse approximation calculation.

Finally, excitation functions were measured for several transitions at $q = 0.96$ fm^{-1} and the excitation functions of Seestrom-Morris et al. at $q = 1.1$ fm^{-1} [See 81] were extended down to 65 MeV. It was found that the eikonal treatment of Siciliano and Walker still provides a qualitative description of the angular behavior of these excitation functions.

Overall it appears that many of the same techniques used successfully in the description of resonance energy data may be applied at these lower energies provided that medium effects are considered.

REFERENCES

[Ajz 81] F. Ajzenberg-Selove, Nucl. Phys. *A360*, 32 (1981)

[Alo 86] P. Alons et al, to be published (see also) P. Alons, E. Siciliano, M. Leitch, Technical Progress Report- University of Colorado Nuclear Physics Laboratory, Oct 1985

[Ama 86] J. Amann, presentation at Los Alamos spectrometer tutorial, unpublished, (1986).

[Ant 84] L.E. Antonuk et al., Nucl. Phys. *A420*, 435 (1984).

[Arn 85] R.A. Arndt and L.D. Roper, Program SAID.

[Ate 81] L. Atencio et al., Nucl. Instrum. Methods, 187, 381 (1981)

[Bal 83] B. Balestri et al., Nucl. Phys. *A392*, 217 (1983).

[Bar 68] P. Bareyre, C. Bricman, and G. Villet, Phys. Rev. C 165, 1730 (1968).

[Bay 75] G. Baym and G. Brown, Nucl. Phys. *A247*, 395 (1975).

[Bei 75] M. Beiner et al., Nucl. Phys. *A235*, 29 (1975).

[Bil 71] S. Bilen'kaya, Y. Kazarinov, and L. Lapidus, Sov. Phys.-JETP 33, 247 (1971)

[Bla 78] G. Blanpied, W. Coker, and R. Liljestrand, Phys. Rev. C 18, 1436 (1978).

[Ble 83] M. Blecher et al., Phys. Rev. C 28, 2033 (1983).

[Boh 75] A. Bohr and B. Mottelson, Nuclear Structure Volume II, W. A. Benjamin Inc., 1975.

[Boy 81] K. Boyer et al., Phys. Rev. C 24, 598 (1981).

[Bro 80] K. Brown, Transport Manual, Cern Report 80-04 (1980).

[Bur 75] R. Burman, R. Fulton, and M. Jacobson, Nucl. Instrum. Methods 131, 29 (1975).

[Car 81a] J.A. Carr et al., scattering potential code ALLWRLD, unpublished.

[Car 81b] J.A. Carr et al., scattering computer code MSUDWPIES, unpublished.

[Car 82] J.A. Carr, H. McManus, and K. Stricker-Bauer, Phys. Rev. C 25, 952 (1982).

[Cot 80] W. Cottingame and D. Holtkamp, Phys. Rev. Lett. 45, 1828 (1980).

[Don 75] T. Donnelly and J. Walecka, Annu. Rev. Nucl. Sci. 25, 329 (1975).

[Eis 74] R. Eisenstein and G. Miller, Computer Phys. Commun. 8, 130 (1974).

[Eis 76] R. Eisenstein and G. Miller, Computer Phys. Commun. 11, 95 (1976).

[Fic 85] B. Fick, Ph. D. Thesis, Virginia Polytechnic Institute and State University, (1985).

[Fra 83] J. Frank et al., Phys. Rev. D28, 1569 (1983).

[Gre 84] S. Greene et al., Phys. Rev. C 30, 2003 (1984).

[Hei 70] J. Heisenberg, J. McCarthy, and I. Sick, Nucl. Phys. A157, 435 (1970).

[Hic 86] R.S. Hicks et al., Phys. Rev. C 34, 1161 (1986)

[Joh 79] R. Johnson et al., Phys. Rev. Lett. 43, 844 (1979).

[Joh 83a] M. Johnson and E. Siciliano, Phys. Rev. C 27, 730 (1983).

[Joh 83b] M. Johnson and E Siciliano, Phys. Rev. C 27, 1647 (1983).

[Kis 55] L. Kisslinger, Phys. Rev. C 98, 761 (1955).

[Kis 74] L. Kisslinger and F. Tabakin, Phys, Rev. C 9, 188 (1974).

[Kol 71] D. Koltun, Advances in Nuclear Physics, Vol. 3, eds. M. Baranger and E. Vogt, Plenum Press N.Y., 1971.

[Kol 80] D. Koltun, Theory of Meson Interactions with Nuclei, John Wiley & Sons, Inc. N.Y., 1980.

[Koo 86] S. Koonin, Computational Physics, The Benjamin Cummings Publishing Co., Inc., Ca., 1986.

[Lan 73] R. Landau and M. McMillan, Phys. Rev. C 8, 2094 (1973).

[Lee 80a] T. Lee and D. Kurath, Phys. Rev. C 21, 293 (1980).

[Lee 80b] T. Lee and D. Kurath, Phys. Rev. C 22, 1670 (1980).

[LUH 80] LAMPF Users Handbook, Los Alamos National Laboratory report # MP-DO-1-UHB (Rev. 1980), unpublished.

[Mor 78] C. Morris, H. Thiessen, and G. Hoffmann, IEEE Trans. Nucl. Sci., Vol. NS-25, 141 (1978).

[Mor 82] C. Morris, Nucl. Instrum. Methods 196, 263 (1982).

[Pet 80] R. Peterson et al., Phys. Rev. C 21, 1030 (1980).

[Pet 81] R. Peterson, J. Shepard, and R. Emigh, Phys. Rev. C 24, 826 (1981).

[Sat 80] G. Satchler, Introduction to Nuclear Reactions, John Wiley & Sons, Inc., N. Y., (1980).

[Sat 73] G. Satchler, Particles and Nuclei, Vol 5, 105 (1973)

[Sch 79] E. Schwarz et al., Phys. Rev. Lett. 43 1578 (1979).

[See 82] S. Seestrom-Morris et al., Phys. Rev. C 26 594 (1982).

[See 81] S. Seestrom-Morris, Ph.D. Thesis, University of Minnesota, LA-8916-T (1981).

[Sic 81] E. Siciliano and G. Walker, Phys. Rev. C 23, 2661 (1981).

[Sic 85] E. Siciliano et al., DWPIES, unpublished

[Sic 86] E. Siciliano et al., Phys. Rev. C 34, 267 (1986).

[Sky 59] T. Skyrme, Nucl. Phys. 9, 615 (1959).

[Sob 84] R. Sobie et al., Phys. Rev. C 30, 1612 (1984).

[Str 79] K. Stricker, H. McManus, and J. Carr, Phys. Rev. C 19, 929 (1979).

[Str 80] K. Stricker, H. McManus, and J. Carr, Phys. Rev. C 22, 2043 (1980)

[Tay 72] J. Taylor, Scattering Theory, John Wiley & Sons, Inc. N.Y., 1972.

[Tip 78] P. Tipler, Modern Physics, Worth Publishers, Inc., (1978)

[Ull 86a] J. Ullmann et al., to be published.

[Ull 86b] J. Ullmann et al., Phys. Rev. C 33, 2092 (1986).

[Wat 57] K.M. Watson, Phys. Rev. C 105, 1388 (1957).

[Whi 86] S. Whisnant, Phys. Rev. C 33, 1443 (1986).

[Yan 71] C. Yang et al., Nucl. Phys. *A162*, 71 (1971).

[Yuk 35] H. Yukawa, Proceedings of the Mathematical Society of Japan 17, 48 (1935).

APPENDIX A

CHANNEL LOG

Beam Description: 65 MeV π^+, $\theta = 84°$

Magnet	DVM	NMR	Slits & Coll	DVM
BM01	____	5204.23	CL-1	−6.967
BM02	____	5225.29	CL-2	−1.748
BM03	____	5226.65	CL-3	−0.721
BM04	____	5199.51	CL-4	−0.451
QM01	−2.7210	____	CL-9	−0.708
QM02	2.0828	____	CL-10	−0.668
QM03	−1.5695	____	CL-11	−0.184
QM04	−1.4499	____	CL-12	−0.938
			CL-6A	−6.388
			CL-6B	−6.022

Scintillator	Voltage	Chambers	Voltage
S2-P	1872	All Chmbrs	2000
S2-N	1836		
S3-P	1892		
S3-N	2070		
$\pi\mu$	1850		

APPENDIX B

POLYNOMIAL FILE —`POL.DAT`

This is a copy of the file that contains the polynomials used for calculating spectrometer quantities. To read it one must understand another file. In Appendix C there is a file named `BLK001.TXT` which contains the assignment of data word names. For instance in that file it is found that data word 236 is the angle ϕ_{target}. This file (`POL.DAT`) contains the information needed to calculate that quantity. The first number in the first row of a section (each section starts with //) is the data word that is to be calculated. Each row after the first specifies one term in a polynomial expansion of the new data word. The first four entries (columns) in a row give the functional dependence of the term. It is possible to use terms of up to fourth order. The final entry in each row is the coefficient of the term.

```
;[MP1OREP.EXP813]POL.DAT
;UPDATED FOR 65MEV
;
351,2,DRIFT REF CHMBRS 1-4
0,0,0,0,0.,
256,0,0,0,-0.015625,
//
331,2,S2T=S2PT-S2NT
0,0,0,0,0.,
331,0,0,0,10.0,
//
332,2,S3T=S3PT-S3NT
0,0,0,0,0.0,
332,0,0,0,10.0,
//
333,2,S3T-S2T
331,0,0,0,1.0,
```

```
332,0,0,0,-1.0,
//
END OF LOOP 1
241, 18, 65MEV DELTA SCAN
0, 0, 0, 0, -0.434570E+01,
225, 0, 0, 0, 0.807333E+00,
226, 0, 0, 0, -0.391417E-02,
227, 0, 0, 0, 0.159769E-01,
228, 0, 0, 0, -0.110988E-03,
225, 225, 0, 0, -0.345598E-03,
225, 226, 0, 0, 0.369880E-03,
226, 226, 0, 0, -0.404041E-06,
227, 227, 0, 0, 0.914007E-02,
227, 228, 0, 0, -0.457929E-03,
228, 228, 0, 0, -0.826602E-05,
225, 226, 226, 0, -0.172798E-06,
226, 226, 226, 0, -0.679721E-08,
225, 226, 226, 226, -0.221783E-09,
225, 225, 225, 0, 0.147337E-04,
225, 225, 225, 225, 0.359451E-06,
225, 225, 226, 226, 0.374110E-08,
225, 225, 225, 226, -0.785737E-07,
//
234, 12, THETA TARGET 2 SLITS LOG 1 P131
0,0,0,0,-165.
0, 0, 0, 0, 0.164204E+03,
225, 0, 0, 0, -0.751814E+00,
226, 0, 0, 0, -0.178558E+00,
227, 0, 0, 0, 0.282658E-01,
228, 0, 0, 0, 0.472981E-02,
225, 225, 0, 0, -0.338275E-01,
225, 226, 0, 0, 0.429355E-02,
226, 226, 0, 0, -0.329836E-03,
227, 227, 0, 0, 0.109025E+00,
227, 228, 0, 0, -0.421050E-02,
228, 228, 0, 0, -0.240669E-03,
//
235,2, Y TARGET FROM RAYTRACE
227,0,0,0,0.262
228,0,0,0,-0.0551
//
236, 15,PHITARGET
0,0,0,0,-37.0
0, 0, 0, 0, 0.545536E+02,
227, 0, 0, 0, 0.278086E+02,
228, 0, 0, 0, -0.954801E+00,
225, 0, 0, 0, 0.795958E-01,
226, 0, 0, 0, -0.179984E-01,
225, 227, 0, 0, -0.318916E+00,
```

```
225, 228, 0, 0, 0.421706E-01,
226, 227, 0, 0, -0.128407E-01,
227, 228, 0, 0, -0.641303E-01,
227, 227, 227, 0, -0.148724E+00,
227, 227, 228, 0, 0.244862E-01,
225, 225, 227, 0, -0.145817E-01,
227, 227, 225, 0, 0.301873E-01,
228, 228, 225, 0, -0.666825E-03,
//
250,5,THETA REAR ROTATED, LOG 2 P144
0, 0, 0, 0, 60.5E-01,
226, 0, 0, 0, 1.0E-01,
225, 0, 0, 0, -3.26E-01,
225, 225, 0, 0, 7.85E-03,
225, 225, 225, 0, 9.84E-05,
END OF LOOP 2
242,2, DUMMY
0,0,0,0,0.0
246,0,0,0,1.0
//
334,3,S2PRMM
251,0,0,0,1.0,
246,0,0,0,3.3764E-01,
246,246,0,0,-4.037E-02,
//
335,3,S3PRMM
252,0,0,0,1.0,
246,0,0,0,3.3764E-01,
246,246,0,0,-4.037E-02,

END OF LOOP 3
```

APPENDIX C

SELECTED Q FILES

Title File BLK001.TXT

This file shows the meaning of the data words used by the Q system.

```
;[MP1OREP.EXPLEPDEV]BLK001.TXT
;
; CLAMSHELL SPECTROMETER TITLE FILE
; REVISIONS:
; 22-AUG-85 (RLB) RELOCATE S4+/-
; *
;
001, IFLAG0, , DUMMY
002, IDCRW , (1,17,*), COINC REG #1
; * BIT 0
; * BIT 1
; * BIT 2
; * BIT 3
; * BIT 4
; * BIT 5
; * BIT 6
; * BIT 7
; * BIT 8
; * BIT 9
; * BIT 10
; * BIT 11
; * BIT 12
; * BIT 13
003, IS1AA , (1, 3, 0), PULSE HT S1
004, IS2PA , (1, 3, 1), PULSE HT S2 +
005, IS2NA , (1, 3, 2), PULSE HT S2 -
006, IS3PA , (1, 3, 3), PULSE HT S3 +
007, IS3NA , (1, 3, 4), PULSE HT S3 -
008, IS4PA , (1, 3, 5), +
009, IS4NA , (1, 3, 6),
010, ASP1 , (1, 3, 7), PULSE HT S4 +
011, ASP2 , (1, 3, 8), PULSE HT S4 -
012, ASP3 , (1, 3, 9), SPARE ADC
013, ASP4 , (1, 3,10), SPARE ADC
014, ASP5 , (1, 3,11), SPARE ADC
015, IS2PT , (1, 7, 0), TIME S2 +
```

```
016, IS2NT , (1, 7, 1), TIME S2 -
017, IS3PT , (1, 7, 2), TIME S3 +
018, IS3NT , (1, 7, 3), TIME S3 -
019, IS4PT , (1, 7, 4), TIME S4 +
020, IS4NT , (1, 7, 5), TIME S4 -
021, TSP6 , (1, 7, 6), SPARE TDC
022, TSP7 , (1, 7, 7), SPARE TDC
023, IS1TT , (1, 8, 0), TIME S1
024, IRFSYN, (1, 8, 1), RF SYNC
025, TSP2 , (1, 8, 2), SPARE
026, TSP3 , (1, 8, 3), SPARE
027, TSP4 , (1, 8, 4), SPARE
028, TSP5 , (1, 8, 5), SPARE
029, ICSTT , (1, 8, 6), TDC OF SUM TOP CERENKOV
030, ICSTB , (1, 8, 7), TDC OF SUM BOTTOM CERENKOV
031, ICHMB(1,1), (1,9,0), CHMBR 1 X (-)
032, ICHMB(2,1), (1,9,1), CHMBR 1 X (+)
033, ICHMB(3,1), (1,9,2), CHMBR 1 Y (-)
034, ICHMB(4,1), (1,9,3), CHMBR 1 Y (+)
035, ICHMB(1,2), (1,9,4), CHMBR 2 X (-)
036, ICHMB(2,2), (1,9,5), CHMBR 2 X (+)
037, ICHMB(3,2), (1,9,6), CHMBR 2 Y (-)
038, ICHMB(4,2), (1,9,7), CHMBR 2 Y (+)
039, LRX1, (1, 5, 0), CHMBR 1 X LEFT-RIGHT
040, LRY1, (1, 5, 1), CHMBR 1 Y LEFT-RIGHT
041, LRX2, (1, 5, 2), CHMBR 2 X LEFT-RIGHT
042, LRY2, (1, 5, 3), CHMBR 2 Y LEFT-RIGHT
043, ASP6, (1, 5, 4), SPARE ADC
044, ASP7, (1, 5, 5), SPARE ADC
045, ASP8, (1, 5, 6), SPARE ADC
046, ASP9, (1, 5, 7), SPARE ADC
047, ASP10, (1, 5, 8), SPARE ADC
048, ASP11, (1, 5, 9), SPARE ADC
049, ASP12, (1, 5,10), SPARE ADC
050, ASP13, (1, 5,11), SPARE ADC
051, IPHCH1, (1, 2, 0), CEREN PULSHT 1
052, IPHCH2, (1, 2, 1), CEREN PULSHT 2
053, IPHCH3, (1, 2, 2), CEREN PULSHT 3
054, IPHCH4, (1, 2, 3), CEREN PULSHT 4
055, IPHCH5, (1, 2, 4), CEREN PULSHT 5
056, IPHCH6, (1, 2, 5), CEREN PULSHT 6
057, CHSP1, (1, 2, 6), SPARE ADC
058, CHSP2, (1, 2, 7), SPARE ADC
059, CHSP3, (1, 2, 8), SPARE ADC
060, CHSP4, (1, 2, 9), SPARE ADC
061, CHSP5, (1, 2, 10), SPARE ADC
062, CHSP6, (1, 2, 11), SPARE ADC
063, TSPR1, (1, 10, 0), SPARE TDC
064, TSPR2, (1, 10, 1), SPARE TDC
```

```
065, TSPR3, (1, 10, 2), SPARE TDC
066, TSPR4, (1, 10, 3), SPARE TDC
067, TSPR5, (1, 10, 4), SPARE TDC
068, TSPR6, (1, 10, 5), SPARE TDC
069, TSPR7, (1, 10, 6), SPARE TDC
070, TSPR8, (1, 10, 7), SPARE TDC
;
; 71-100 ARE SPARES
;
; *****************************************
;
; FOLLOWING GROUPS OF WORDS ARE
; INTEGERZED BY MULTIPLYING
; REAL WORD BY "FAC" AND ADDING TO "OFF"
; *
; FAC OFF
; 101 ==> 130 100 0
; 131 ==> 150 1 0
; 151 ==> 190 100 0
; 191 ==> 210 1 0
; 211 ==> 250 100 0
; 251 ==> 265 1 0 1ST MULTIS CALL,TST LP #1
; 266 ==> 330 100 0
; 331 ==> 350 1 0 1ST MULTIS CALL,TST LP #1
; 351 ==> 360 100 0
; *
; *******************************************
101, POSX(1), CMBR 1 CRUDE POSIT. X PLANE
102, POSX(2), CMBR 2 CRUDE POSIT. X PLANE
103, POSX(3), CMBR 3 CRUDE POSIT. X PLANE
104, POSX(4), CMBR 4 CRUDE POSIT. X PLANE
105, POSX(5), CMBR 5 CRUDE POSIT. X PLANE
106, POSX(6), CMBR 6 CRUDE POSIT. X PLANE
107, POSX(7), CMBR 7 CRUDE POSIT. X PLANE
108, POSX(8), CMBR 8 CRUDE POSIT. X PLANE
109, POSX(9), CMBR 9 CRUDE POSIT. X PLANE
110, POSX(10), CMBR 10 CRUDE POSIT. X PLANE
111, TPOSX(1), CMBR 1 TRUNC. POS X PLANE
112, TPOSX(2), CMBR 2 TRUNC. POS X PLANE
113, TPOSX(3), CMBR 3 TRUNC. POS X PLANE
114, TPOSX(4), CMBR 4 TRUNC. POS X PLANE
115, TPOSX(5), CMBR 5 TRUNC. POS X PLANE
116, TPOSX(6), CMBR 6 TRUNC. POS X PLANE
117, TPOSX(7), CMBR 7 TRUNC. POS X PLANE
118, TPOSX(8), CMBR 8 TRUNC. POS X PLANE
119, TPOSX(9), CMBR 9 TRUNC. POS X PLANE
120, TPOSX(10), CMBR 10 TRUNC. POS X PLANE
121, DRFTMX(1), CMBR 1 DRIFT TIME X PLANE
122, DRFTMX(2), CMBR 2 DRIFT TIME X PLANE
```

```
123, DRFTMX(3), CMBR 3 DRIFT TIME X PLANE
124, DRFTMX(4), CMBR 4 DRIFT TIME X PLANE
125, DRFTMX(5), CMBR 5 DRIFT TIME X PLANE
126, DRFTMX(6), CMBR 6 DRIFT TIME X PLANE
127, DRFTMX(7), CMBR 7 DRIFT TIME X PLANE
128, DRFTMX(8), CMBR 8 DRIFT TIME X PLANE
129, DRFTMX(9), CMBR 9 DRIFT TIME X PLANE
130, DRFTMX(10), CMBR 10 DRIFT TIME X PLANE
131, CHKSMX(1), CMBR 1 CHECKSUM X PLANE (UNUSED)
132, CHKSMX(2), CMBR 2 CHECKSUM X PLANE (UNUSED)
133, CHKSMX(3), CMBR 3 CHECKSUM X PLANE (UNUSED)
134, CHKSMX(4), CMBR 4 CHECKSUM X PLANE (UNUSED)
135, CHKSMX(5), CMBR 5 CHECKSUM X PLANE (UNUSED)
136, CHKSMX(6), CMBR 6 CHECKSUM X PLANE (UNUSED)
137, CHKSMX(7), CMBR 7 NOT USED
138, CHKSMX(8), CMBR 8 NOT USED
139, CHKSMX(9), CMBR 9 CHECKSUM X PLANE (UNUSED)
140, CHKSMX(10), CMBR 10 CHECKSUM X PLANE (UNUSED)
141, DRFPOX(1), CMBR 1 DRIFT DIST X PLANE
142, DRFPOX(2), CMBR 2 DRIFT DIST X PLANE
143, DRFPOX(3), CMBR 3 DRIFT DIST X PLANE
144, DRFPOX(4), CMBR 4 DRIFT DIST X PLANE
145, DRFPOX(5), CMBR 5 DRIFT DIST X PLANE
146, DRFPOX(6), CMBR 6 DRIFT DIST X PLANE
147, DRFPOX(7), CMBR 7 NOT USED
148, DRFPOX(8), CMBR 8 NOT USED
149, DRFPOX(9), CMBR 9 DRIFT DIST X PLANE
150, DRFPOX(10), CMBR 10 DRIFT DIST X PLANE
151, CPOSX(1), CMBR 1 DRF CORR POS X PLANE
152, CPOSX(2), CMBR 2 DRF CORR POS X PLANE
153, CPOSX(3), CMBR 3 DRF CORR POS X PLANE
154, CPOSX(4), CMBR 4 DRF CORR POS X PLANE
155, CPOSX(5), CMBR 5 DRF CORR POS X PLANE
156, CPOSX(6), CMBR 6 DRF CORR POS X PLANE
157, CPOSX(7), CMBR 7 NOT USED
158, CPOSX(8), CMBR 8 NOT USED
159, CPOSX(9), CMBR 9 DRF CORR POS X PLANE
160, CPOSX(10), CMBR 10 DRF CORR POS X PLANE
161, POSY(1), CMBR 1 CRUDE POSIT. Y PLANE
162, POSY(2), CMBR 2 CRUDE POSIT. Y PLANE
163, POSY(3), CMBR 3 CRUDE POSIT. Y PLANE
164, POSY(4), CMBR 4 CRUDE POSIT. Y PLANE
165, POSY(5), CMBR 5 CRUDE POSIT. Y PLANE
166, POSY(6), CMBR 6 CRUDE POSIT. Y PLANE
167, POSY(7), CMBR 7 CRUDE POSIT. Y PLANE
168, POSY(8), CMBR 8 CRUDE POSIT. Y PLANE
169, POSY(9), CMBR 9 CRUDE POSIT. Y PLANE
170, POSY(10), CMBR 10 CRUDE POSIT. Y PLANE
171, TPOSY(1), CMBR 1 TRUNC. POS Y PLANE
```

```
172, TPOSY(2), CMBR 2 TRUNC. POS Y PLANE
173, TPOSY(3), CMBR 3 TRUNC. POS Y PLANE
174, TPOSY(4), CMBR 4 TRUNC. POS Y PLANE
175, TPOSY(5), CMBR 5 TRUNC. POS Y PLANE
176, TPOSY(6), CMBR 6 TRUNC. POS Y PLANE
177, TPOSY(7), CMBR 7 TRUNC. POS Y PLANE
178, TPOSY(8), CMBR 8 TRUNC. POS Y PLANE
179, TPOSY(9), CMBR 9 TRUNC. POS Y PLANE
180, TPOSY(10), CMBR 10 TRUNC. POS Y PLANE
181, DRFTMY(1), CMBR 1 DRIFT TIME Y PLANE
182, DRFTMY(2), CMBR 2 DRIFT TIME Y PLANE
183, DRFTMY(3), CMBR 3 DRIFT TIME Y PLANE
184, DRFTMY(4), CMBR 4 DRIFT TIME Y PLANE
185, DRFTMY(5), CMBR 5 DRIFT TIME Y PLANE
186, DRFTMY(6), CMBR 6 DRIFT TIME Y PLANE
187, DRFTMY(7), CMBR 7 DRIFT TIME Y PLANE
188, DRFTMY(8), CMBR 8 DRIFT TIME Y PLANE
189, DRFTMY(9), CMBR 9 DRIFT TIME Y PLANE
190, DRFTMY(10), CMBR 10 DRIFT TIME Y PLANE
191, CHKSMY(1), CMBR 1 CHECKSUM Y PLANE (UNUSED)
192, CHKSMY(2), CMBR 2 CHECKSUM Y PLANE (UNUSED)
193, CHKSMY(3), CMBR 3 CHECKSUM Y PLANE (UNUSED)
194, CHKSMY(4), CMBR 4 CHECKSUM Y PLANE (UNUSED)
195, CHKSMY(5), CMBR 5 CHECKSUM Y PLANE (UNUSED)
196, CHKSMY(6), CMBR 6 CHECKSUM Y PLANE (UNUSED)
197, CHKSMY(7), CMBR 7 NOT USED
198, CHKSMY(8), CMBR 8 NOT USED
199, CHKSMY(9), CMBR 9 CHECKSUM Y PLANE (UNUSED)
200, CHKSMY(10), CMBR 10 CHECKSUM Y PLANE (UNUSED)
201, DRFPOY(1), CMBR 1 DRIFT DIST Y PLANE
202, DRFPOY(2), CMBR 2 DRIFT DIST Y PLANE
203, DRFPOY(3), CMBR 3 DRIFT DIST Y PLANE
204, DRFPOY(4), CMBR 4 DRIFT DIST Y PLANE
205, DRFPOY(5), CMBR 5 DRIFT DIST Y PLANE
206, DRFPOY(6), CMBR 6 DRIFT DIST Y PLANE
207, DRFPOY(7), CMBR 7 NOT USED
208, DRFPOY(8), CMBR 8 NOT USED
209, DRFPOY(9), CMBR 9 DRIFT DIST Y PLANE
210, DRFPOY(10), CMBR 10 DRIFT DIST Y PLANE
211, CPOSY(1), CMBR 1 DRF CORR POS Y PLANE
212, CPOSY(2), CMBR 2 DRF CORR POS Y PLANE
213, CPOSY(3), CMBR 3 DRF CORR POS Y PLANE
214, CPOSY(4), CMBR 4 DRF CORR POS Y PLANE
215, CPOSY(5), CMBR 5 DRF CORR POS Y PLANE
216, CPOSY(6), CMBR 6 DRF CORR POS Y PLANE
217, CPOSY(7), CMBR 7 NOT USED
218, CPOSY(8), CMBR 8 NOT USED
219, CPOSY(9), CMBR 9 DRF CORR POS Y PLANE
220, CPOSY(10), CMBR 10 DRF CORR POS Y PLANE
```

```
221, XFRON, X FRONT
222, THTFR, THETA FRONT
223, YFRON, Y FRONT
224, PHIFR, PHI FRONT
225, XREAR, X AT REAR CHAMBERS
226, THTRE, THETA AT REAR CHAMBERS
227, YREAR, Y AT REAR CHAMBERS
228, PHIRE, PHI AT REAR CHAMBERS
229, SPARE
230, SPARE
231, SPARE
232, SPARE
233, XTGT, X TARGET
234, THTTGT, THETA TARGET
235, YTGT, Y TARGET(UNROT)
236, PHITGT, PHI TARGET
237, THTCHK, THETA CHECK
238, PHICHK, PHI CHECK
239, THTA1, THETA AT A1 TGT
240, DELTPA, DELTA OF PART A TO BEAM
241, DELTPC, DELTA OF PART C TO SPECT
242, QOPT, QEXACT OPTIMIZED
243, CRUDEL, CRUDE DELTA
244, XROTG, X AT REAL ROTATED TGT
245, YROTG, Y AT REAL ROTATED TGT
246, QEXACT, MISSING MASS FROM CALKIN
247, THTSCT, SCATTERING ANGLE FROM CALKIN
248, PTRANS, MOMENTUM XFER FROM CALKIN
249, XDEP, DEP VAR FROM XXDEP
250, THTCUT THETA REAR ROTATED
; ********************************
; *
; THESE QUANTITIES HAVE A MULT OF 1.0, BUT OFFSET OF 0
; *
251, S2DELE, S2 DELTA E
252, S3DELE, S3 DELTA E
253, DES23, GEOMETRIC MEAN S2 AND S3
254, TMS2, SUMMED TIM S2
255, TMS3, SUMMED TIM S3
256, TSM23, AVG TIME S2&S3 (REFERENCE TIME)
257, S1TOF, (2*IS1TT-TMS23+I152)
258, CHPH, CHERENKOV PH SUM
259, S1DELE, S1 DELTA E
260, S23TOF, S23 TIM OF FLIGHT
261, TS1OFF, OFFSET S1 (.1NS/CH)
262, TIME CH POS
262, TIME CH TIME E
264, RFTIM ,RF TIME
265, CRFTIM, CORRECTED RF TIME
```

```
; *
; ****************************
266, S1CTOF, S1 CORRECTED TOF (0.01NS/CHAN)
267, TOF, TOF WRT 5NS RF
268, MOUT, OUTGOING MASS (100KEV/CHAN)
269, OPT TRF
270, POUT, MOMENTUM OF
; OUTGOING PARTICLE (100KEV/C/CHAN)
271, DLOSS, (DELTAA-DELTAC) CALC BY MULTIM
272, DSQXF, DIF12X**2 + DIF34X**2
273, DSQYF, DIF12Y**2 + DIF34Y**2
274, DSQXR, DIF56X**2 + DIF910X**2
275, DSQYR, DIF56Y**2 + DIF910Y**2
276, DSQ12Y, DIF12Y**2
277, DSQ34Y, DIF34Y**2
278, DSQ12X, DIF12X**2
279, DSQ34X, DIF34X**2
280, SPARE
; ********************************
; *
; THE FOLLOWING QUANTITIES ARE RELATED
; TO PAIRS OF DRIFT CHAMBERS
; THEY WILL ALL DISAPPEAR WITH THE
; ADVENT OF LEFT/RIGHT LOGIC
; CHAMBERS.
; ******************************
281, X12 * MEAN POSIT X1&2
282, X34 * MEAN POSIT X3&4
283, X56 * MEAN POSIT X5&6
284, X78 * MEAN POSIT X7&8
285, X90 * MEAN POSIT X9&10
286, Y12 * MEAN POSIT Y1&2
287, Y34 * MEAN POSIT Y3&4
288, Y56 * MEAN POSIT Y5&6
289, Y78 * MEAN POSIT Y7&8
290, Y90 * MEAN POSIT Y9&10
291, DIF12X(1), POS DIF1 CHMBRS 1&2 X PLANE
292, DIF12X(2), POS DIF2 CHMBRS 1&2 X PLANE
293, DIF12X(3), POS DIF3 CHMBRS 1&2 X PLANE
294, DIF12X(4), POS DIF4 CHMBRS 1&2 X PLANE
295, DIF34X(1), POS DIF1 CHMBRS 3&4 X PLANE
296, DIF34X(2), POS DIF2 CHMBRS 3&4 X PLANE
297, DIF34X(3), POS DIF3 CHMBRS 3&4 X PLANE
298, DIF34X(4), POS DIF4 CHMBRS 3&4 X PLANE
299, DIF56X(1), POS DIF1 CHMBRS 5&6 X PLANE
300, DIF56X(2), POS DIF2 CHMBRS 5&6 X PLANE
301, DIF56X(3), POS DIF3 CHMBRS 5&6 X PLANE
302, DIF56X(4), POS DIF4 CHMBRS 5&6 X PLANE
303, DIF78X(1), POS DIF1 CHMBRS 7&8 X PLANE
```

```
304, DIF78X(2), POS DIF2 CHMBRS 7&8 X PLANE
305, DIF78X(3), POS DIF3 CHMBRS 7&8 X PLANE
306, DIF78X(4), POS DIF4 CHMBRS 7&8 X PLANE
307, DIF90X(1), POS DIF1 CHMBRS 9&10 X PLANE
308, DIF90X(2), POS DIF2 CHMBRS 9&10 X PLANE
309, DIF90X(3), POS DIF3 CHMBRS 9&10 X PLANE
310, DIF90X(4), POS DIF4 CHMBRS 9&10 X PLANE
311, DIF12Y(1), POS DIF1 CHMBRS 1&2 Y PLANE
312, DIF12Y(2), POS DIF2 CHMBRS 1&2 Y PLANE
313, DIF12Y(3), POS DIF3 CHMBRS 1&2 Y PLANE
314, DIF12Y(4), POS DIF4 CHMBRS 1&2 Y PLANE
315, DIF34Y(1), POS DIF1 CHMBRS 3&4 Y PLANE
316, DIF34Y(2), POS DIF2 CHMBRS 3&4 Y PLANE
317, DIF34Y(3), POS DIF3 CHMBRS 3&4 Y PLANE
318, DIF34Y(4), POS DIF4 CHMBRS 3&4 Y PLANE
319, DIF56Y(1), POS DIF1 CHMBRS 5&6 Y PLANE
320, DIF56Y(2), POS DIF2 CHMBRS 5&6 Y PLANE
321, DIF56Y(3), POS DIF3 CHMBRS 5&6 Y PLANE
322, DIF56Y(4), POS DIF4 CHMBRS 5&6 Y PLANE
323, DIF78Y(1), POS DIF1 CHMBRS 7&8 Y PLANE
324, DIF78Y(2), POS DIF2 CHMBRS 7&8 Y PLANE
325, DIF78Y(3), POS DIF3 CHMBRS 7&8 Y PLANE
326, DIF78Y(4), POS DIF4 CHMBRS 7&8 Y PLANE
327, DIF90Y(1), POS DIF1 CHMBRS 9&10 Y PLANE
328, DIF90Y(2), POS DIF2 CHMBRS 9&10 Y PLANE
329, DIF90Y(3), POS DIF3 CHMBRS 9&10 Y PLANE
330, DIF90Y(4), POS DIF4 CHMBRS 9&10 Y PLANE
;**************************************************
;WORDS 331-350 HAVE MULT OF 1.0 AND OFFSET OF 0.
;
331, DELTS2, TIME DIF S2P-S2N
332, DELTS3, TIME DIF S3P-S3N
333, DELT23, TIME DIFF S3P-S3N-S2P+S2N
334, S2PRMM, S2 CORRECTED FOR MMASS CORELATION EXP813
335, S3PRMM, S3 CORRECTED FOR MMASS CORELATION EXP813
336, SPARE
337, SPARE
338, SPARE
339, SPARE
340, SPARE
;341-350, SPARE
;*************************************************
;
351, DRFRF(1), DRIFT REF TIME CHAMBER 1
352, DRFRF(2), DRIFT REF TIME CHAMBER 2
353, DRFRF(3), DRIFT REF TIME CHAMBER 3
354, DRFRF(4), DRIFT REF TIME CHAMBER 4
355, DRFRF(5), DRIFT REF TIME CHAMBER 5
356, DRFRF(6), DRIFT REF TIME CHAMBER 6
```

```
357, DRFRF(7), DRIFT REF TIME CHAMBER 7
358, DRFRF(8), DRIFT REF TIME CHAMBER 8
359, DRFRF(9), DRIFT REF TIME CHAMBER 9
360, DRFRF(10), DRIFT REF TIME CHAMBER 10
;
; 361-400 ARE SPARES AT EPICS and LEP

;
```

Histogram Setup File EXP813.HST

This file defines the histograms that are to be made. To define a histogram the user must specify the data word, IN, the limits of that word, X, the desired bin width, BI, and the test that must be met before the data is included in the histogram, TE.

```
;[MP1OREP.EXP813]EXP813.HST
;SHORTENED FILE
/VE:BR
/DE:ALL
/DF/BL:1
;XREAR/IN:225/X:-5000:5000/BI:20/TE:111
;THTRE/IN:226/X:-5000:5000/BI:50/TE:112
;YREAR/IN:227/X:-2000:2000/BI:20/TE:113
;PHIRE/IN:228/X:-2000:2000/BI:50/TE:114
;THTROT/IN:250/X:-3000:3000/BI:50/TE:112
;
;TEST ==> GOOD CHMBRS,PID,FOCAL PLANE
/DF/TE:106
;THTTGT/IN:234/X:-3000:3000/BI:25
;YTGT/IN:235/X:-1500:1500/BI:20
;PHITGT/IN:236/X:-2000:2000/BI:25
;
;TEST ==> GOOD CHMBRS,S2PRMM,S3PRMM,TGT,FOCAL PLANE
MMASSC/IN:246/X:-1000:3000/BI:4/TE:106
; PID SCINTILATOR BOX ON S2 AND S3
;S2S3/XP:251:0:400:5/YP:252:0:400:5/TE:0
;
;IN THE NEXT SECTION WE HAVE A BUNCH OF CHAMBERS HISTOS
POSX1/IN:101/X:-5000:5000/BI:2/TE:27
POSX2/IN:102/X:-5000:5000/BI:2/TE:27
DRFPX1/IN:141/X:-5:50/BI:1/TE:27
DRFPX2/IN:142/X:-5:50/BI:1/TE:27
CPOSX1/IN:151/X:-5000:5000/BI:2/TE:27

CPOSX2/IN:152/X:-5000:5000/BI:2/TE:27
```

Schematic Test File EXP813.TST

This is where the tests are defined. This is not a complete test file. This sample file contains principally those tests that were used on the final missing mass histograms.

```
;[MP1OREP.EXPLEPC43]DEV.TST 26-AUG-85 CYCLE 43 DEV
;
/TE:150/BL:3/IG:10/IB:10
;
BLOCK,1
;
; CHAMBER ANODE TESTS
;
1,GAT,31,50,3500, ;1 X1P
2,GAT,32,50,3500, ;2 X1N
3,GAT,33,50,2650, ;3 Y1P
4,GAT,34,50,2650, ;4 Y1N
5,GAT,35,50,3500, ;5 X2P
6,GAT,36,50,3500, ;6 X2N
7,GAT,37,50,2250, ;7 Y2P
8,GAT,38,50,2250, ;8 Y2N
;
;
;PARTICLE IDENTIFICATION
;
11,IBOX,1, ;11 ;BOX 1 ==>OLD PID
;
; LEFT-RIGHT TESTS
;
12,GATE,39,0,529, ;12 ;LRX1 GATE
13,GATE,40,0,629, ;13 ;LRY1 GATE
14,GATE,41,0,656, ;14 ;LRX2 GATE
15,GATE,42,0,738, ;15 ;LRY2 GATE
;
21,AND,1,2, ;21 X1 GOOD ANODES
22,AND,3,4, ;22 Y1 GOOD ANODES
23,AND,5,6, ;23 X2 GOOD ANODES
24,AND,7,8, ;24 Y2 GOOD ANODES
25,AND,21,22, ;25 GOOD XY1
26,AND,23,24, ;26 GOOD XY2
27,AND,25,26, ;27 GOOD ANODES
;
36,AND,27,11, ;36 GOOD ANODES,OLD PID
;
50,IOR,1,-1, ;50 ;LOOP1 COUNTER
BLOCK,2,
;
; CHAMBER DRIFT TIME TESTS
```

```
;
51,GAT,121,-2,42, ;51 DRTX1
52,GAT,181,-2,42, ;52 DRTY1
53,GAT,122,-2,42, ;53 DRTX2
54,GAT,182,-2,42, ;54 DRTY2
;
55,AND,27,51, ;55
56,AND,27,52, ;56
57,AND,27,53, ;57
58,AND,27,54, ;58
;
60,AND,55,56,57,58, ;60 GOOD CHAMBERS, DRIFT TIME
61,AND,60,11, ;61 GOOD CHAMBERS, OLD PID
62,AND,60,-11, ;62 GOOD CHAMBERS, NOT OLD PID
;
;TARGET TESTS
;
65,GAT,250,-2600,2600, ;65 ;ROTATED THETA REAR
66,GAT,234,-999,1001, ;66 ;THTTGT
67,GAT,235,-299,300, ;67 ;YTGT
68,GAT,236,-1240,1001, ;68 ;PHITGT
69,GAT,225,-4999,5001, ;69 ;XREAR
70,GAT,226,-3499,2200, ;70 ;THTRE
71,GAT,227,-999,1000, ;71 ;YREAR
72,GAT,228,-699,500, ;72 ;PHIRE
;
;GATES AND BOXES (DO WITH THESE AS YOU WISH)
;
75,IBOX,2, ;75 ;BOX 2
76,IBOX,3, ;76 ;BOX 3
77,IBOX,4, ;77 ;BOX 4
78,IBOX,5, ;78 ;BOX 5
79,IBOX,6, ;79 ;BOX 6
80,IGAT,6, ;80 ;GATE 6 ELASTIC
81,IGAT 1, ;81 ;IGATE 1
82,IGAT,2, ;82 ;IGATE 2
83,IGAT,3, ;83 ;IGATE 3
84,IGAT,4, ;84 ;IGATE 4
85,IGAT,5, ;85 ;IGATE 5
;
; EXPERIMENT SPECIFIC GOOD EVENT TESTS
;
;
;
; I DEFINED THESE NEXT FOUR TEST JOE MITCHELL 10/10/85
; THESE TEST USE THE S2PRMM AND S3PRMM PIDS ONLY
103,AND,60,66,67,68, ;103 ;GOOD CHAMBRS, GOOD TGT TESTS
104,AND,65,69,70,71,72, ;104 ;GOOD FOCAL PLANE
105,AND,75,103,104, ;105 ;G CHAMBRS,TARG,FP,S2 PID
```

```
106,AND,105,76, ;106 ; " " " ",S3 PID
107,AND,-75,103,104 ;107 ; " " NOT S2 PID
108,AND,-76,107 ;108 ; " "" NOT S2 PID,NOT S3 PID
;
111,AND,61,65,70,71,72, ;111 ;FP EVENT, EXCEPT XREAR
112,AND,61,69,71,72, ;112 ; THTRE
113,AND,61,65,69,70,72, ;113 ; YREAR
114,AND,61,65,69,70,71, ;114 ; PHIRE
;
;
150,IOR,1,-1, ;150 ;LOOP 2 COUNTER (WHOOPEE ALL DONE)

;
```

APPENDIX D

PION DECAY

The pion is known to exist in three different charge states , $q_\pi = 0, \pm 1$. None of the three charge states is stable. The two states with non-zero electric charge (the π^+ and π^-) have the same mean lifetime, $\overline{\tau} = 2.60 \times 10^{-8}$ sec or $c\overline{\tau} = 780.4$ cm. These lifetimes are measured in the pion rest frame.

Because these charged pions have a lifetime that is short on laboratory time scales some of the scattered pions decay after scattering but before they reach the detector array. A correction must be made for these events. For any statistical decay process the number of particles that decay in a small time interval dt is proportional to the total number of particles N. This relationship can be written

$$-dN = \lambda N dt,$$

where the minus sign indicates that N is decreasing in time. This equation is easily integrated and gives the familiar law of radioactive decay

$$N = N_\circ \exp(-\lambda t).$$

It is easily shown that the decay constatnt, λ is the recipocal of the mean lifetime, $\overline{\tau}$ [Tip 78]. Therefore in the pion rest frame the decay relation can be written

$$\frac{N}{N_\circ} = \exp(-t/\overline{\tau}).$$

For pions moving with a velocity v, the observed lifetime in the lab will be increased by a factor of $\gamma = \frac{1}{\sqrt{1-\beta^2}}$, where $\beta = v/c$. For pions traveling a fixed distance in the lab (such as through a spectrometer) the decay relation can be written in terms of this distance, d. One such expression is

$$SF = \frac{N}{N_\circ} \exp(-\frac{d}{\gamma\beta c\tau}).$$

This is essentially the decay correction in the cross section formula of Chapter 2. There is one additional complication due to the fact that particles with slightly different momenta travel paths of sligthly different lengths. This effect is easily accounted for. The path length through the spectrometer can be expressed in terms of the particle's momentum difference from the central ray, $\delta = \frac{(p-p_{sp})}{p_{sp}} \times 100$ (p_{sp} is the central momentum of the spectrometer and is determined by the magnetic field). In terms of δ the pathlength to the optical focal plane is (the optical focal plane is the actual image plane)

$$d = 1.82 + 0.016\delta \text{ m}.$$

There is a small additional correction to this pathlength because the optical focal plane is 19 degrees steeper than the physical focal plane (the plane in which the first set of wire chambers lie). The final result is

$$d = 1.82 + 0.0117\delta \text{ m}.$$

A charged pion decays into a muon and a muon neutrino. Because this is a simple two body decay certain restrictions on the trajectories of the outgoing particles arise due to two body kinematics. In particular, if a moving pion is observed to decay in the laboratory there is a maximum angle, relative to the pions laboratory velocity vector, which the muon can attain. This angle will be denoted θ_{max}. Another angle that is often used is the opening angle. The opening angle is twice θ_{max}. It gets its name because it is the opening angle of the cone which is accesable to the muon. This cone is called the Jacobian cone. An expression for the maximum angle between the muon's velocity vector and the pions velocity vector is

$$\tan\theta_{max} = \sqrt{\frac{1-\beta_\pi^2}{(\frac{\beta_\pi^2}{\beta_\mu^2})^2 - 1}}.$$

Here β_π is the lab β of the pion while β_μ is the β of the muon in the pions rest frame. For pions of 50 MeV this expression gives a maximum angle of 17.97 degrees. For 70 MeV pions θ_{max} is 14.66 degrees. It turns out that the decay muons tend to group towards the edge of the Jacobian cone.

ACKNOWLEDGEMENTS

There are so many people who have helped me in my graduate studies that it is impossible to thank them all individually. Some that I would like to thank specifically are the people at the Nuclear Physics Lab, especially Jerry Peterson, Jack Kraushaar, Ernie Rost, and Joe McDermott. The people at MP-10 in Los Alamos were very helpful. In particular I would like to thank Dick Boudrie (for assistance with the Clamshell facility), Chris Morris (for the target), and Susan Seestrom-Morris (for helping me with the computer).